Wetting and dewetting effects of bubbles, droplets and solids

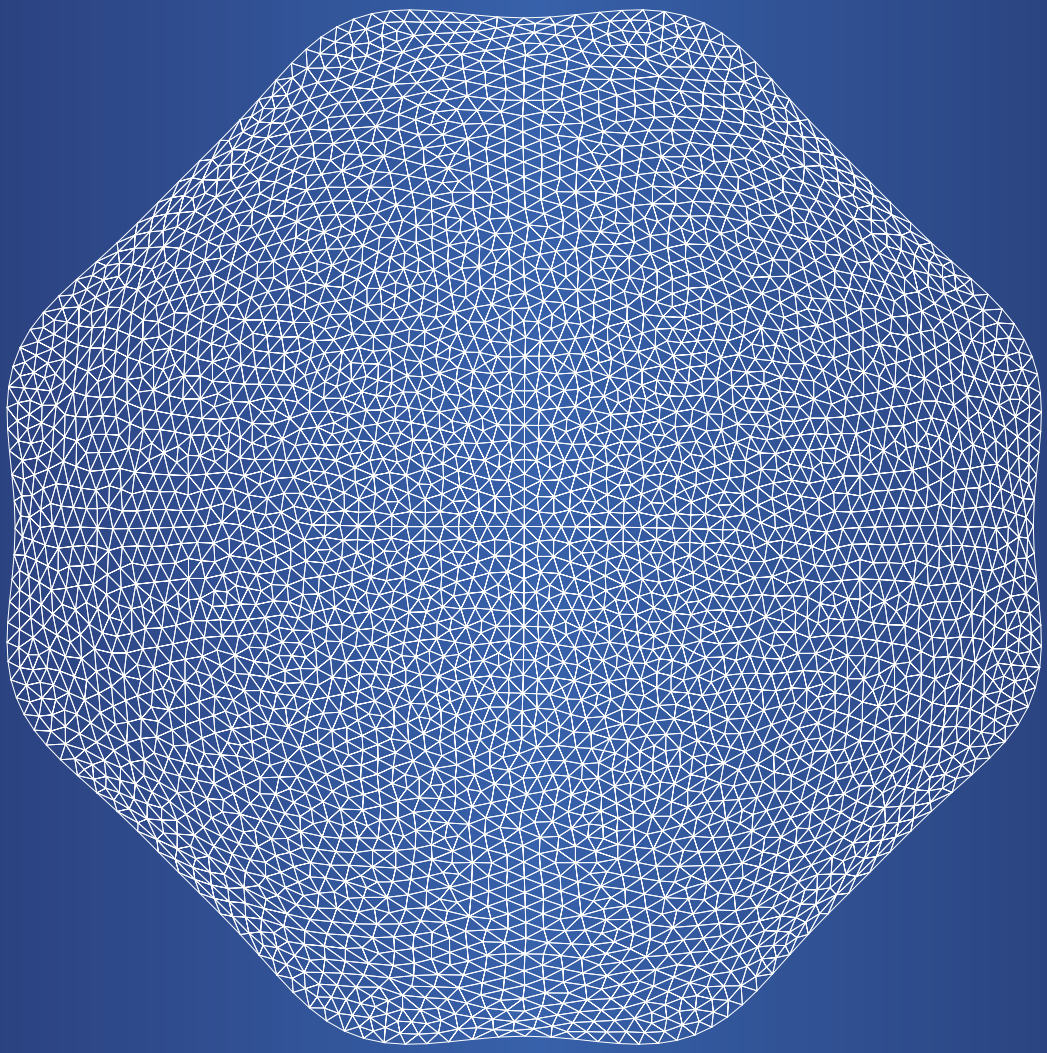

Ivan Dević

WETTING AND DEWETTING EFFECTS OF BUBBLES, DROPLETS AND SOLIDS

Ivan Dević

Graduation Committee:

Prof. dr. J. W. M. Hilgenkamp (chairman)	University of Twente
Prof. dr. D. Lohse (supervisor)	University of Twente
Prof. dr. J. H. Snoeijer	University of Twente
Prof. dr. D. van der Meer	University of Twente
Dr. E. S. Kooij	University of Twente
Prof. dr. U. Thiele	Westfälische Wilhelms-Universität Münster
Prof. dr. A. A. Darhuber	Eindhoven University of Technology

The work in this thesis was carried out at the Physics of Fluids Group, Max-Planck-Center Twente for complex fluid dynamics, Mesa+ Institute, and J. M. Burgers Centre for Fluid Dynamics, Faculty of Science and Technology, University of Twente. This thesis was financially supported by The Netherlands Center for Multiscale Catalytic Energy Conversion (MCEC), an NWO Gravitation Programme funded by the Ministry of Education, Culture and Science of the government of The Netherlands..

Cover design: Ivan Dević

Publisher: Ivan Dević,
Physics of Fluids Group, University of Twente,
P.O. Box 217, 7500 AE Enschede, The Netherlands
pof.tnw.utwente.nl

Print: Gilderprint, Enschede

ISBN: 978-90-365-4643-0
DOI: 10.3990/1.9789036546430

WETTING AND DEWETTING EFFECTS OF BUBBLES, DROPLETS AND SOLIDS

DISSERTATION

to obtain
the degree of doctor at the University of Twente,
on the authority of the rector magnificus,
Prof. dr. T. T. M. Palstra,
on account of the decision of the graduation committee
to be publicly defended
on Friday the 26th of October 2018 at 16:45

by

Ivan Dević

Born on 14$^{\text{th}}$ of January, 1990
in Split, Croatia

This dissertation has been approved by the supervisor:

Prof. dr. Detlef Lohse

Contents

1 Introduction

Fluids are everywhere around and inside us, like a blood flow inside our veins which keeps us alive, to rivers, lakes and seas. If we would trust words of the one and the only Albert Einstein: *"Only two things are infinite: the universe and human stupidity"*, it would imply that every fluid is finite. Or in other words: *every single fluid body has an interface.* Although this might not come as a big surprise to many readers, I invite you to think again. We all know how the falling drop looks like, we have all seen break up of a jet of fluid in a series of droplets and we were all once lost romantics who observed rain on the windshield of a car or a bus. All of this phenomena has one thing in common: they are driven by interfaces and their respective properties. If the droplet of a particular liquid is positioned on the substrate, there are at least three interfaces present in the system, namely, the droplet-substrate interface, the droplet-environment and the environment-substrate, where environment describes either a liquid or a gas phase which covers the substrate and surrounds the droplet (Figure 1.1.b). The problem of many interface interaction is at the core of the fluid physics field called *wetting.*

Wetting has many industrial applications such as microfluidics [7] or catalysis [2], in which the precise control of a single droplet or a single bubble morphology is crucial, along with a collective interaction between many droplets or bubbles via diffusion process. The main problem of industrial applications of wetting is that at the scientific level, there are still many open fundamental question.[3, 5, 9, 11, 12] Throughout this thesis, we have challenged many of this questions and extended the application of wetting principles to finite

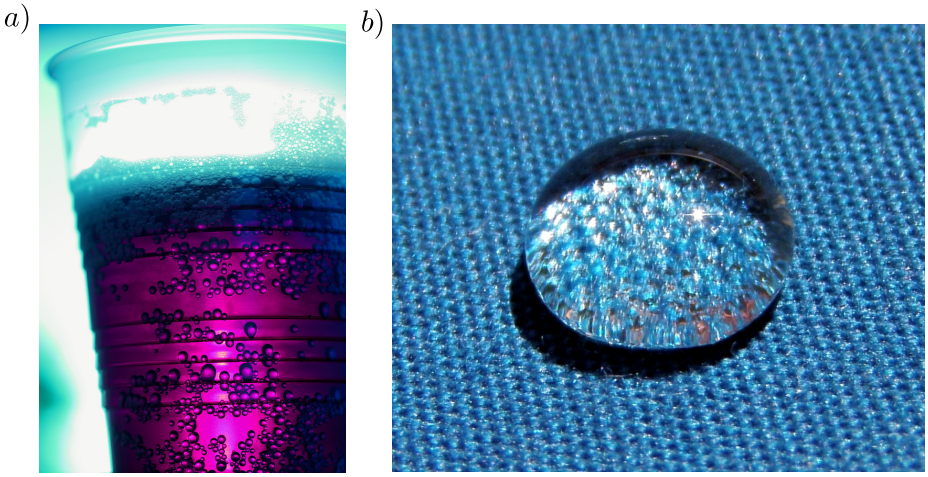

Figure 1.1: *a)* Nucleation of bubbles on a glass surface in a soda drink. (Image taken by Brocken Inaglory, CC BY-SA 3.0) *b)* Single drop wetting a DWR-coated surface (Image taken by Pink Sherbet Photography, CC BY 2.0)

solid bodies. If one would have to summarise all of questions tackled in this thesis in to the one question, it would be: *"What are properties of wetting equilibriums?"*.

1.1 Fundamental theory

Existence of interfaces is driven by molecular cohesive forces between molecules of same species. In the fluid bulk, the net cohesive force is close to zero, since every molecule experiences this force from every direction. However, on the fluid boundary, there is only certain part of space in which a single molecule feels the cohesive force, so the net cohesive force has a direction towards the bulk of fluid. On the macroscopic level, we average this interactions along the interface and introduce the physical quantity called the *surface tension*, which is usually denoted with γ. The SI unit for the surface tension is J/m^2 or N/m, so usual interpretations of the surface tension are that either it describes the energy area density or the force length density. If we would multiply the surface tension of some interface with the area of the same interface, we would obtain the value of an *interfacial energy* for that interface. The sum minimum of all interfacial energy in the system describes the equilibrium state of the wetting system. If there are no additional interactions present in the system, two major properties of the interface in the equilibrium state are obtained: the Young-Laplace equation and the Young's law. Both of these laws will be discussed in the further text.

Let us imagine a droplet of volume V and the droplet surface tension with the environment $\gamma_{v\ell}$ (such as one in Figure 1.1.b), where the index ℓ denotes

the liquid phase (droplet) and v denotes the environment, which in this case is considered to be *vapour phase*. If we would position this droplet on the homogeneous flat solid substrate (denoted with the index s), two additional surface tensions would emerge: γ_{sv} and $\gamma_{s\ell}$. The total interfacial energy of this system reads

$$E = \gamma_{v\ell} A_{v\ell} + \gamma_{sv} A_{sv} + \gamma_{s\ell} A_{s\ell} - \gamma_{sv} A_{s\ell} \tag{1.1}$$

where indices for both the area and the surface tension denotes which interface we are observing in the system. First two terms on the right hand side express the interfacial energy of the system in which the droplet does not exist, while the term $\gamma_{s\ell} A_{s\ell}$ tells us how much energy we need to invest to create the droplet interface with the vapour phase, while the term $\gamma_{v\ell} A_{s\ell}$ accounts for the destruction of the part of the solid-vapour interface. If we assume that the substrate is infinite compared to the droplet, we can omit the second term from Eq. 1.1, since the value of A_{sv} will be constant for any droplet volume V. The trivial minimum of Eq. 1.1 is that the value of all interfaces is zero, therefore, the total interfacial energy is also zero. To evade this problem, we will introduce the droplet volume constraint on the Eq. 1.1, thus we obtain

$$E = \gamma_{v\ell} A_{v\ell} + (\gamma_{s\ell} - \gamma_{sv}) A_{s\ell} + \lambda V \tag{1.2}$$

where λ is a Lagrange multiplier for the volume constraint. To obtain the analytical solution for the minimum of the Eq. 1.2, we will assume that the droplet is axisymmetric and we can describe the interface as a function $h(x)$, where h denotes the local height of the interface, while x is the radial coordinate. Using differential geometry we can rewrite Eq. 1.2 as

$$E = \int_0^{x_f} \left(\sqrt{1 + \left(\frac{dh}{dx}\right)^2} \gamma_{v\ell} + (\gamma_{s\ell} - \gamma_{sv}) + \lambda h \right) 2\pi x dx \tag{1.3}$$

where $2\pi x dx$ is an area differential term for the axisymmetric polar coordinate system, while x_f denotes the position of the three-phase contact line. The term in brackets inside the integral will from now on be denoted with Γ. To minimise the value of Eq. 1.3 under the volume constraint, we will use the Euler-Lagrange equation. Although Euler-Lagrange equation is more often used to determine dynamics of the system, we can minimise Eq. 1.3 by replacing time with the radial coordinate x, general coordinates with the height h and the general velocities with the $h' \equiv \frac{dh}{dx}$. Once all these replacement have been done, we can state that the minimum value of Eq. 1.3 resides in the solution of the second order partial differential equation

$$\frac{d}{dx}\frac{\partial \Gamma}{\partial h'} - \frac{\partial \Gamma}{\partial h} = 0. \tag{1.4}$$

If we plug Γ in Eq. 1.4, we obtain the Young-Laplace equation for the equilibrium wetting state and it reads

$$\frac{\frac{\partial^2 h}{\partial x^2}}{\left(1+\frac{\partial h}{\partial x}\right)^{\frac{3}{2}}} = \frac{\lambda}{\gamma_{v\ell}} \tag{1.5}$$

The left hand side of Eq. 1.5 is the differential geometry definition of the mean curvature K and as visible, the mean curvature has to be constant for the functional in Eq. 1.3 to have the minimum value. Further investigation would reveal that the Lagrange multiplier λ is the Laplace pressure which accounts for the pressure jump across the curved interface and in the equilibrium state due to the constant curvature, the Laplace pressure is also constant when no other interactions are present. Unlike for systems with finite volumes, in the case of soap films, where there is no pressure jump across the interfaces, the equilibrium state is a zero mean curvature shape [6], while any finite value of volume V demands a finite mean curvature shape.

For the homogeneous flat substrate, the only obtainable constant mean curvature shape is the spherical cap shape. For the spherical cap shape under the volume constraint, the only parameter needed to describe this shape is the contact angle θ which interface closes with the substrate at the contact line. To determine the equilibrium contact angle we will again minimise the interfacial energy, but this time we will perform in it slightly different fashion. Instead of implying the volume constraint with the Lagrange multiplier, we will express the volume constraint by setting the total volume derivative to zero. Since the spherical cap shape is described with the radius of curvature R and the contact angle θ, the total volume derivative is defined as

$$dV = \frac{\partial V}{\partial R}\partial R + \frac{\partial V}{\partial \theta}\partial \theta = 0 \tag{1.6}$$

which results in

$$\frac{\partial R}{\partial \theta} = -\frac{\partial V/\partial \theta}{\partial V/\partial R} \tag{1.7}$$

Using the Eq. 1.7 we can minimise the interfacial energy by solving

$$\frac{\partial E}{\partial \theta} = \frac{\partial}{\partial \theta}\left(\gamma_{v\ell}A_{v\ell} + \left(\gamma_{s\ell} - \gamma_{sv}\right)A_{s\ell}\right) = 0 \tag{1.8}$$

Since we are considering spherical cap geometry, all of areas present in the Eq. 1.8 have the analytical geometrical definition, as does the volume V. Once we solve Eq. 1.8, we obtain the Young's law

$$\cos\theta_y = \frac{\gamma_{sv} - \gamma_{s\ell}}{\gamma_{v\ell}}, \tag{1.9}$$

where the θ_y is either called the Young's angle or the equilibrium contact angle. Very important aspect of the Young's law is it's local nature, which means that the contact line in the given position on the substrate will always have the same equilibrium contact angle, which is governed by three surface tensions present at the contact line.[1, 4, 10] Even if surface tensions γ_{sv} and $\gamma_{s\ell}$ are functions of space with finite gradients in all directions, one will obtain that the Eq. 1.9 is satisfied at every part of the contact line. Eqs. 1.4 and 1.9 are two key equations of wetting problems and the interplay between these two equations and many types of patterned substrates is a central motive for this thesis.

1.2 Guide throughout the thesis

This thesis explores the wetting effect of bubbles, droplets and solid films. *Chapter 2* focuses on the interaction between the wettting principles and the disjoining pressure on the single bubble. The disjoining pressure is interaction between two phases, which are separated by the intermediate phase. The pressure in the intermediate phase is larger due to the van der Waals interactions of atoms over the intermediate phase and due to the compressibility of the bubble, morphology starts to deform very close to the contact line. *Chapters 3,4, and 5* are focused on the droplet wetting. Inside *Chapters 3 and 4* we are dealing with wetting on both physically and chemically patterned substrates. In *Chapter 3* we have investigated experimental evidence of selective droplet nucleation on the substrate decorated with solid microcaps, while in *Chapter 4* we are interested in the direct interplay between the Young's law and the Young-Laplace equation on the elliptical lyophilic patch, where we show that due to the Young-Laplace equation the droplet might prefer spreading on the lyophobic part of the substrate, rather than on the lyophilic part. In *Chapter 5* we explore the application of a body force on the droplet and we analyse the stability of the droplet on the chemical step, when the droplet is forced to go from a lyophilic to a lyophobic part of the substrate. We discovered that the lack of possibility to satisfy either the Young-Laplace equation or the Young's law might prevent droplet from having a stable shape, however, these two different effects are occurring in different regimes of the wettability

contrast over the chemical step (difference in values of the Young's angle). *Chapters 6 and 7* are focused on the problem of the solid-state dewetting [8, 13]. Solid-state dewetting is a dynamical process of an atom surface diffusion along the interface and equilibrium states of given dynamics are identical to the ones observed in bubbles and droplets. The interplay between solid-state dewetting and patterned substrates was not even considered until few years ago. In this thesis, we present the effect of physical singularities on the solid state dewetting (*Chapter 6*) and we also conducted the first fundamental numerical research of solid-state dewetting on the chemically patterned substrate(*Chapter 7*). In *Chapter 6* we performed the analysis of the solid-state dewetting on the grooved substrate. The crucial result from this chapter is the first report of a slow and a fast way of convergence to the equilibirium, where the separation of the two regimes is the direct consequence of the contact line pinning in the physical singularity. Results from *Chapter 7* reveal that solid-state dewetting is completely a contact line driven problem and any solution of Young-Laplace equations presents an equilibrium, irrelevant of the value of the interfacial energy (whether it is global or local minimum) and the stability of equilibrium is determined rather by a position of the contact line, rather than any macroscopic aspect of the dynamics. The main thesis conclusion will be summarised in *Chapter 8*.

References

[1] S. Brandon, N. Haimovich, E. Yeger, and A. Marmur. Partial wetting of chemically patterned surfaces: The effect of drop size. *J. Colloid Interface Sci.*, 263:237–243, 2003.

[2] B. S. Clausen, J. Schiøtz, L. Gråbæk, C. V. Ovesen, K. W. Jacobsen, J. K. Nørskov, and H. Topsøe. Wetting/ non-wetting phenomena during catalysis: Evidence from in situ on-line exafs studies of cu-based catalysts. *Top. Catal.*, 1:367–376, 1994.

[3] P. G. de Gennes. Wetting: statics and dynamics. *Rev. Mod. Phys.*, 57: 827, 1985.

[4] L. Gao and T. J. McCarthy. How wenzel and cassie were wrong. *Langmuir*, 23:3762–3765, 2007.

[5] S. Herminghaus, M. Brinkmann, and R. Seemann. Wetting and dewetting of complex surface geometries. *Annu. Rev. Mater. Res.*, 38:101–121, 2008.

[6] C. Isenberg. *The science of soap films and soap bubbles.* Courier Corporation, 1992.

[7] T. Lee, E. Charrault, and C. Neto. Interfacial slip on rough, patterned and soft surfaces: A review of experiments and simulations. *Adv. Colloid*

Interface Sci., 210:21–38, 2014.

[8] F. Leroy, Ł. Borowik, F. Cheynis, Y. Almadori, S. Curiotto, M. Trautmann, J. C. Barbé, and P. Müller. How to control solid state dewetting: A short review. *Surf. Sci. Rep.*, 71:391–409, 2016.

[9] D. Lohse and X. Zhang. Surface nanobubbles and nanodroplets. *Rev. Mod. Phys.*, 87:981–1035, 2015.

[10] G. McHale. Cassie and wenzel: Were they really so wrong? *Langmuir*, 23:8200–8205, 2007.

[11] D. Quere. Wetting and roughness. *Annu. Rev. Mater. Res.*, 38:71–99, 2008.

[12] M. Rauscher and S. Dietrich. Wetting phenomena in nanofluidics. *Annu. Rev. Mater. Res.*, 38:143–172, 2008.

[13] C. V. Thompson. Solid-state dewetting of thin films. *Annu. Rev. Mater. Res.*, 42:399–434, 2012.

1

2 Effect of disjoining pressure on surface nanobubbles

In gas-oversaturated solutions, stable surface nanobubbles can exist thanks to a balance between the Laplace pressure and the gas overpressure, provided the contact line of the bubble is pinned. In this article, we analyze how the disjoining pressure originating from the van der Waals interactions of the liquid and the gas with the surface affects the properties of the surface nanobubbles. From a functional minimization of the Gibbs free energy in the sharp-interface approximation, we find the bubble shape that takes into account the attracting van der Waals potential and gas compressibility effects. Although the bubble shape slightly deviates from the classical one (defined by the Young contact angle), it preserves a nearly spherical-cap shape. We also find that the disjoining pressure restricts the aspect ratio (size/height) of the bubble and derive the maximal possible aspect ratio, which is expressed via the Young angle.[1]

[1]Based on: V. B. Svetovoy, I. Dević, J.H. Snoeijer and D. Lohse, Effect of Disjoining Pressure on Surface Nanobubbles, *Langmuir* 32:11188-11196 , 2016. Numerical work is part of the thesis

2.1 Introduction

When a solid is immersed in liquid at some conditions nanoscopic spherical-cap-shaped gaseous domains are formed at the interface. These domains, called surface nanobubbles, attracted a lot of attention recently (see reviews [1–5]). Their existence and gaseous nature has been confirmed with different methods but the main challenge was to understand the unexpectedly long lifetime of these bubbles. The surface nanobubbles exist days instead of microseconds as expected from the theory of diffusive dissolution [6]. Recently it was established that contact line pinning of the gas-liquid-solid contact line is crucial for the stability of the bubbles [7–12]. The effect of pinning originates from chemical and topographical heterogeneities of the solid surface [13–17], which are omnipresent and unavoidable. Given pinning, a stable equilibrium is achieved through the balance of Laplace pressure and gas overpressure due to oversaturation, which is also a necessary condition for stable surface nanobubbles [11, 12]. The question we want to address in this paper is: How do disjoining pressure effects – a concept introduced to extended the continuum approach down to the nanoscale (see e.g. refs. [16, 18, 19]) – modify this balance and the shape of the surface nanobubble?

It is usually assumed that the surface nanobubbles can be described by a spherical cap shape. The pressure in such a bubble is constant and equals the ambient pressure plus the Laplace pressure. For liquid drops on a solid it was already recognized [13, 20] that near the contact line the disjoining pressure contributes to the total force balance and influences the equilibrium shape of the drop. The influence of the disjoining pressure on the shape of the drops is however rather weak [21–24] and it is important only at the very edge of the drop. This need not a priori to be the case for surface nanobubbles because strong a disjoining pressure near the edge could influence the bubble as a whole due to compressibility of the gas. However, this problem was not yet addressed in detail, though the relevance of the disjoining pressure for nanobubbles and micropancakes is of course known for a long time [5, 25].

In this paper we will analyse the influence of the van der Waals interaction (i.e., the disjoining pressure) on the equilibrium shape of a free or pinned nanobubble. The paper is organized as follows. In Section 2 we shortly review the approach developed for droplets on a solid surface, then derive the equation of the force balance in presence of an external field, which is identified with the disjoining pressure, and finally construct the Gibbs free energy for the surface bubble, which can be considered as a functional of the bubble shape. Analytical solutions, which are possible for two-dimensional bubbles are analysed in Section 3. Axisymmetric bubbles are discussed in Section 4. Our conclusions are presented and summarized in the last section.

2.2 Formulation

We aim to establish the shape of surface nanobubbles under the influence of a disjoining pressure. The shape is characterised by the function $h(x, y)$ defined in Fig. 2.1. Here we derive the free energy functional $\Phi[h]$ using a sharp-interface description, from which the equilibrium equations for $h(x, y)$ can be obtained. Assuming an equilibrium implies isothermal conditions; phase transitions which may lead to local cooling are not considered. As a brief

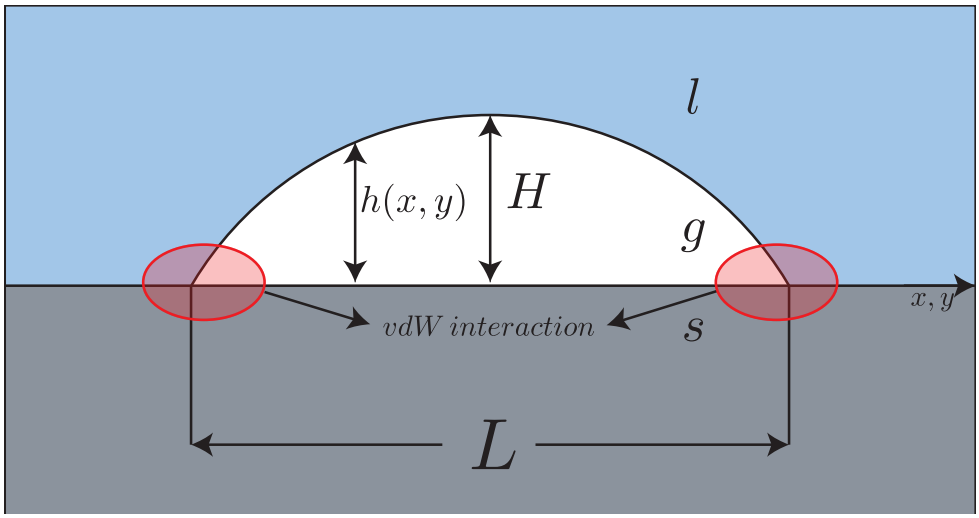

Figure 2.1: Sketch of a surface nanobubble with vdW interaction (most relevant in the corners) and definitions of the involved parameters. Different media are indicated as liquid (l), gas (g), and solid (s). The local height of the bubble $h(x, y)$ is a function of in-plane coordinates x and y. The maximal height in the center is H and the footprint size is L.

reminder, we first summarise the approach commonly used for incompressible liquid drops, which is subsequently extended to incorporate the effect of gas compressibility as is required for surface nanobubbles. We remind the reader that the sketch as express in figure 2.1 is an approximation: One could also consider a "precursor film" of the nanobubble towards the surrounding liquid, which would correspond to a local depletion of the water density in direct contact to the wall or similarly to a local gas enhancement, as were both found in molecular simulations [26, 27]. However, of course, the present sharp-interface description can not give the detailed molecular information, but the fact that such layers are observed in molecular simulations justifies this assumption of our analysis.

2.2.1 Incompressible liquid drops

For incompressible liquid drops the change of energy when changing the shape can be presented as the functional [17, 21–24]

$$\Phi[h] = \int dxdy \left[\gamma \left(\sqrt{1+(\nabla h)^2} \right) + \gamma_{sl} - \gamma_{sg} + w(h) + \lambda h \right]. \tag{2.1}$$

Here, γ is the liquid-gas surface tension and the integral gives the surface area. The contribution from a unit area of wetted substrate is $\gamma_{sl} - \gamma_{sg}$, where γ_{sl} and γ_{sg} are the surface tensions for the solid-liquid and solid-gas interfaces, respectively. $w(h)$ represents the van der Waals potential. The Lagrange multiplier λ is introduced to perform the minimisation under the constraint of a prescribed finite volume; indeed, the integral $\int dxdyh(x,y)$ represents the volume of the droplet.

On a nanoscale, i.e., for nanodrops and nanobubbles, one cannot neglect the range of molecular interactions, which are captured by the effective interface potential $w(h)$. Its influence extends to small h, where the interface is sufficiently close to the substrate. In the variational analysis, which gives the equilibrium equation for $h(x,y)$, the interface potential gives rise to an additional pressure term, $\Pi = -dw/dh$, which is the so-called disjoining pressure. In the macroscopic limit, the interface potential simply vanishes, i.e. $w(h=\infty) = 0$. We define the change in the free energy in such a way that it disappears in the "dry" state, which implies that $w(h_c) = \gamma_{sg} - \gamma_{sl} - \gamma$, where h_c is a microscopic cutoff that will be discussed explicitly below. Using Young's law for the macroscopic contact angle θ_Y, this can be written as $-w(h_c) = \gamma(1-\cos\theta_Y)$. For now, it is of key importance to note that the integral over the disjoining pressure is related to Young's contact angle θ_Y, since [21–24, 28]

$$-\int_{h_c}^{\infty} dh\,\Pi(h) = w(\infty) - w(h_c) = \gamma(1-\cos\theta_Y). \tag{2.2}$$

Indeed, droplet shapes that minimises the free energy (2.1) are very close to a spherical cap, with a macroscopic contact angle θ_Y. The Lagrange multiplier λ represents the Laplace pressure in the drop and can be tuned to achieve the desired drop volume. Only in the close vicinity of the contact line, where h falls within the range of molecular interactions, the disjoining pressure alters the droplet shape.

2.2.2 Pressure distribution in compressible gas bubbles

Let us now turn our attention to the case of *compressible* gas bubbles. The obvious first difference with respect to the droplet is that the gas and liquid

domains in Fig. 2.1 are inverted. This can be accounted for by exchanging the roles of γ_{sg} and γ_{sl}. However, upon redefining the contact angle in the gas phase (inside the bubble, so that $\gamma\cos\theta_Y = \gamma_{sl} - \gamma_{sg}$), both the formalism and the integral relation (2.2) are still valid. The key difference, however, is the gas compressibility. The energy functional should be minimised not under the constraint of constant volume, but instead we must impose the number of gas molecules N inside the bubble. Namely, surface nanobubbles are observed for a very long time [1–5], which means that the bubble can be treated as quasi static and we neglect the escape or influx of molecules due to diffusion. Due to compressibility, a constant number of molecules does not imply a constant volume, nor a constant pressure inside the bubble.

For simplicity and for specific calculations we assume that the only source of the disjoining pressure is the van der Waals (vdW) interaction, but this restriction can be easily removed if some other interactions are involved. The interaction becomes strong near the contact line between gas, liquid, and solid (see Fig. 2.1). In absence of external fields at the interface separating the liquid and gas phases temperature T and pressure P stay constant. From the thermodynamic point of view the vdW interaction can be considered as an external field acting on the gas molecules located between the opposing walls of the bubble. In a stationary external field the system becomes inhomogeneous and the pressure along the boundary is not constant anymore. Instead, the chemical potential μ as a function of temperature, pressure, and the parameters characterizing the field stays constant at the interface [29].

Thermodynamically, μ is the Gibbs free energy per molecule. In an external field it can be written as

$$\mu = \mu_0(P,T) + \phi(\mathbf{r}), \tag{2.3}$$

where $\mu_0(P,T)$ is the chemical potential in absence of the field and $\phi(\mathbf{r})$ is the field potential per molecule, which depends on the position of the molecule $\mathbf{r}$. The bubble will be in the mechanical equilibrium if $\mu = const$ along the gas-liquid interface. Differentiating (2.3) with respect to the space coordinates we can find the force balance at the interface:

$$\frac{\nabla P}{n(P,T)} + \nabla\phi(\mathbf{r}) = 0, \tag{2.4}$$

where $n(P,T)$ is the gas concentration in the bubble and we made use of the thermodynamic relation $(\partial\mu/\partial P)_T = n^{-1}(P,T)$.

As was already mentioned, we assume for definiteness that the opposing walls of the surface nanobubble attracts each other with a force per unit area, which originates only from the vdW interaction between solid and liquid

molecules via the gas gap. This force is

$$\Pi(h) = -\frac{A_H}{6\pi h^3}, \tag{2.5}$$

where $A_H \sim 10^{-20}$ J is the Hamaker constant between liquid, gas, and solid and $h = h(x, y)$ is the local distance between the walls as shown in Fig. 2.1. In the more general case [28] the vdW interaction is not the only contribution to the disjoining pressure $\Pi(h)$. The local distance h is going to zero in the corners, where the pressure (2.5) diverges. In reality this divergence is regularised by hard-core repulsion. Such a regularisation is also critical in view of (2.2), since the disjoining pressure in (2.5) cannot be integrated to $h = 0$; this was the reason for introducing a cut-off distance h_c. To control the effect of the cutoff, we explicitly include a repulsive contribution to the disjoining pressure, as

$$\Pi(h) = \frac{A_H}{6\pi h^3}\left[\left(\frac{h_c}{h}\right)^6 - 1\right]. \tag{2.6}$$

This pressure is motivated by the body-body Lennard-Jones interaction [30, 31]. At $h = h_c$ the repulsive and attractive contributions are equal and the disjoining pressure becomes zero. We note that in eq. (2.6) we have neglected the contribution of spatial partial derivatives to $\Pi(h)$, which in general [19] also depends on $\partial_x h$ and $\partial_{xx} h$, where x represents a spatial coordinate. Given that the contact angle of surface nanobubbles is small this approximation is justified.

It has to be noted that the pressure (2.5) or (2.6) is defined between parallel plates, which is not the case for the bubble walls. We can apply this equation locally by changing the curved surface by flat patches parallel to the substrate. This is the idea of the proximity force approximation [32] (PFA) that is widely used in analysis of the dispersion forces (see recent review [33]). Application of PFA is justified if the curvature radius of interacting surfaces is much larger than the distance between them. In our case this condition reads $8H^2/(L^2 + 4H^2) \ll 1$. It will be assumed here that the condition holds true. However, there is no principal problem if the condition is broken. It just means that the specific functional behavior (2.5) or (2.6) is changed. Then a more complicated expression has to be used but one can apply numerical (see review [34]) and sometime analytical [35] methods to determine the function $\Pi(h)$.

Attraction of the bubble walls results in an extra pressure (disjoining pressure) experienced by a gas molecule. Due to this pressure the chemical potential at a constant temperature changes on $\Pi(h)v$, where $v = n(P,T)^{-1}$ is the volume per molecule (molar volume). Therefore, the external potential ϕ in Eq. (2.3) can be presented as

$$\phi(\mathbf{r}) = \frac{\Pi(h)}{n(P,T)}, \tag{2.7}$$

where both h and P are functions of the in-plane coordinates x, y. The functional dependence of pressure one can find by substituting ϕ into the equation (2.4) of the force balance and expressing the concentration via the pressure with the help of the equation of state: $n(P,T) = P/kT$. For simplicity we use here the equation of state for ideal gas, which can be generalized if necessary. The resulting equation on the coordinate dependence of the pressure is

$$\frac{\nabla P}{P} + \nabla\left(\frac{\Pi(h)}{P}\right) = 0. \tag{2.8}$$

It can be integrated to find an implicit dependence of P on the local height $h(x,y)$:

$$P\ln(P/P_0) = -\Pi(h), \tag{2.9}$$

where P_0 is the pressure in the bubble if the interaction is switched off ($A_H \to 0$), or when the bubble height reaches macroscopic distances outside the range of molecular interactions. This relation shows explicitly that the pressure in the bubble is not homogeneous. Note that the Hamaker constant for liquid-gas-solid system is always positive, so the pressure in the bubble is always larger than P_0.

The pressure P as a function of the local height h is shown in Fig. 2.2. It is defined by two independent parameters. One is the cutoff distance that has typical value $h_c \approx 0.2\,\text{nm}$ [36]. The second independent parameter is $\beta = A_H/6\pi h_c^3 P_0$. At large heights $h \gg h_c$ the pressure approaches asymptotically P_0, it has maximum at $h = 3^{1/6}h_c$, and decreases up to P_0 at $h = h_c$.

2.2.3 Gibbs free energy for compressible gas bubbles

The thermodynamics of coexistence of different phases in external fields was considered in [37] for a number of physical systems. We construct here the Gibbs free energy $\Phi[h]$ as a functional of the bubble shape $h(x,y)$, which consists of volume and surface contributions. The volume contribution is just the sum of the chemical potentials μ for all the gas molecules inside of the bubble:

$$\Phi_V[h] = \int_V d^3x\, \mu(P,T,h)n(P,T). \tag{2.10}$$

We assume here a sharp interface between liquid and gas (sharp-kink approximation [22]). In this case the integrand does not depend on the vertical coordinate z and the corresponding integration can be done explicitly. The

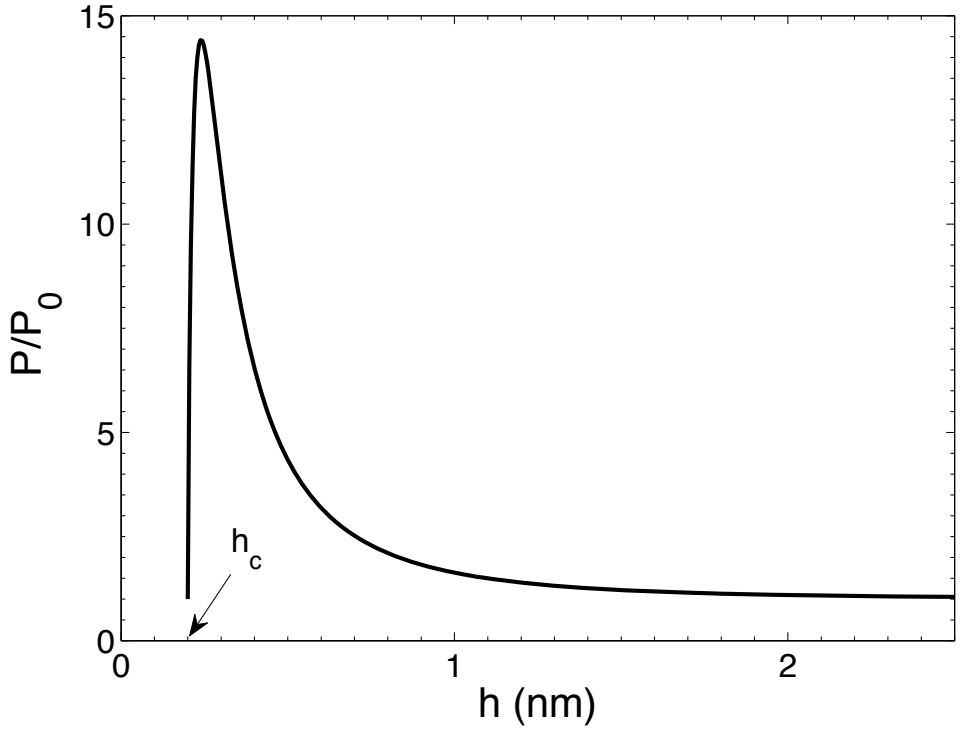

Figure 2.2: Pressure as a function of the local height for the disjoining pressure (2.6). The curve is given for the parameters $h_c = 0.2\,\mathrm{nm}$ and $A_H/6\pi h_c^3 P_0 = 100$.

lower integration limit $z = 0$ corresponds to the solid-gas interface and the upper limit $z = h$ is at the gas-liquid boundary. Expressing $n(P,T)$ via the equation of state and using the condition $\mu = const$ we find

$$\Phi_V[h] = -\kappa \int dxdy\, hP(h), \tag{2.11}$$

where $\kappa = -\mu/kT$ is an unknown constant, $P(h)$ is the solution of Eq. (2.9), and the integral is running over the bubble footprint in the $x-y$ plane. The right hand side of Eq. (2.11) is proportional to the number of molecules in the bubble. The constant κ plays the role of a Lagrange multiplier that imposes the desired number of molecules. Importantly, since the pressure $P(h)$ is *not* constant inside the bubble, this constraint is fundamentally different from the incompressible case, for which the constraint involves the volume $\int dxdy\, h$.

The surface contribution to the Gibbs potential $\Phi_S[h]$ can be written as

$$\Phi_S[h] = \int dxdy \left[\gamma\sqrt{1+(\nabla h)^2} + \gamma_{sg} - \gamma_{sl} + w(h)\right]. \tag{2.12}$$

This is in direct analogy to (2.1) for droplets, except for the interchange between γ_{sg} and γ_{sl} due to the inversion of the liquid and gas phases. The

explicit form of the potential in the case of the Lennard-Jones model is

$$w(h) = \frac{A_H}{12\pi h^2}\left[\frac{1}{4}\left(\frac{h_c}{h}\right)^6 - 1\right]. \tag{2.13}$$

Let us stress that the contributions of the interaction to Φ_S and Φ_V are independent. The first one will exist even for a bubble filled with vacuum, while the contribution to Φ_V is related to the gas molecules.

As a result, the total Gibbs free energy can be presented as

$$\Phi[h] = \Phi_V[h] + \Phi_S[h] = \int dxdy\left[\gamma\left(\sqrt{1+(\nabla h)^2} - 1\right) + U(h)\right], \tag{2.14}$$

where using $\gamma(1-\cos\theta_Y) = -w(h_c)$ we introduced the "effective potential"

$$U(h) = w(h) - w(h_c) - \kappa h P(h). \tag{2.15}$$

In combination with (2.9) and (2.13), this fully specifies the energy functional for compressible gas bubbles. In the next sections this functional will be minimized to determine bubble shapes $h(x,y)$.

2.3 Two-dimensional bubble

We first consider the shape of a two-dimensional (2D) bubble, which is homogeneous in the y-direction. In this case the shape $h(x)$ can be obtained analytically, and is sufficient to reveal the essential physics. After deriving the general solution, we consider the bubbles with and without pinning. We highlight geometrical features and identify a bound on the aspect ratio for pinned bubbles.

2.3.1 General solution

The minimisation procedure can be made using the Euler-Lagrange method. Namely, for the two-dimensional problem the functional (2.14) reduces to the form

$$\Phi[h] = \int dx\,\Gamma(h,h'), \tag{2.16}$$

with the energy per unity length

$$\Gamma(h,h') = \gamma\left(\sqrt{1+h'^2} - 1\right) + U(h). \tag{2.17}$$

This is the equivalent to a Lagrangian in classical mechanics, in which case the variable is time instead of the spatial coordinate x. Minimisation of the functional leads to the Euler-Lagrange equations

$$\frac{d}{dx}\frac{\partial \Gamma}{\partial h'} = \frac{\partial \Gamma}{\partial h} \tag{2.18}$$

and yields the equilibrium equation

$$\gamma\left(\frac{h'}{\sqrt{1+h'^2}}\right)' = \frac{dU}{dh} = -\Pi(h) - \kappa\frac{d}{dh}\left[hP(h)\right]. \tag{2.19}$$

The left hand side is the Laplace pressure, surface tension times curvature, while the right hand side contains the disjoining pressure and a term allowing for a finite number of molecules N.

The bubble shape is thus determined by a second order ordinary differential equation (ODE), which contains κ as an unknown parameter. As boundary conditions we impose a height H at the bubble centre, where due to symmetry one also has $h'(0) = 0$, i.e.

$$h(0) = H, \quad h'(0) = 0. \tag{2.20}$$

This means that a solution can be generated for each value of κ: by varying κ one finds bubble shapes that contain a varying number of molecules. We anticipate that a unique equilibrium solution is obtained when assuming that there is no pinning of the contact line.

Since in the 2D case the functional does not depend explicitly on x, one can find a first integral of Eq. (2.19) [24]. It reads

$$\mathcal{E} = h'\frac{\partial \Gamma}{\partial h'} - \Gamma = \gamma\left(1 - \frac{1}{\sqrt{1+h'^2}}\right) - U(h), \tag{2.21}$$

where $\mathcal{E}$ is a constant. Again, there is a direct analogy with classical mechanics, where the homogeneity in time enables a first integral of the equation of motion, which expresses the conservation of energy. The analysis is now reduced to (2.21), a first order ODE with $\mathcal{E}$ and κ as unknown parameters. The value of $\mathcal{E}$ can be eliminated using the boundary conditions (2.20). This reduces (2.21) to

$$\gamma\left(1 - \frac{1}{\sqrt{1+h'^2}}\right) = \Delta U(h), \tag{2.22}$$

where the potential energy difference is introduced

$$\Delta U(h) = U(h) - U(H). \tag{2.23}$$

An important observation here is that a solution exists only if ΔU is not negative over the entire bubble. In the domain $0 \leq x < \infty$, the solution can be presented in an implicit form

$$x = \int_h^H \frac{dh(\gamma - \Delta U)}{\sqrt{\Delta U(2\gamma - \Delta U)}}, \tag{2.24}$$

where all the conditions at $x = 0$ are already satisfied. Note that via eq. (2.15) and $U(h)$ respective $\Delta U(h)$ κ still appears as a parameter, allowing for a family of bubble shapes.

2.3.2 Homogeneous substrate: no pinning

Let us first consider the case where there is no pinning at the contact line, which leads to the true equilibrium solution. For the disjoining pressure (2.6), the balance of attraction and repulsion leads to a solution where the bubble has a precursor film that extends to $x \to \pm\infty$. The film thickness h^* can be determined from the condition $h' = 0$ inside the film. According to (2.22) this implies $\Delta U(h^*) = 0$, and for a given value of H this selects a unique value of κ, and consequently the number of molecules. Note that in the limit of large bubbles $H \to \infty$, much larger than the range of interaction, one has $U(H) \to 0$, which implies that the precursor film thickness $h^* \to h_c$. For small bubbles, the precursor film is a bit larger than h_c.

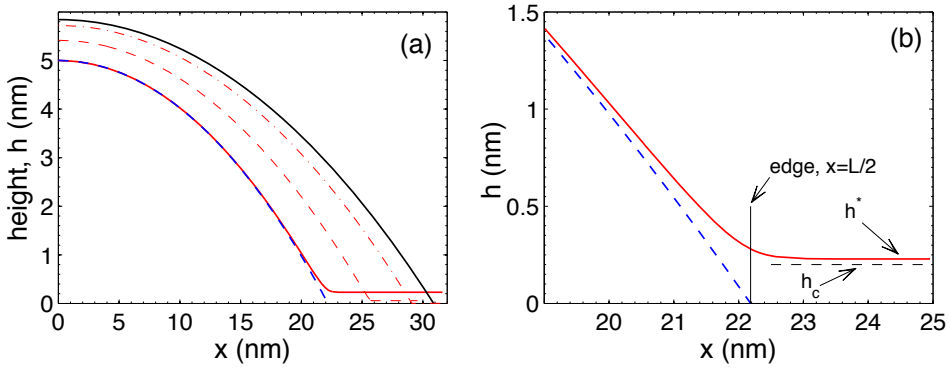

Figure 2.3: (a) 2D nanobubble on a homogeneous substrate (solid red curve) with a height of $H = 5\,\text{nm}$. The dashed blue curve shows the cylindrical cap of an equivalent size L given by Eq. (2.25). The black curve presents a classical bubble (i.e., a bubble in the macroscopic description where the influence of the disjoining pressure is replaced by a perfectly localised contact angle boundary condition) containing the same number of molecules. The dashed and dash-doted red curves correspond to the reduced interaction with the scaling factors (see text) $\lambda = 4$ and 256, respectively. (b) shows a zoom of the figure near the bubble edge, indicating important parameters as explained in the text.

The existence of the precursor film means that h relaxes to h^* at infinity, and thus the bubble formally extends over the entire domain. Still, we wish to determine a lateral bubble size L. Here we do this by equating the curvature radius at the top of the bubble to a cylindrical cap, which is the solution for a macroscopic bubble without disjoining pressure. With a cylindrical segment of radius of curvature R this implies the geometrical connection

$$-\frac{\gamma}{R} = \left.\frac{dU}{dh}\right|_{h=H}, \quad R = \frac{(L/2)^2 + H^2}{2H}, \tag{2.25}$$

which effectively defines L.

The shape of a bubble with height $H = 5\,\mathrm{nm}$ is shown in Fig. 2.3a by the solid (red) curve. We took as typical parameters $\gamma = 0.072\,\mathrm{J/m^2}$, $h_c = 0.2\,\mathrm{nm}$, and $A_H = 1 \times 10^{-20}\,\mathrm{J}$. According to Eq. (2.2) these parameters correspond to $\theta_Y = 21.4°$. The blue dashed curve is given by Eq. (2.25). It defines the cylindrical cap of an equivalent size L. Note that the cap practically coincides with the actual bubble except of the very edge. We found the bubble size and the precursor film thickness to be $L \approx 44.4\,\mathrm{nm}$ and $h^* \approx 0.23\,\mathrm{nm}$, respectively. The detailed behavior near the edge is shown in fig. 2.3b, where the bubble edge is marked by the vertical line and the cutoff distance is indicated by the dashed horizontal line. Above the physical edge the bubble quickly reaches the asymptotic height h^*.

It is interesting to emphasise the effect of the interaction on the bubble size. The bubble that was found by the minimization of the Gibbs free energy (2.16) can be compared with a classical bubble that has the contact angle θ equal to the Young angle, $\theta = \theta_Y$, and contains the same number of molecules N. These two conditions completely define the classical bubble, which is shown by the black curve in the same figure. It has the lateral size $L^{cl} = 62.2\,\mathrm{nm}$ and height $H^{cl} = 5.9\,\mathrm{nm}$. There is a difference between bubbles with and without interaction potential. This difference is the combined effect of the disjoining pressure and the gas compressibility. How these factors influence the shape and size of the bubble has to be discussed qualitatively.

The pressure in the classical (2D) bubble is estimated as $P_0^{cl} = P_a + \gamma/R^{cl} \approx 9.46\,\mathrm{bar}$, where $P_a \approx 1\,\mathrm{bar}$ is the ambient pressure and $R^{cl} \approx 85.1\,\mathrm{nm}$ is the curvature radius of the classical bubble. The pressure in the bubble with the vdW interaction is distributed inhomogeneously as shown in Fig. 2.2. In the center it is approaching $P_0 \approx 14.92\,\mathrm{bar}$ and sharply increases near the edges. This inhomogeneous pressure distribution can be responsible only for small part of the difference between the bubbles. The number of molecules $dN/dx \sim h(x)P(h)$ in the interval dx is shown in Fig. 2.4(a). For comparison the same value $dN/dx \sim h(x)$ is given for the homogeneous pressure $P(h) = P_0$ in the bubble. As one can see dN/dx near the edge is larger than in the

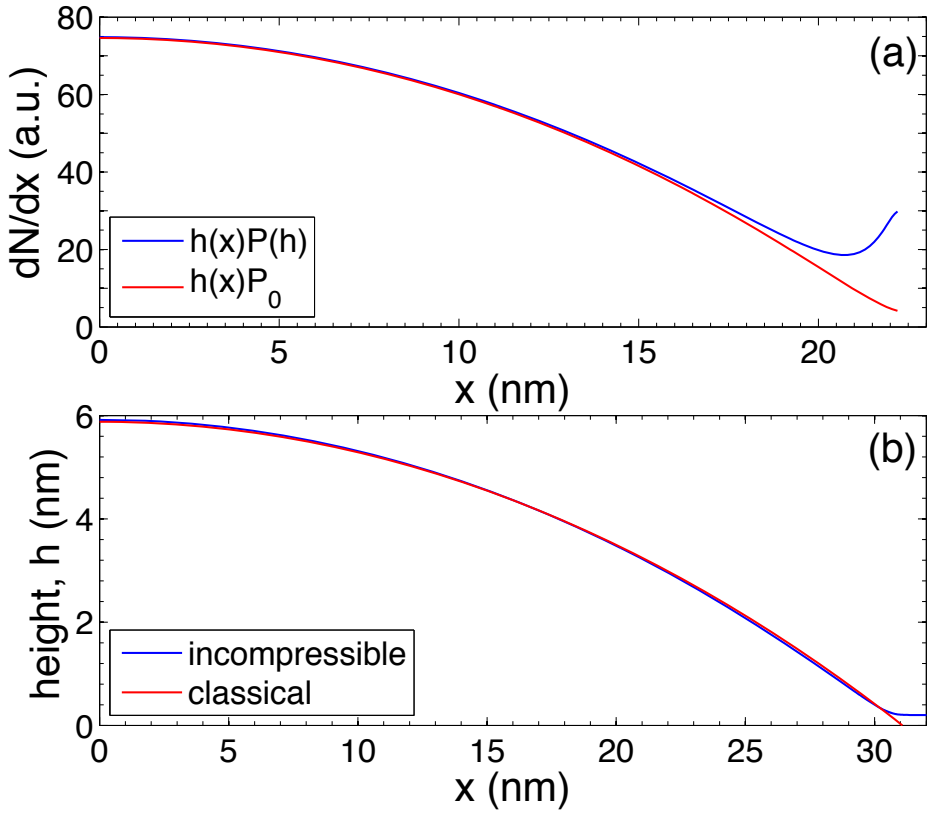

Figure 2.4: (a) Distribution of the number density dN/dx of molecules per length dx as a function of the lateral coordinate x. The blue curve presents the distribution in the actual bubble. The red curve is for an imaginary bubble with homogeneous pressure distribution $P(h(x)) = P_0$. (b) Bubble shape for an incompressible "gas" in comparison with the classical bubble.

case of the homogeneous pressure but the integral difference in the number of molecules is just 3%.

In the classical bubble the vdW interaction is contracted to a line that is the contact line. Without pinning this line can move freely. If the interaction has a finite distance range the contact line moves inward to balance the distributed forces. When the interaction range increases the classical bubble will shrink more and more. To be sure that this is the case let us rescale the distances $h \to \lambda h$ in the potential (2.13), where λ is a scaling factor. This rescaling can be absorbed by the change of the parameters: $A'_H = A_H/\lambda^2$ and $h'_c = h_c/\lambda$. Note that this transformation preserves the basic relation (2.2). With this transformation we can change the magnitude of interaction (or equivalently the range of interaction) but keep the same θ_Y. The case $\lambda \to \infty$ corresponds to the classical bubble. In Fig. 2.3 the bubbles for $\lambda = 4$ and $\lambda = 256$ are presented by dashed and dash-dotted curves, respectively. The actual bubble corresponds to $\lambda = 1$. An important observation is that the bubble approaches

the classical shape rather slowly when λ increases.

It is possible to check also what happens if the bubble is filled in with an imaginary medium that is an incompressible "gas". For that one has to return to Eqs. (2.4) and (2.7), where we cannot use the equation of state and have to keep the concentration as a constant: $n(P,T) = n_0$. The only change in the Gibbs free energy is the volume term in the effective potential (2.15) $\kappa h P(h)$ that has to be changed by $\kappa h P_n$, where $P_n = kTn_0$ is a constant with the dimension of pressure. The resulting functional, of course, coincides with that for drops (2.1). The parameter P_n was chosen to be equal to the pressure in the classical bubble P_0^{cl}. The condition of constant number of molecules is equivalent to the condition of constant volume. The result is presented in Fig. 2.4(b). One can see that the bubble is practically coincides with the classical bubbles except for the behavior near the very edge. Moreover, even the small difference quickly disappears with the increase of the scaling factor λ.

We can conclude that the contraction of the bubble in comparison with the classical one in Fig. 2.3 is the result of both the finite interaction range and the gas compressibility.

2.3.3 Pinned bubble

If the substrate is not homogeneous the bubble size can be determined by the effect of pinning. Pinning of the contact line keeps the lateral extension L so as the footprint area of the bubble fixed. This is a crucial assumption for stability of the surface nanobubbles [7–12]. In this paper we assume that the bottom of the bubble is homogeneous and the inhomogeneities happen at the contact line. This is a reasonable assumption because anyway the interaction is important very close to the bubble edge. Within this approach we cannot, however, describe the effect of contact angle hysteresis, which is also related to inhomogeneities on the surface [18, 38]. To describe the hysteresis we have to explicitly introduce the dependence of the Hamaker constant on the $x-y$ coordinates.

According to Eq. (2.22) the bubble is defined by the function $\Delta U(h)$, which via eq. (2.15) depends on the parameter κ. This function for three different values of κ is shown in Fig. 2.5. At $h = H$ the function is zero by definition. It has a maximum when the disjoining pressure becomes comparable with the Laplace pressure. At even smaller heights it has also a minimum when the repulsive interaction becomes comparable with the attraction. Solutions of Eq. (2.22) exist only for $\Delta U(h) \geq 0$. There is a minimal value of κ such that for every $\kappa < \kappa_{min}$ the function ΔU becomes negative and solutions cease to exist. This minimal value is defined by the same condition $\Delta U(h^*) = 0$ we

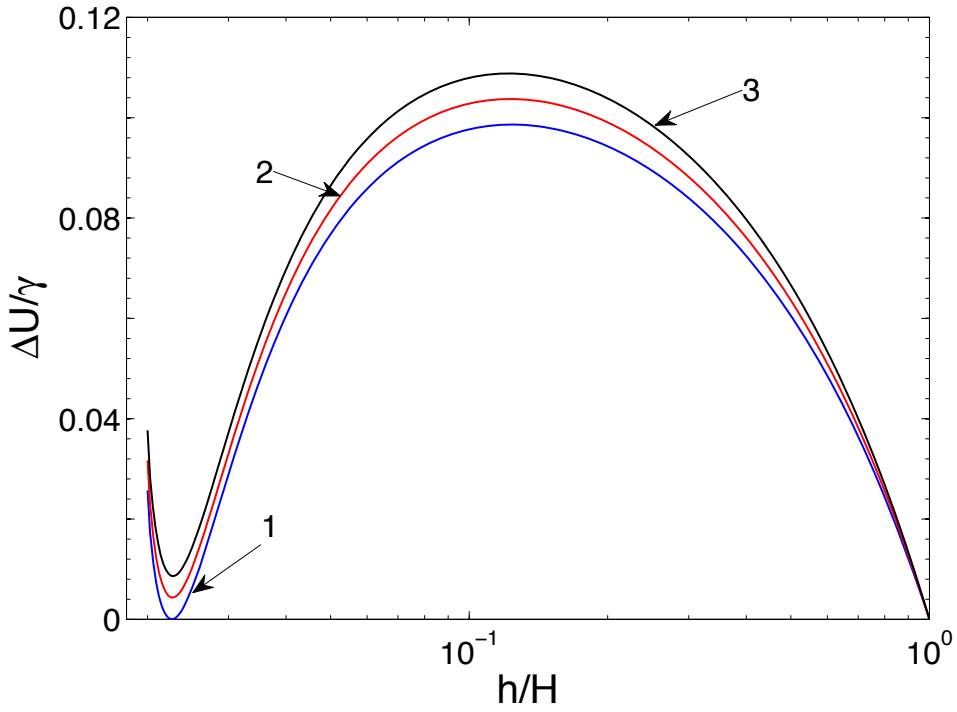

Figure 2.5: Function $\Delta U(h)$ in units of γ for $H = 5\,\text{nm}$ and $A_H = 1.36 \times 10^{-20}\,\text{J}$. Curve 1 corresponds to the case $\kappa = \kappa_{min}$, which describes the bubble on a homogeneous substrate. Curves 2 and 3 correspond to $\kappa = 1.05\kappa_{min}$ and $\kappa = 1.1\kappa_{min}$, respectively.

used to determine the "unpinned" shape. Hence the critical case coincides with the homogeneous unpinned bubble. Expressing κ_{min} from the condition $\Delta U(h^*) = 0$ we find

$$\kappa_{min} = \frac{w(H) - w(h^*)}{HP(H) - h^*P(h^*)}, \tag{2.26}$$

where, as before, h^* is the precursor film thickness. The critical function (curve 1) touches the horizontal axis in one point $h = h^*$. Because the solution (5.12) is singular in this point, it can be reached only at infinity ($x \to \infty$) so that the domain of heights $h_c < h < h^*$ is not accessible. When $\kappa > \kappa_{min}$ the minimum is positive and all the heights $h_c < h < H$ are available. The functions $\Delta U(h)$ for $\kappa = 1.05\kappa_{min}$ and $1.10\kappa_{min}$ are presented by the curves 2 and 3, respectively.

Three pinned bubbles of the same height $H = 5\,\text{nm}$ and different size are shown in Fig. 2.6. The curve 1 shows the bubble, which is very close to the critical one. It corresponds to $\delta\kappa = \kappa - \kappa_{min} = 1 \times 10^{-4}$, where $\kappa_{min} = 0.9412$. The size of this bubble $L = 43.8\,\text{nm}$ is very close to that for the critical bubble. One can see a distinctive shoulder that remains from the critical bubble but has now a finite length. The curves 2 and 3 are presented for $\delta\kappa = 0.01$ and 0.02, respectively. The bubble sizes in these cases $L = 39.8\,\text{nm}$ and $35.2\,\text{nm}$

are smaller than for the critical bubble as was expected. It has to be stressed that for pinned bubbles one cannot demand the continuity of the gas-liquid interface. At the point of pinning this continuity is broken due to presence of external pinning forces. This is why the derivative h' stays constant in the last point of the bubble in contrast with the bubble on the homogeneous substrate.

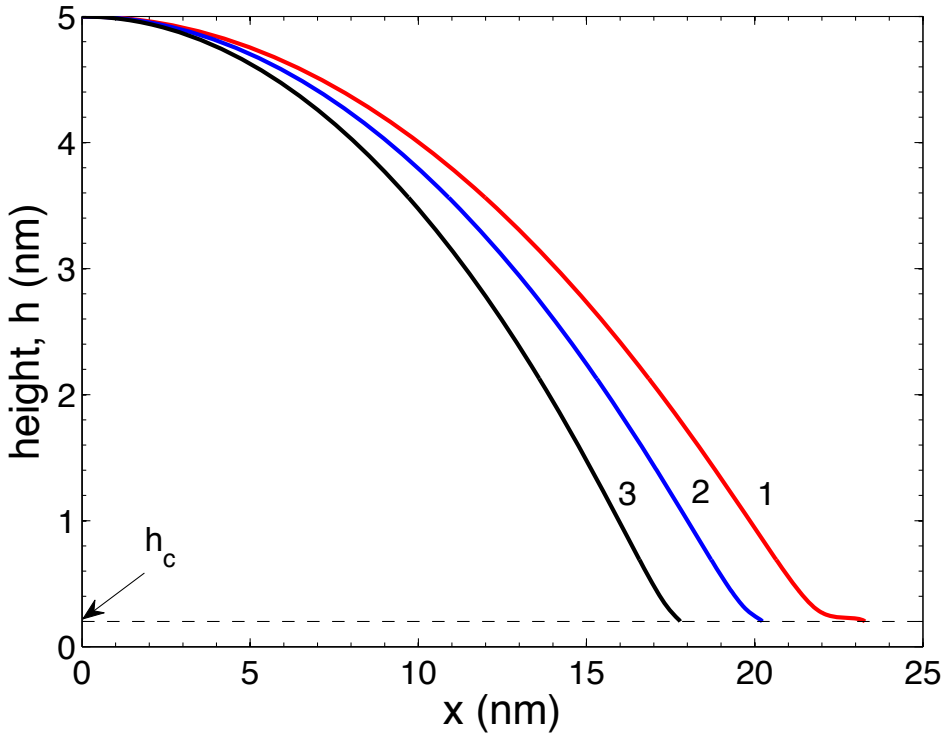

Figure 2.6: Pinned bubbles at a fixed height $H = 5\,\text{nm}$ and Hamaker constant $A_H = 1 \times 10^{-20}\,\text{J}$ for three different values of $\delta\kappa = \kappa - \kappa_{min}$. The curves 1, 2, and 3 correspond to $\delta\kappa = 1 \times 10^{-4}$, 0.01, and 0.02, respectively.

2.3.4 Critical aspect ratio

With the increase of κ the bubble size decreases as one can see from Fig. 2.6 or deduce from Eq. (2.25). It means that the bubble with $\kappa = \kappa_{min}$ corresponds to the largest possible bubble for a given height and Hamaker constant. In this sense we call this bubble a critical bubble. Therefore, the interaction restricts the aspect ratio $\mathcal{R} = L/H$ of the surface nanobubbles: with the increase of $\mathcal{R}$ the surface tension cannot sustain anymore the increasing interaction. The largest aspect ratio $\mathcal{R}_{cr}$ is realized for the critical bubble. Figure 2.7 shows $\mathcal{R}_{cr}$ as a function of the bubble height H for three different values of the Hamaker constant. Actually instead of A_H we have used in the figure an equivalent parameter θ_Y, which is related to A_H by Eq. (2.2). When H becomes large

$\mathcal{R}_{cr}$ saturates at the values shown by the dashed lines. This limit can be found analytically.

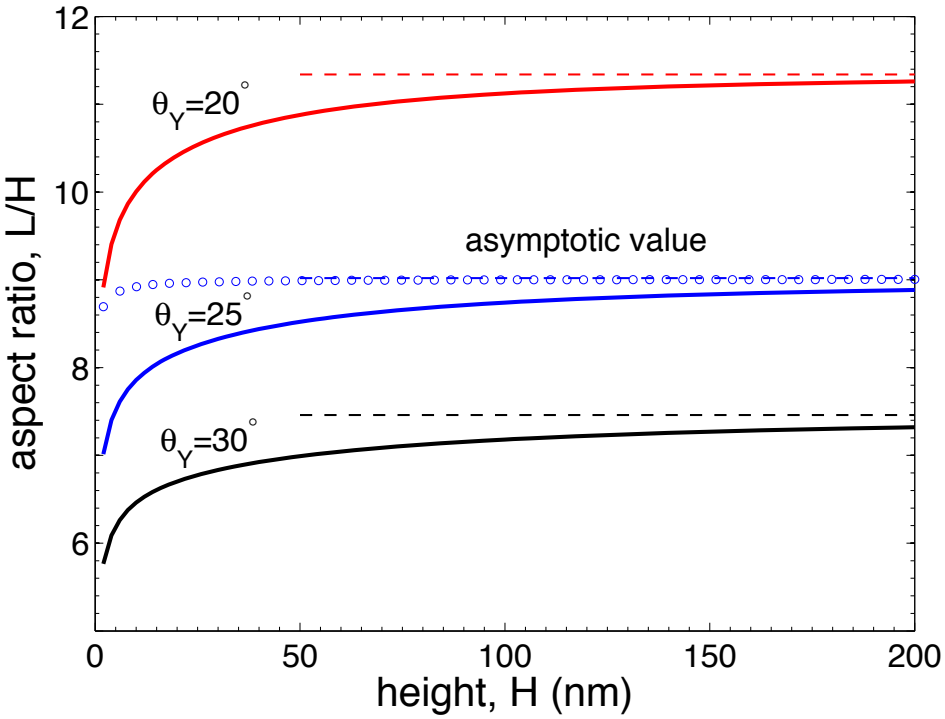

Figure 2.7: Critical aspect ratio L/H for different Hamaker constants $A_H = 0.87, 1.36, 1.97 \times 10^{-20}$ J, which are equivalent to Young's angles $\theta_Y = 20^o, 25^o, 30^o$. The curve shown by open circles was calculated with $\theta_Y = 25^\circ$ for an incompressible "gas". The dashed lines give the asymptotic values ($H \to \infty$) for the critical aspect ratios.

As we already mentioned at $H \to \infty$ the precursor film thickness is reduced to $h^* \to h_c$ and pressure $P(h^*) \to P_0$. Then for κ_{min} in this limit we find from (2.26)

$$\kappa_{min} \to -\frac{w(h_c)}{HP_0}, \quad H \to \infty. \tag{2.27}$$

The aspect ratio in the same limit can be determined from Eq. (2.25). At the top of a large bubble the interaction does not contribute and we find $dU/dh|_{h=H} \to -\kappa P_0$. Substituting to Eq. (2.25) together with $\kappa = \kappa_{min}$ we find for the critical aspect ratio

$$\mathcal{R}_{cr} \to 2\sqrt{\frac{1+\cos\theta_Y}{1-\cos\theta_Y}}, \quad H \to \infty, \tag{2.28}$$

where instead of the potential $w(h_c)$ we introduced the contact angle according to the relation $\gamma(1-\cos\theta_Y) = -w(h_c)$. It has to be stressed that this aspect

ratio is equivalent to the classical boundary condition: the contact angle is equal to Young's angle, $\theta(L/2) = \theta_Y$, where $\theta(L/2)$ is the contact angle at the bubble edge.

For small heights the critical aspect ratio $\mathcal{R}_{cr}$ deviates from the classical limit (2.28) as Fig. 2.7 demonstrates. For example, even for $H = 200\,\text{nm}$ the deviation from the classical limit is above 2%. Such a strong sensitivity to the interaction was already stressed for the bubbles with a fixed number of molecules and it is related to the compressibility of the gases. We did similar calculations for an incompressible "gas" keeping all the other properties of the gas unchanged. The result is strikingly different as demonstrated by the curve shown by the open circles. In this case 2% deviation is reached only for "bubbles" with the height $H < 5\,\text{nm}$.

2.4 Axisymmetric bubble

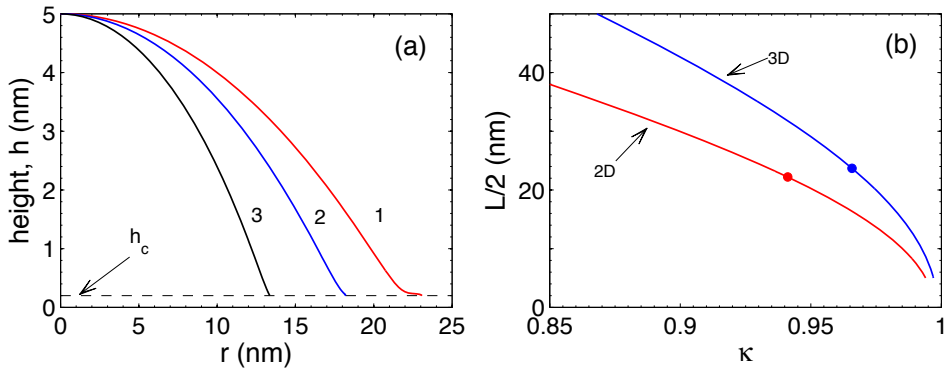

Figure 2.8: (a) Pinned axisymmetric bubbles for three different values of $\delta\kappa = \kappa - \kappa_{min}$ at fixed H and A_H. The curves 1, 2, and 3 corresponds to $\delta\kappa = 1 \times 10^{-4}$, 0.01, and 0,02, respectively. (b) The dependence of the size L on κ for 2D and 3D cases. The dots correspond to $\kappa = \kappa_{min}$.

In the previous section a significant part of the analysis was done analytically that simplified understanding of the physical picture. In the case of axisymmetric bubbles the possibility of an analytical treatment is restricted but we can use the physical intuition developed in the previous section for interpretation of the results.

Variation of the total Gibbs free energy (2.14) results in the equation on the shape of an axisymmetric bubble:

$$\frac{\gamma}{r}\left(r\frac{h'}{\sqrt{1+h'^2}}\right)' = \frac{dU}{dh}, \tag{2.29}$$

where $h = h(r)$ is a function of the in-plane radius r and "prime" means the derivative with respect to r. As in the case of 2D bubbles the boundary conditions at the top of the bubble are $h(0) = H$ and $h'(0) = 0$. For the axisymmetric bubble the problem cannot be solved analytically because Eq. (2.29) does not have a first integral similar to (2.21).

We expect that on a homogeneous substrate there is a continuous transition at infinity to a precursor film of thickness h^*, $h \to h^*$. Then the boundary condition at $r \to \infty$ is $h' \to 0$. Continuity demands also that the curvature at infinity has to be zero that is equivalent to the condition $dU/dh \to 0$. Then asymptotically at large r Eq. (2.29) is linearized

$$h'' + \frac{h'}{r} = \frac{B}{\gamma}(h - h^*), \tag{2.30}$$

where B is a constant defined by the effective potential ΔU. The solution of this equation is proportional to the modified Bessel function $K(r\sqrt{B/\gamma})$, which asymptotically at large r has the form

$$h(r) = h^* + \frac{A}{\sqrt{r}} \exp\left(-r\sqrt{B/\gamma}\right), \quad r \to \infty, \tag{2.31}$$

where A is an integration constant. The situation here is completely similar to that for the 2D bubble on the homogeneous substrate. The height $h = h^*$ can be reached only at $r \to \infty$. On the other hand, the physical size L is determined by the equation similar to (2.25) with an additional factor 2 on the left hand side, which reflects the existence of the two principal curvatures.

The problem was solved numerically using Runge-Kutta method with the "initial" conditions $h(0) = H$ and $h'(0) = 0$. The parameter κ was chosen to satisfy the condition $h' \to 0$ at infinity. This bubble describes the critical bubble, which corresponds to the minimal value $\kappa = \kappa_{min}$. Any bubble with larger κ but with the same height and Hamaker constant is a pinned bubble. Figure 2.8 shows three bubbles for $H = 5\,\text{nm}$ and $A_H = 1 \times 10^{-20}\,\text{J}$ corresponding to different values of κ. The bubble shown by the curve 1 is close to the critical one and corresponds to $\delta\kappa = \kappa - \kappa_{min} = 1 \times 10^{-4}$, where $\kappa_{min} = 0.9658$. The curves 2 and 3 are given for $\delta\kappa = 0.01$ and 0.02, respectively. In comparison with a similar Fig. 2.6 for the 2D case one can see that the bubble size decreases faster with the increase of κ. It has pure geometrical reason. In the inset the dependence of the bubble size on κ, which follows from Eq. (2.25), is shown for both 2D and 3D cases. The minimal κ are indicated by the dots on each curve. The difference between the 2D and 3D curves originates from different factors in the Laplace pressure (1 vs 2). Nearby $\kappa = \kappa_{min}$ the derivative $dL/d\kappa$ is larger for the 3D case. This explains faster variation of L with κ.

The critical aspect ratio as a function of bubble height for axisymmetric bubbles is shown in Fig. 2.9 for three different values of Young's (or three different Hamaker constants). Since in the classical limit $H \to \infty$ the same relation (2.28) for $\mathcal{R}_{cr}$ holds true, the asymptotic limits shown by thin dashed lines are the same as for the 2D case. One can see that the curves behave similar to those for the 2D case. However, for axisymmetric bubbles the transition to the classical limit happens even more slowly. This is again related to the geometrical reason.

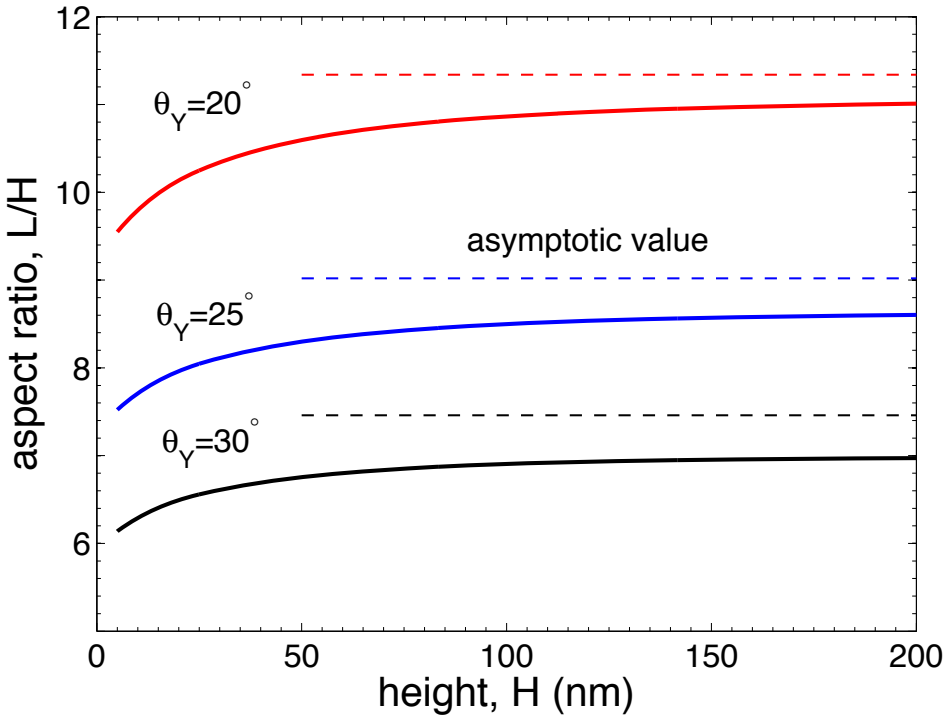

Figure 2.9: Critical aspect ratio for the axisymmetric bubble as a function of the bubble height. Three presented curves correspond to different Young's angles $\theta_Y = 20,\ 25$, and 30° (different Hamaker constants). Thin dashed lines define the classical limit for each Young's angle.

2.5 Conclusions

In this paper we considered influence of the disjoining pressure on the shape, aspect ratio, and pressure distribution inside of the surface nanobubbles. The disjoining pressure was considered as an external field for the thermodynamic characteristics of the gas filling the bubble. This external field is the reason for inhomogeneous pressure distribution in the bubble. We characterized the

bubble with the Gibbs free energy that includes the standard surface contribution and nontrivial volume contribution. The latter took into account the gas compressibility with nonuniform pressure distribution. Minimization of the Gibbs free energy allowed for the determination of all the characteristics of the bubble.

The resulting bubble shape slightly deviates from the classical bubble (defined by the Young contact angle θ_Y) with the same number of molecules, but preserves nearly spherical-cap shape. The deviation is a combined effect of the finite interaction range and the gas compressibility. We found that for a fixed Hamaker constant the bubble aspect ratio L/H (size/height) has to be smaller than a critical value $\mathcal{R}_{cr}(H)$, which depends on the bubble height H. Due to the interaction the bubble with a small height cannot exist. For large bubbles ($H \to \infty$) the critical aspect ratio approaches that given by the Young contact angle. We found deviations from this classical limit and established that this effect is related to the gas compressibility. Finally we stress that the physical idea and the main finding of ref. [11] – namely pinning and a stable balance between Laplace pressure and gas overpressure as origin of the stability of surface nanobubbles – remain unaffected by the results of the present paper.

We did explicit calculations for a van der Waals interaction although the method applied in this paper is much more general. It can be easily generalized to include different contributions that are typically associated with the disjoining pressure. The surface charges on the solid surface or on the gas-liquid interface also could be included.

References

[1] M. A. Hampton and A. V. Nguyen. Nanobubbles and the nanobubble bridging capillary force. *Adv. Coll. Int. Sci.*, 154:30–55, 2010.

[2] V. S. J. Craig. Very small bubbles at surfaces – the nanobubble puzzle. *Soft Matter*, 7:40–48, 2011.

[3] J. R. T. Seddon and D. Lohse. Nanobubbles and micropancakes: Gaseous domains on immersed substrates. *J. Phys.: Condens. Matter*, 23:133001, 2011.

[4] X. Zhang and D. Lohse. Perspectives on surface nanobubbles. *Biomicrofluidics*, 8:041301, 2014.

[5] D. Lohse and X. Zhang. Surface nanobubble and surface nanodroplets. *Rev. Mod. Phys.*, 87:981–1035, 2015.

[6] P. S. Epstein and M. S. Plesset. On the stability of gas bubbles in liquid-gas solutions. *J. Chem. Phys.*, 18:1505–1509, 1950.

[7] X. Zhang, Derek Y. C. Chan, D. Wang, and N. Maeda. Stability of Interfacial Nanobubbles. *Langmuir*, 29(4):1017–1023, 2013.

[8] J. H. Weijs and D. Lohse. Why Surface Nanobubbles Live for Hours. *Phys. Rev. Lett.*, 110:054501, 2013.

[9] Y. Liu and X. Zhang. Nanobubble stability induced by contact line pinning. *J. Chem. Phys.*, 138:014706, 2013.

[10] Y. Liu, J. Wang, X. Zhang, and W. Wang. Contact line pinning and the relationship between nanobubbles and substrates. *J. Chem. Phys.*, 140:054705, 2014.

[11] D. Lohse and X. Zhang. Pinning and gas oversaturation imply stable single surface nanobubble. *Phys. Rev. E*, 91:031003(R), 2015.

[12] S. Maheshwari, M. van der Hoef, X. Zhang, and D. Lohse. Stability of surface nanobubbles: A molecular dynamics study. *Langmuir*, 10.1021/acs.langmuir.6b00963, 2016.

[13] P. G. de Gennes. Wetting: statics and dynamics. *Rev. Mod. Phys.*, 57:827–863, 1985.

[14] L. Leger and J. F. Joanny. Liquid spreading. *Rep. Prog. Phys.*, 55:431–486, 1992.

[15] G. D. Nadkarni and S. Garoff. An Investigation of Microscopic Aspects of Contact Angle Hysteresis: Pinning of the Contact Line on a Single Defect. *Europhys. Lett.*, 20:523–528, 1992.

[16] D. Bonn, J. Eggers, J. Indekeu, J. Meunier, and E. Rolley. Wetting and spreading. *Rev. Mod. Phys.*, 81(2):739–805, 2009.

[17] J. H. Snoeijer and B. Andreotti. Moving contact lines: Scales, regimes, and dynamical transitions. *Ann. Rev. Fluid Mech.*, 45:269–292, 2013.

[18] P. G. de Gennes, F. Brochard-Wyart, and D. Quere. *Capillarity and wetting phenomena: drops, bubbles, pearls, waves.* Springer, New York, 2004.

[19] L. G. Leal B. Dai and A. Redondo. Disjoining pressure for nonuniform thin films. *Phys. Rev. E*, 78:061602, 2008.

[20] G. J. Merchant and J. B. Keller. Contact angles. *Phys. Fluids A*, 4(3):477–485, 1992.

[21] H.T. Dobbs and J.O. Indekeu. Line tension at wetting: interface displacement model beyond the gradient-squared approximation. *Physica A: Statistical Mechanics and its Applications*, 201(4):457 – 481, 1993.

[22] T. Getta and S. Dietrich. Line tension between fluid phases and a substrate. *Phys. Rev. E*, 57:655–671, 1998.

[23] L. W. Schwartz. Hysteretic effects in droplet motions on heterogeneous substrates: Direct numerical simulation. *Langmuir*, 14(12):3440–3453, 1998.

[24] J. H. Snoeijer and B. Andreotti. A microscopic view on contact angle selection. *Phys. Fluids*, 20:057101, 2008.
[25] X. H. Zhang, N. Maeda, and J. Hu. Thermodynamic stability of interfacial gaseous states. *J. Phys. Chem. B*, 112:13671–13675, 2008.
[26] S. M. Dammer and D. Lohse. Gas enrichment at liquid-wall interfaces. *Phys. Rev. Lett.*, 96:206101, 2006.
[27] C. Sendner, D. Horinek, L. Bocquet, and R. R. Netz. Interfacial water at hydrophobic and hydrophilic surfaces: Slip, viscosity, and diffusion. *Langmuir*, 25:10768–10781, 2009.
[28] N. V. Churaev. Contact angles and surface forces. *Adv. Colloid & Interface Sci.*, 58:87–118, 1995.
[29] L. D. Landau and E. M. Lifshitz. *Statistical physics, part 1.* Pergamon, 1986.
[30] M. Sellier and E. Trelluyer. Modeling the coalescence of sessile droplets. *Biomicrofluidics*, 3:022412, 2009.
[31] T. Ingebrigtsen and S. Toxvaerd. Contact angles of lennard-jones liquids and droplets on planar surfaces. *J. Phys. Chem. C*, 111:8518–8523, 2007.
[32] B. Derjaguin. Untersuchungen ueber die reibung und adhaesion, iv. *Kolloid-Zeitschrift*, 69(2):155–164, 1934.
[33] V. B. Svetovoy and G. Palasantzas. Influence of surface roughness on dispersion forces. *Adv. Colloid and Interface Sci.*, 216:1–19, 2015.
[34] A. W. Rodriguez, F. Capasso, and S. G. Johnson. The casimir effect in microstructured geometries. *Nature Photonics*, 5:211–221, 2011.
[35] C. D. Fosco, F. C. Lombardo, and F. D. Mazzitelli. Derivative-expansion approach to the interaction between close surfaces. *Phys. Rev. A*, 89:062120, 2014.
[36] J. Israelachvili. *Intermolecular and surface forces.* Academic Press, 1991.
[37] V. S. Vorobev and S. P. Malyshenko. Thermodynamics of phase equilibrium in nonuniform fields. *Phys. Rev. E*, 56:3959–3967, 1997.
[38] J. Joanny and P. de Gennes. A model for contact angle hysteresis. *J. Chem. Phys.*, 81:552, 1984.

2

3

How a surface nanodroplet sits on the rim of a microcap

The location and morphology of femtoliter nanodroplets that nucleate and grow on a microcap-decorated substrate in contact with a liquid phase was investigated. We experimentally examined four different wetting combinations of the flat area and the microcaps. The results show that depending on the relative wettability, the droplets sit either on the plain surface, or on the top of the microcap, or on the rim of the microcap. The contact angle and, for the last case, the radial positions of the nanodroplets relative to the microcap centre were characterised, in reasonable agreement with our theoretical analysis which is based on an interfacial energy mimimization argument. However, the experimental data show considerable scatter around the theoretical equilibrium curves, reflecting pinning and thus non-equilibrium effects. We also provide the theoretical phase diagram in parameter space of the contact angles, revealing under which conditions the nanodroplet will nucleate on the rim of the microcap. [1]

[1] Based on: S. Peng, I. Dević, H. Tan, D. Lohse and X. Zhang, How a surface nanodroplet sits on the rim of a microcap, *Langmuir* 32:5744-5754, 2016. Numerical work is part of the thesis

3.1 Introduction

Nucleation and growth of sessile nanodroplets on a microstructured surface is of high relevance to a wide range of fundamental and practical processes [1–4]. It is an essential step in water collection [5, 6], highly efficient cooling systems [7, 8], antifog or antifreeze [9, 10], liquid manipulation in microfludic systems [11], corrosion [12–14], among many others. Intensive research interest has been drawn to the control of droplet formation by tailoring surface microstructures [10, 15–17]. Biomimetic structures often possess exceptional wetting properties, such as the structures of lotus leaves, butterfly wings, desert beetle back, insect eyes or spider fibers [6, 18–20]. Among natural structures with amazing wetting properties, spherical bumps appear to be a commonly shared morphological feature over different length scales, for instance in lotus leaf, Namib desert beetle back or moth eyes[6, 18, 21, 22]. Therefore, manipulation of droplets on a surface will benefit from a better understanding of wetting properties of a nanodroplet on spherical microcaps. The understanding is also beneficial for advanced materials in which nanodroplets on a desired position relative to a microsphere have been used as effective templates in fabrication of particles with unconventional shapes [23–26].

Although wetting phenomenon of nanodroplets on topographically structured substrates have been theoretically studied [2, 27–30], experimentally, not so much work has been done, as it is not simple to place nanodroplets near a microstructure due to their very small volume. In contrast to the standard top-down approach by depositing the droplet from a bulk liquid, in a bottom-up approach nanodroplets nucleate and grow in-situ on the microstructure by interfacial phase transition and diffusion interaction with the surrounding phase [31]. In our recent work, we found that nanodroplets preferentially nucleate at the *rim* of polymeric microcaps sitting on a flat substrate coated with the same polymer [32]. The droplets therein were produced by solvent exchange where a good solvent for the droplet liquid was displaced by a poor solvent [33–35]. The volume of those nanodroplets was as small as a few attoliters to femtoliters, depending on flow conditions and solution compositions [32]. An optical snapshot of various of these nanodroplets sitting around microcaps and on the plane surface is shown in Figure 3.1 a. Figure 3.1 b shows the three-dimensional fit of an AFM image (details will be provided later) of three nanodroplets sitting around a microcap. An example for a single droplet sitting on the rim of a microcap is shown in Figures 3.2 a (AFM image) and b (SEM image), taken from ref. [32]. In that work we also found spontaneous pattern formation of *multiple* surface nanodroplets simultaneously growing on the rim. The (relative) *azimuthal* position of these nanodroplets on the rim of the microcap has been discussed in detail in ref. [32]. In this work, we will

focus on their *radial* positions and on their contact angles. In order to better understand the wetting properties of nanodroplets on microcaps, we will cover four different macroscopic wetting conditions for the droplet liquid where the chemical composition and morphology of the microcaps were varied.

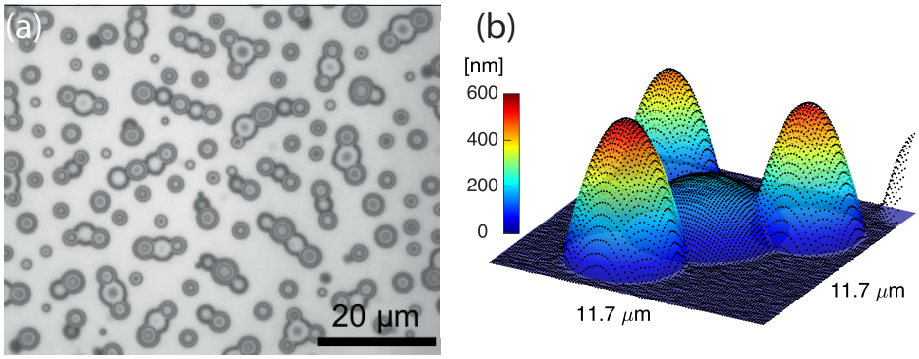

Figure 3.1: a) Optical microscopy image of nanodroplets sitting on the rim of microcaps or on the plane substrate. b) Three-dimensional fit of an AFM image of three nanodroplets sitting on the rim of a microcap.

Figures 3.2 c and d give sketches of the sideview and the topview of the nanodroplet sitting on the rim and the notations used in this paper. L is the contact diameter of the microcap, H its height, and α its contact angle. Correspondingly, ℓ is the contact diameter of the nanodroplet sitting on the rim and h its height. The contact angle of the nanodroplet on the microcap is defined as θ_{mc}, whereas the contact angles on the flat surface is θ_{fs}. Finally, $\ell_0/2$ the distance between the centers of (spherical) contact areas of the microcap and the nanodroplet and $\ell_p/2$ the distance between the center of the microcap and the projection of the contact point between microcap and nanodroplet, which is closest to the apex of the microcap, down onto the plane of the substrate.

The microcap's morphology is characterised by L and α, and the nanodroplet's by ℓ and θ_{fs} (or alternatively its volume). We will use these as control parameters and then experimentally and theoretically determine ℓ_0 and ℓ_p, i.e., determine how far the nanodroplet will creep over the microcap. The experimental results are in reasonable agreement with a theoretical analysis of the droplet morphology that is based on a minimization of the interfacial energy of the system. However, there is quite some scatter of the experimental data which we ascribe to the central role of pinning at the droplet boundaries and thus to non-equilibrium effects. Note that we will restrict ourselves to cases in which the apex of the nanodroplets at the rim was controlled to be above 100 nm, so that a large portion of the droplets is beyond the range of intermolecular interactions.

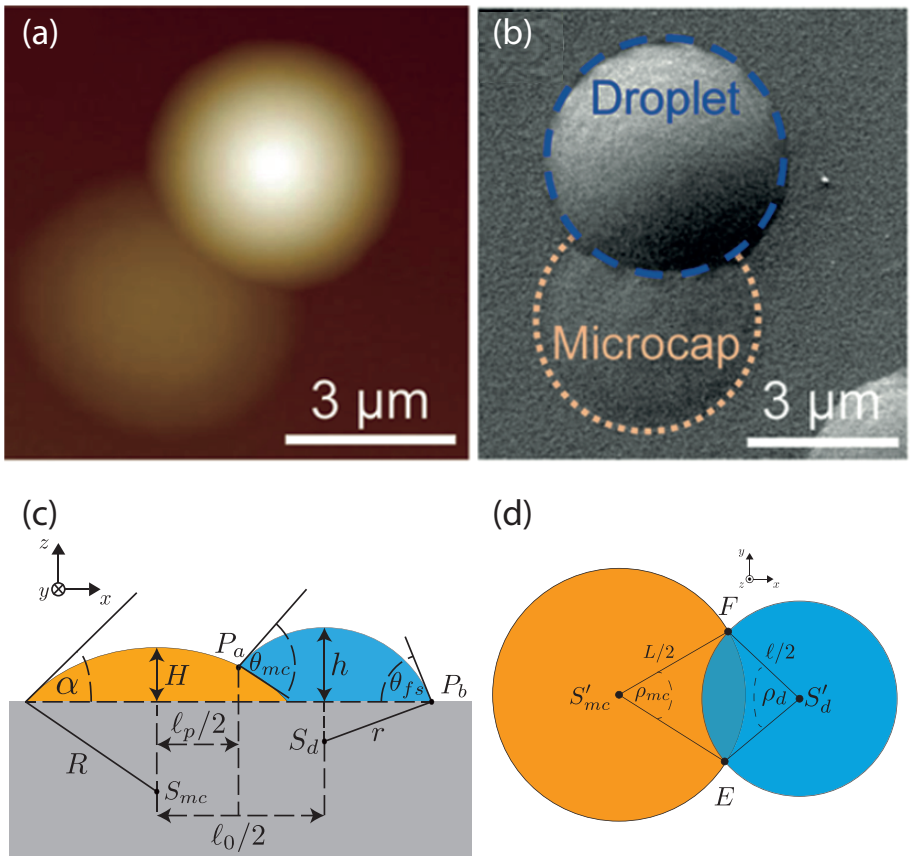

Figure 3.2: (a, b): AFM and SEM images of one nanodroplet sitting on a microcap. Taken from ref. [32]. (c, d): Sketch of the geometry of the nanodroplet-microcap system and axis orientations as seen from the sideview c) and the top view d). The sketches also give the notation used in the paper.

3.2 Experimental section

Chemicals and materials

One side polished silicon wafers were purchased from UniversityWafer, Inc. (South Boston, MA). Octadecyltrimethylchlorosilane (OTS, >90%), crosslinker (1,6-hexanediol diacrylate, HDDA), monomer (2-(dimethylamino)ethyl methacrylate, DMAEMA), and photoinitiator (2-hydroxy-2-methylpropiophenone) were from Sigma. Organic solvents like chloroform (AnalaR), toluene (AnalaR), and ethanol (100%) were from Merck Pty Ltd. All chemicals were used without further purification unless otherwise specified.

Preparation of hydrophobic OTS-Silicon (OTS-Si) substrates

In the preparation of OTS-Si substrates, polished silicon wafers were cleaned in piranha solution ($H_2SO_4(70\%) : H_2O_2(30\%)$) at 75^{o}C for 20 min. All

glassware used for the solution was dried for 2 h under 120^{o}C in an oven. The silicon was dried at 120^{o}C for 1.5 h and soaked in 0.5 vol % OTS in toluene for about 2 h in a sealed dry container at room temperature. After 12 h, the OTS-Si substrates were rinsed with chloroform, sonicated in toluene and ethanol, dried with nitrogen, and then stored in a clean container. Before use, the OTS-Si was cleaned in ethanol and water by using an ultrasound bath.

Preparation of patterned surfaces

Patterned surfaces with hydrophobic circular domains on hydrophilic background were prepared by photolithography method [36]. Briefly, photoresist was spun coated on precleaned silicon substrates and subsequently exposed to UV light through a photomask. After rinsing the substrates in developer solution and DI water, the unprotected circular domains were exposed and chemically modified by OTS, resulting in circular hydrophobic domains with diameters ranging from 3 to 10 μm. The hydrophilic background was then exposed by removal of the top photoresist coating. The average roughness of the OTS-coated microdomains is about 2 nm and the water contact angles in air on the hydrophilic and hydrophobic domains were found to be 10^o and 118^o, respectively..

Formation and characterization of microcaps and nanodroplets

The detailed procedure for the preparation of polymeric microcaps by solvent exchange method was descripted in our previous work [32, 34, 37]. Precursor polymerizable monomer nanodroplets were generated on hydrophobic OTS-Si substrates by the solvent exchange method. The polymeric microcaps were obtained after the photopolymerization. On the prepatterned substrate, the droplets formed selectively on the circular microdomains [36]. After the polymerisation, those microcaps in the regular array were used as the substrate for the nanodroplet formation. The nanodroplets were also produced by the solvent exchange using solutions corresponding to the droplet liquid. The droplets were also photopolymerized before the characterisation.

The microcaps and polymerized nanodroplets were examined by optical microscope, scanning electron microscope (SEM) (FEI Nova, NanoSEM, Oxford X-MaxN 20 EDXS), and atomic force microscope (AFM) (MFP-3D, Asylum Research, Santa Barbara, CA). The geometrical properties and in particular the cross-sectional profiles of the nanodroplets and microcaps were extracted from AFM images by 3D spherical-cap fitting. Here cut-off distances of either 10 nm or of 20 nm were introduced near the foot of the microcaps and the nanodroplets, to eliminate disjoining pressure effects, but the results were

found to be independent of the exact value of the cut-off. The detailed fitting methodology will be reported in another manuscript in preparation.

3.3 Experimental results

We studied the position and morphological features of the nanodroplets around the microcaps for four different cases summarised in Table 3.1. The microcap-decorated substrate in case 1 is shown in Figure 3.3 a-d. The footprint diameters of the microcaps ranged from 4 to 8 μm, and their heights from 50 to 300 nm, while the contact angle was around $7^\circ - 8^\circ$ for all microcap sizes. In case 2 the contact angle of all microcaps was also around 8^o as shown in Figure 3.3 e-h, while the footprint diameters of the microcaps varied from 4 to 8 μm, and their heights from 100 nm to 1 μm. The substrate and the droplet liquid for case 3 were chemically the same as for case 2, but the microcap contact angle was much larger, namely about $\alpha \approx 50^o$ rather than 8^o as in case 2, see Table 3.1. In case 4 the microcaps sat on a hydrophilic substrate with a lateral diameter of 10 μm and a height of 750 nm. After the completion of the solvent exchange on the above substrates, nanodroplets were polymerised before the morphological characterisation.

	Microcap	Droplet liquid	Mean α	Mean θ_{fs}
Case 1	PHDODA	HDODA	$\approx 8^\circ$	$\approx 26^\circ$
Case 2	PDMAEMA	DMAEMA	$\approx 8\circ$	$\approx 45\circ$
Case 3	PDMAEMA	DMAEMA	$\approx 50\circ$	$\approx 45\circ$
Case 4	PHDODA	HDODA	$\approx$17	N/A

Table 3.1: Employed liquids for the microcap and droplet formation and resulting contact angles for the four analysed cases.

3.3.1 Case 1

The optical image in Figure 3.1 a shows the polymerised nanodroplets and the microcaps on the substrate. Nanodroplets formed on the rim of the microcaps as well as on the flat area. The former are referred to as 'droplets on rim', and the latter as ' isolated droplets'. There are also some pearl necklace-like structures made of several alternating microcaps and closely spaced polymerised droplets. Regular Newton rings observed on both microcaps and nanodroplets were denser on the later than on the former, suggesting that the aspect ratio of microcaps is smaller than that of polymerised droplets [37].

Based on the spherical cap fittings of the nanodroplets in AFM images, we obtained its essential features: the contact angles on both the microcap surface

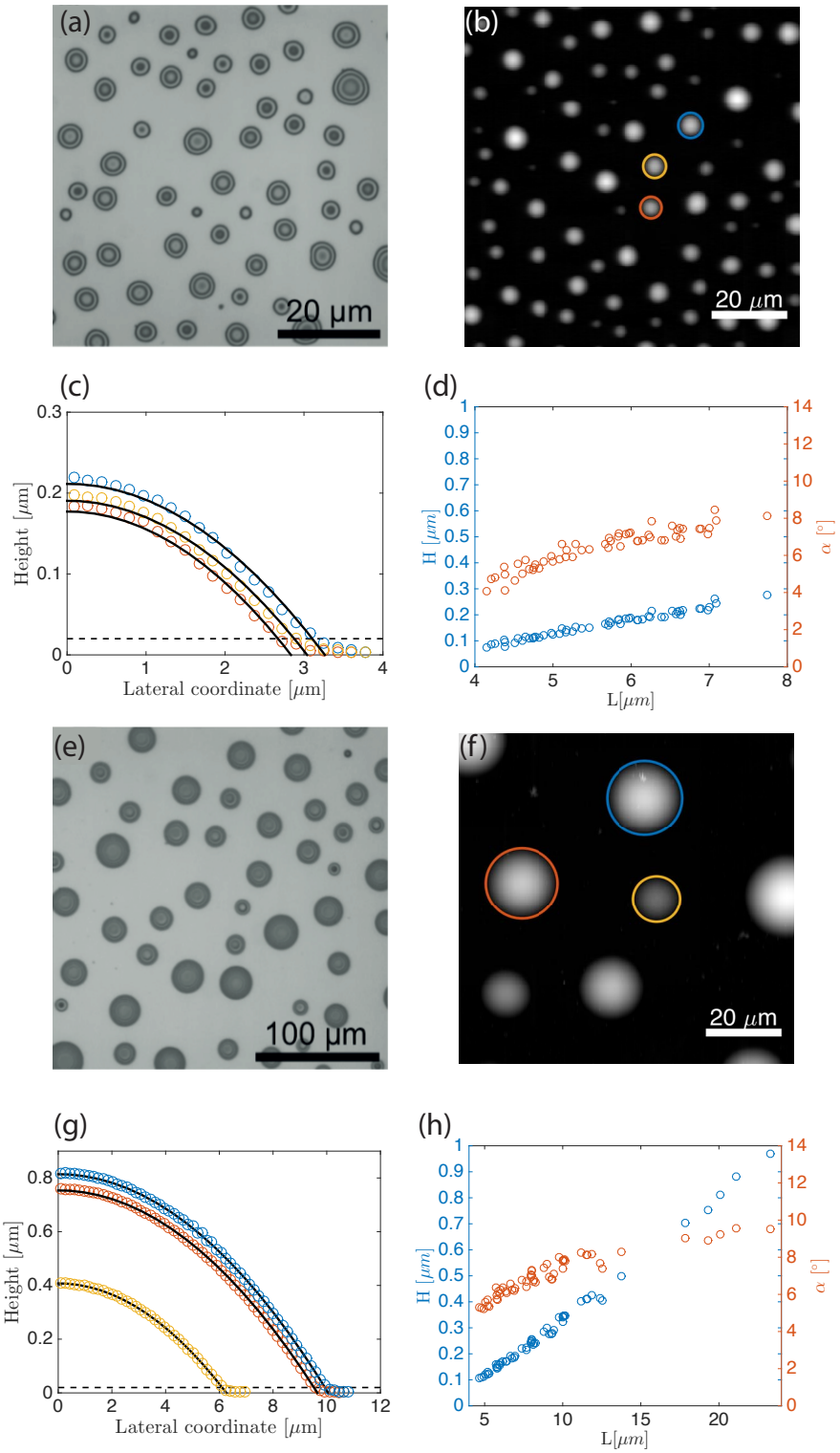

Figure 3.3: Properties of the microcaps in cases 1 and 2. Substrate in case 1 (a-d): In a) and b), optical microscopy and AFM images of PHDODA microcaps are shown; c) shows the cross-section profiles of three microcaps indicated in b). The circles show our cross section analysis from AFM data and the solid lines are corresponding spherical-cap fitting; In d), the height and the contact angle are plotted as function of lateral size of the PHDODA microcaps. The later plot reveals the sharp distribution of the contact angle; (e-h) are the corresponding characterizations of PDMAEMA microcaps in case 2.

and on the flat area, θ_{mc} and θ_{fs}, respectively, the footprint diameter ℓ, the height, and the relative position of the droplet centre to the microcap center, expressed by ℓ_p and ℓ_0. In Figure 3.4 c and e, we compare the results of our spherical cap fittings and cross section analysis of both 'isolated' nanodroplets and 'nanodroplets on rim'.

The plots in Figures 3.4 f and g show that the height of the isolated nanodroplets and the nanodroplets at the rim increases nearly linearly with the footprint diameter. The contact angles of the nanodroplets on the rim formed with the flat area and with the microcap and the ones of the isolated nanodroplets were all approximately 26^o, independent of the nanodroplet size. The length scales ℓ_0 and ℓ_p, which characterise how much the nanodroplet has creeped over the microcap, are given in Figures 3.4 h and i. These data are rather scattered – we will argue below that this is due to pinning effects – but we can extract that the larger the relative size of the nanodroplet with respect to the microcap, the larger is the distance between the droplet and microcap base centre, and the less it creeps on the microcap, compared to the nanodroplets length scale (contact diameter ℓ).

3.3.2 Case 2

For case 2 we observed a drastically different behavior of the nanodroplets. Both optical and AFM images (Figures 3.5 a and b) shows that the nanodroplets are scattered over the entire surface. Some nanodroplets sit on the top of microcaps while others are on flat area. There was no preference to the rim of the microcaps. In the contrary, it seemed that the nanodroplets somehow avoided the rim, as evidenced by the absence of nanodroplets sitting next to the microcap. While the morphological features of the microcaps were similar in cases 1 and 2, the contact angle of the droplets on the flat area in case 2 was $35 - 50^o$ as measured from the AFM images, which is larger than the contact angle in case 1 (26^o). The different locations of the nanodroplets in case 1 clearly reveal that, for the same (flat) morphologic features of the microcaps, the nanodroplets will preferentially nucleate at the microcap rim if the droplet liquid can wet the substrate well. The different contact angle θ_{fs} of the nanodroplets on the surface thus disfavours or even prevents their nucleation at the rim of the microcaps, for which we will provide energy argument in the theoretical analysis of the system.

3.3.3 Case 3

Now we look into case 3, in which the polymerised droplets of case 2 acted as the microcaps on the substrates. The contact angle of the microcaps was

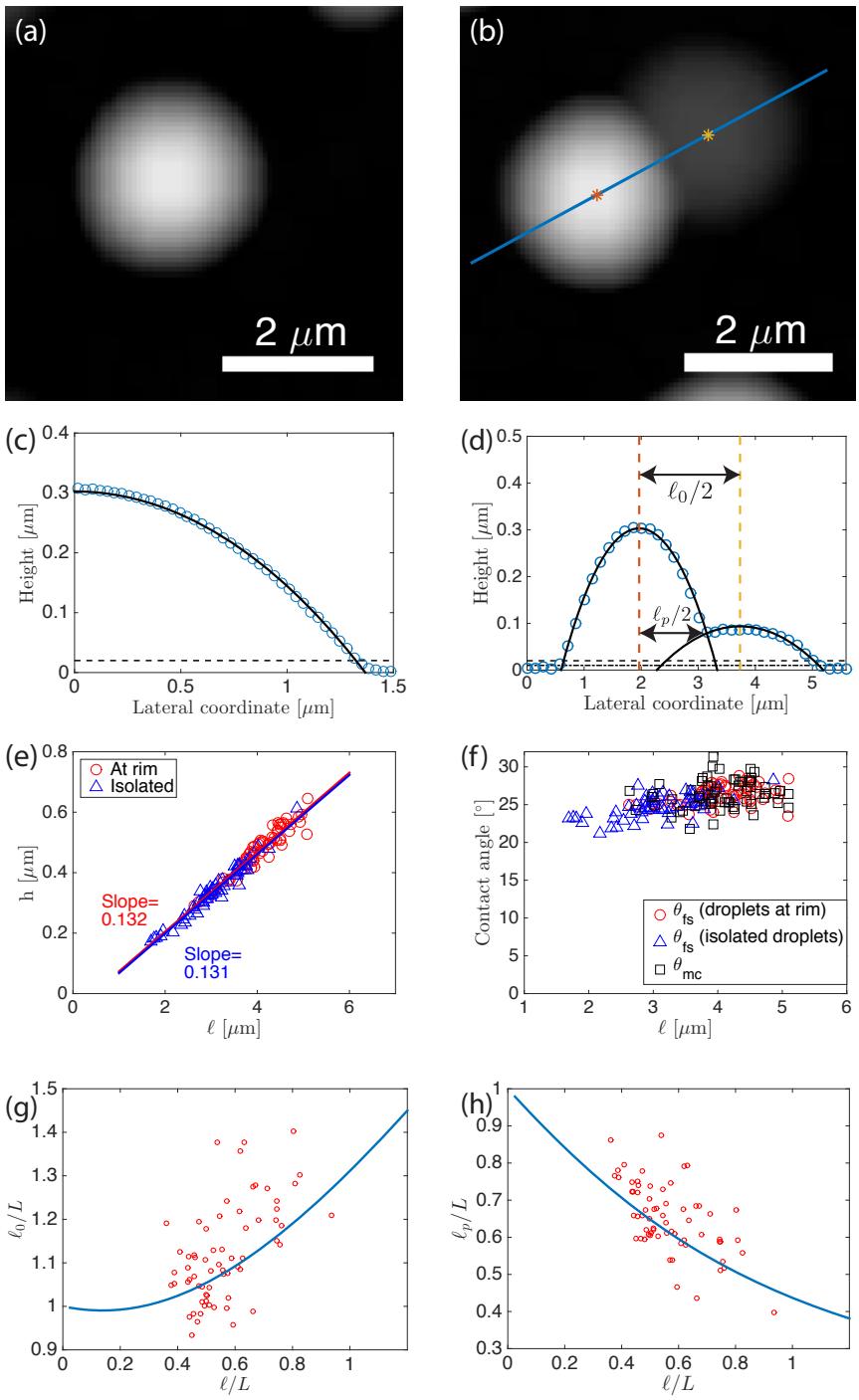

Figure 3.4: Case 1: a) and b) AFM images of an isolated nanodroplet and a nanodroplet sitting on the rim; c) and d) are their corresponding cross-section profiles; The height e) and the contact angle θ_{fs} f) are plotted as function of the lateral size of the isolated nanodroplet and of the nanodroplets on the rim; g) and h) Experimental data for ℓ_0/L as function of ℓ/L (red circles) in comparison with our theoretical result (blue curve, $\theta_{fs} = \theta_{mc} \approx 26^o$, $\alpha \approx 8^o$).

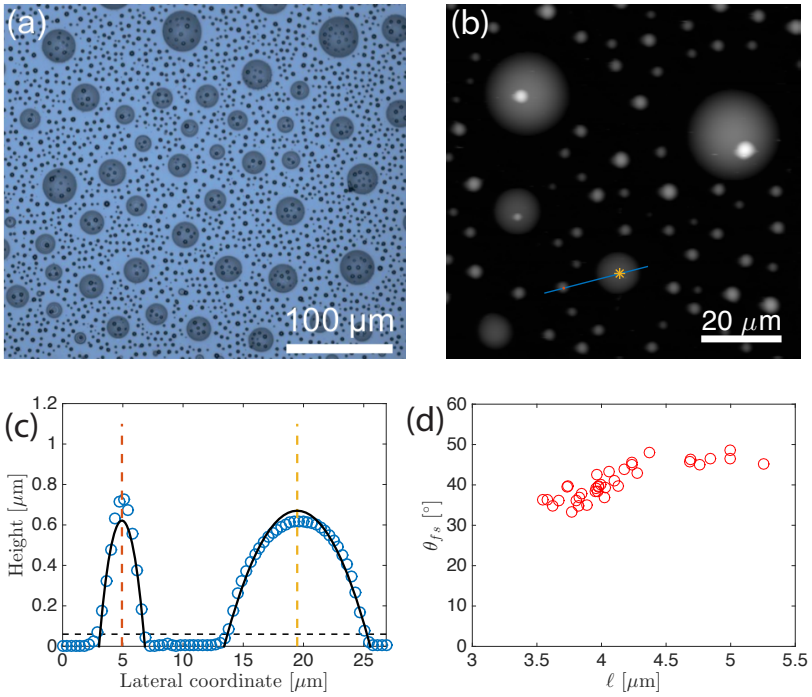

Figure 3.5: Case 2: DMAEMA nanodroplets on surface decorated with PDMAEMA microcaps: Optical a) and AFM b) images of DMAEMA nanodroplets sitting on the top of the PDMAEMA microcaps and on the flat surface. In c) the corresponding cross-section profile of an isolated nanodroplet and a close-by microcap is shown; In d) the contact angle θ_{fs} is plotted as function of the lateral size of the isolated nanodroplet.

$40° - 60°$, much higher than for the microcaps in case 2, while the droplet liquid was the same as in case 2. This time we again found (as in case 1) that the nanodroplets preferentially sit on the rim of the microcap. In fact, all microcaps are accompanied by one or more nanodroplets as shown in Figure 3.6. [2] Clearly, in case 3 the rim of the microcaps is preferred for the nanodroplet nucleation.

The cross-sectional profile of the nanodroplet-microcap composites in Figure 3.6 d show a part of the spherical-cap-shape of both the microcap and the nanodroplet. Interestingly, there is large difference in the contact angles of the nanodroplet on the side with flat surface (θ_{fs}) and with the microcap (θ_{mc}). The former is 35^o to 55^o, which is the same as the contact angle of the isolated nanodroplets, but the later surprisingly is larger, varying from 50^0 to 70^0. The length scales ℓ_0 and ℓ_p are given in Figures 3.6 h and i, showing a similar trend as in case 1, but now with much less scatter. The result clearly suggests that the morphology of the microcap (i.e., its contact angle α) has significant influence on the positioning and morphology of the nanodroplets

[2] We can distinguish our nanodroplets from microcaps by doping the droplet liquid with a fluorescent dye. Our fluorescent images revealed that those individual structures were fluorescent. So they are not lonely microcaps, but isolated nanodroplets.

around them.

3.3.4 Case 4

Finally, we analysed case 4 which is different from the above three cases in terms of the wettability of the flat area. The microcaps in case 4 consisted of the same material as in case 1, but the flat area was lyophobic. After the solvent exchange, all of the nanodroplets were exclusively located on the top of the microcaps. Examples are shown in Figure 3.7. Part of the nanodroplet rim overlapped with the microcap rim, suggesting that the nanodroplet nucleated from the microcap rim and grew over the top surface of the microcap.

3.4 Theoretical analysis

3.4.1 Procedure

What physical principle does the morphology and position of the nanodroplet determine? One may be tempted to immediately answer that it would be the principle of minimal surface energy together with Young's equations [38] (which in fact *reflects* the minimal energy condition) for the equilibrium contact angles – and indeed we will later perform a corresponding calculation. However, before we do so, we would like to caution the reader: During the growth process of the nanodroplets due to solute oversaturation the system strictly speaking is *not* in equilibrium. In fact, for (temporarily) oversaturated systems (leading to a growth of the nanodroplets) the resulting contact angles depend on length and strength of the oversaturation pulse and the pinning features of the droplet on the surface and thus on the chemical and geometrical surface inhomogeneities [4, 35, 36]. In fact, in ref. [36], thanks to different oversaturation pulses and given pinning sites, nanodroplets with *different* contact angles are produced, though they consist of the identical liquid and sit on the identical surface. Obviously, in that case Young's equation is irrelevant.

Here we will first assume that pinning effects will *not* play a major role and that the contact angles of the nanodroplets are given by Young's equation. To be more precises, there are two Young angles, namely the one for the nanodroplet on the flat substrate

$$\cos\theta_{fs} = \frac{\gamma_{s\ell_0} - \gamma_{s\ell}}{\gamma_{\ell_o\ell}} \tag{3.1}$$

and the one for the contact of the nanodroplet on the microcap,

$$\cos\theta_{mc} = \frac{\gamma_{S\ell_0} - \gamma_{S\ell}}{\gamma_{\ell_o\ell}}. \tag{3.2}$$

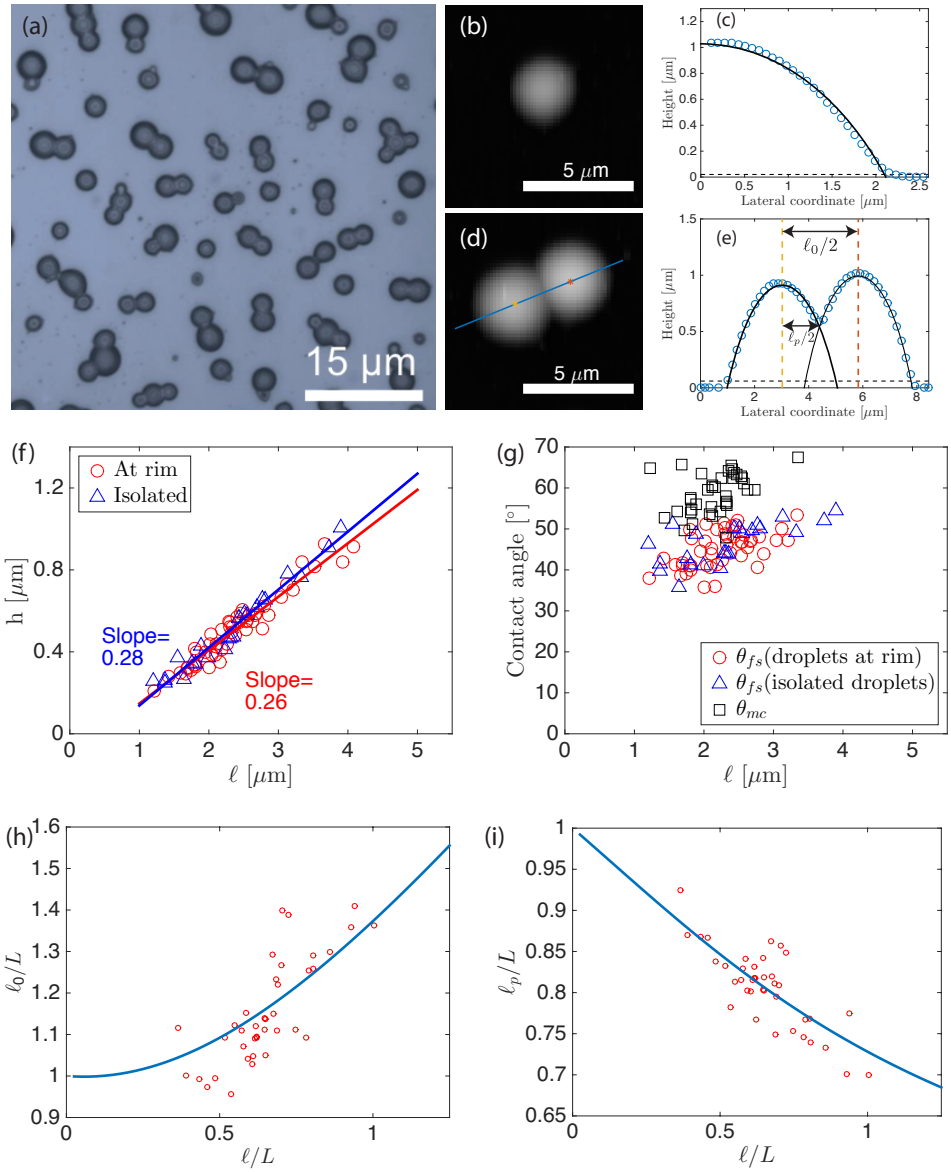

Figure 3.6: Case 3: DMAEMA nanodroplets sitting on the rim of PDMAEMA microcaps: a) Optical microscopy image of DMAEMA nanodroplets on the PDMAEMA microcaps; b) AFM images of the isolated nanodroplets and the nanodroplets sitting on the rim of the microcap; In c) and d) their corresponding cross-section profiles are given; In e) and f), the height and the contact angle are plotted as function of the lateral size of the isolated nanodroplets and the nanodroplets on the rim; (h,i) Experimental data for ℓ_0/L as function of ℓ/L (red circles) in comparison with our theoretical result (blue curve, $\theta_{fs} \approx 43^0$, $\theta_{mc} \approx 60^0$ and $\alpha \approx 50^o$).

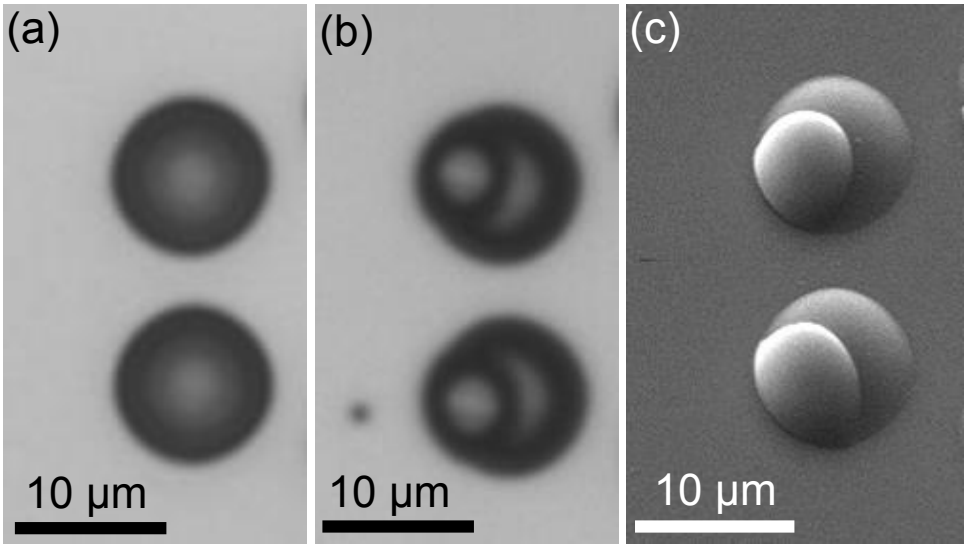

Figure 3.7: Case 4: The nanodroplets are exclusively sitting on the top of the microcaps, as the background surface is hydrophilic: Optical microscopy images of microcaps before a) and after b) nanodroplet formation; c) shows a SEM image of nanodroplets sitting on the top of microcaps.

Here γ_{ij} is the surface tension between the i and j phases and s denotes the solid phase of the flat substrate, S the solid phase of the microcap, ℓ the liquid phase of the nanodroplet and ℓ_o the liquid phase outside of the nanodroplet (outer phase), see Figures 3.2 c and d.

From the direct AFM measurements we know that the microcap is spherical-cap-shaped (orange colour in Figures 3.2 c and d). The same holds for the nanodroplets (blue colour). The reason is that gravitational effects are negligible (i.e.., small Bond number) and no other forces apart from capillarity play any role. Therefore in our calculation we can assume that the microcap and the nanodroplet are (part of) a spherical-cap, i.e., are locally sphere-like, which follows from surface energy minimisation, once the energy is dominated by capillarity.

The nanodroplet sits on the spherical-cap-shaped microcap with given footprint diameter L and contact angle α (and thus also given radius of curvature R). As control parameters of the problem we take the given nanodroplet volume, and – according to table 3.1 – the given nanodroplet contact angle θ_{fs} on a flat surface (resulting in some footprint diameter ℓ and some radius of curvature r), and the given nanodroplet contact angle θ_{mc} on the microcap[3]. We will then calculate the radial position of the nanodroplet on the microcap.

To describe this radial position of the nanodroplets on the microcap, we define all geometric parameters as shown in Figures 3.2 c and d. In particular,

[3]Note that θ_{mc} does not vary along the contact line between nanodroplet and microcap, due to the assumed nested spherical cap shapes.

$\ell_p/2$ is the distance between the orthogonal projections (on the plane of the flat substrate) of S_{mc} (S'_{mc}), which is the center of curvature of the footprint area for the microcap, and P_a, which is the contact point of the nanodroplet and the microcap closest to the apex of the microcap. Further, $\ell_0/2$ is the distance between the orthogonal projections of the centres of curvatures on the plane of the flat substrate.

The length scales ℓ_p and ℓ_0 fully characterise the radial position of the nanodroplet on the microcap. Given Young's laws (3.1) and (3.2) and the requested locally spherical shape of the nanodroplet, which both reflect the minimal energy condition, for given contact angles θ_{fs} and θ_{mc} and given nanodroplet volume, they follow from a straightforward numerical calculation.

Before we will discuss the results, we would like to point out that, alternatively to this approach, one can also directly calculate the interfacial energy and minimise it under constraints, which will lead to exactly the same results. The interfacial energy of the nanodroplet sitting on the microcap is given by

$$E = A_1(\gamma_{s\ell} - \gamma_{s\ell_0}) + A_2\gamma_{\ell_o\ell} + A_3(\gamma_{S\ell} - \gamma_{S\ell_0}), \tag{3.3}$$

with A_k representing the contact surface of the nanodroplet with the other phases depending on the value of the index k (1 for flat substrate, 2 for outer phase, 3 for microcap). We normalise Eq. (7.10) with $\gamma_{\ell_o\ell}$ and use Eqs. (3.1)-(3.2) to obtain

$$\tilde{E} \equiv \frac{E}{\gamma_{\ell_o\ell}} = -A_1\cos\theta_{fs} + A_2 - A_3\cos\theta_{mc}. \tag{3.4}$$

In case 1 and 2 where the microcap and the flat substrate are of the same material ($\theta_{fs} = \theta_{mc} \equiv \theta$), Eq. (3.4) reduces to

$$\tilde{E} = A_2 - (A_1 + A_3)\cos\theta. \tag{3.5}$$

We then calculate the contact areas A_1, A_2, and A_3 in Eq. (3.4) for this nested spherical-cap geometry. The expressions for these contact areas of the nanodroplet are derived in the Appendix. They read

$$A_1 = (r\sin\theta_{fs})^2\pi - \frac{(R\sin\alpha)^2}{2}(\rho_{mc} - \sin\rho_{mc}) - \frac{(r\sin\theta_{fs})^2}{2}(\rho_d - \sin\rho_d), \tag{3.6}$$

$$A_2 = 2r^2\pi(1-\cos\theta_{fs}) - r^2\int_{\theta_A}^{\theta_{fs}} \rho_{\mathrm{d}}(\theta)\sin\theta\,\mathrm{d}\theta \tag{3.7}$$

and

$$A_3 = R^2\int_{\theta_A}^{\alpha} \rho_{\mathrm{mc}}(\theta)\sin\theta\,\mathrm{d}\theta. \tag{3.8}$$

Here ρ_{mc} and ρ_d are defined as the angles at which we see line segment $\bar{EF}$ from S'_{mc} and S'_d, respectively, see Figure 3.2 d. The corresponding volume of the nanodroplet (which is imposed as constraint) is calculated by numerical integration of the volume integral.

To minimise the interfacial energy Eq. (3.4) for a given value of the volume, we now proceed as follows: We construct a family of spherical cap solutions satisfying Young's equation (Eq. (3.1)) in the point P_b [39, 40] and at the same time the volume constraint. In order to search for the dependance of Eq. (3.4) as function of the position of point P_a, we then determine which position of the point P_a minimises Eq. (3.4), which also defines the value of the contact angle of the nanodroplet at point P_a. The latter is indeed the Young angle θ_{mc} (Eq. (3.2)) as required and from the position of P_a we calculate the radial length scales ℓ_0 and ℓ_p.

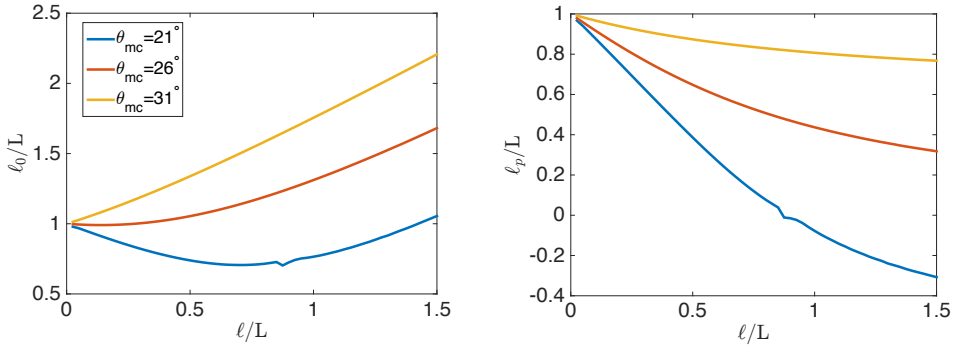

Figure 3.8: Theoretical results for the distance length scale ℓ_0/L and the position length scale ℓ_p/L as function of the microdroplet size ℓ/L, obtained from minimising Eq. (3.4) for three different relative wettabilities θ_{mc} (namely 26^0, 21^0, and 31^o) of the spherical-cap shaped microcap. For all calculations we set $\theta_{fs} = 26^o$ and $\alpha = 8^o$.

Results of theoretical analysis

The resulting radial length scales ℓ_0 and ℓ_p – consistently obtained with either of the above sketched methods – are shown in Figure 3.8, for three scenarios, namely for one in which both the flat substrate and the microcap are made of the same material (same Young angle), one for which the microcap is more lyophobic (larger Young angle), and one for which the flat substrate is more lyophobic. We see that all three scenarios have a common property: As expected, the nanodroplets asymptotically approach the rim of the microcap as the volume of the nanodroplet approaches zero. For the case of the microcap being more lyophilic than the flat substrate ($\theta_{mc} < \theta_{fs}$, blue curve), we notice that nanodroplets will tend to cover even the apex of the microcap (i.e., $\ell_p < 0$) if the volume is large enough. Note the little kink in the curve which occurs at

$\ell_p \approx 0$ (i.e., only for preferred wetting of the microcap as compared to the flat surface $\theta_{mc} < \theta_{fs}$ and at the same time very large nanodroplet volumes and correspondingly negative ℓ_p), reflecting that in the calculation the position of the point P_a can never be exactly on the apex of the microcap.

Next, we compare the results from our energy minimisation procedure with the experimental results for cases 1 and 3, in which the nanodroplets are sitting on the rim of the microcap. For the contact angles α and θ_{fs} we take the respective values from Table 3.1. The contact angle θ_{mc} on the microcap side is obtained from our 3-D spherical fitting of the AFM data (we take the average value). In case 1 it is roughly the same as θ_{fs} (see Figure 3.4f), whereas in case 3 θ_{mc} is about 20^o larger than θ_{fs}, see Figure 3.6 g, presumably due to contact line hysteresis and pinning. We then calculate ℓ_0 and ℓ_p, which are shown in Figures 3.4 g, h and 3.6 h, i together with the respective experimental data.

In general, we find reasonable agreement with the experimental data, giving support to our simple macroscopic energy minimisation approach and the assumption of the validity of the Young laws. However, the experimental data show quite some scatter around the theoretical equilibrium curves, presumably reflecting pinning effects and the violation of the equilibrium condition.

From the Figure 3.4 h and Figure 3.6 i we see that pinning to physical or chemical heterogeneities causes nanodroplets of the same footprint diameter to have quite some deviations in the values of ℓ_p. As already mentioned above, it is this pinning which leads to the scatter of our experimental data around the theoretical predictions, along with the individuality of the microcaps and the nanodroplets (variations in values of α and contact angles), which cannot be avoided by the solvent exchange method in experiments [41]. Since our theoretical predictions are functions only of the contact angles α, θ_{fs} and θ_{mc} (Eq.(3.4)), we calculated them with the average values of the contact angles in our experiments and there is no way to normalise our data with the individual Young angles to collapse them on one line.

To better understand our theoretical results, we show, in Figure 3.9 a and b), interfacial energy values of the nanodroplet satisfying a volume constraint ($V = 28.41\mu m^3$) and the Young's angle in point P_b ($\theta_{fs} = 26°$) as a functionf of the position ℓ_0 of the center of the nanodroplet. We set θ_{mc} to be 21° in a and 31° in b). We also plot the interfacial energy values of the nanodroplet of the same volume, in cases where the nanodroplet completely wets either the flat substrate or the microcap, provided that these wetting states can occur with the corresponding Young angle as contact angle of the nanodroplet. The global energy minimum, for different values of α, is located either on the rim of the microcap or on the more lyophilic surrounding of the rim of the microcap, depending on the values of the Young angles θ_{fs} and θ_{mc}. In Figure 3.9 d, we

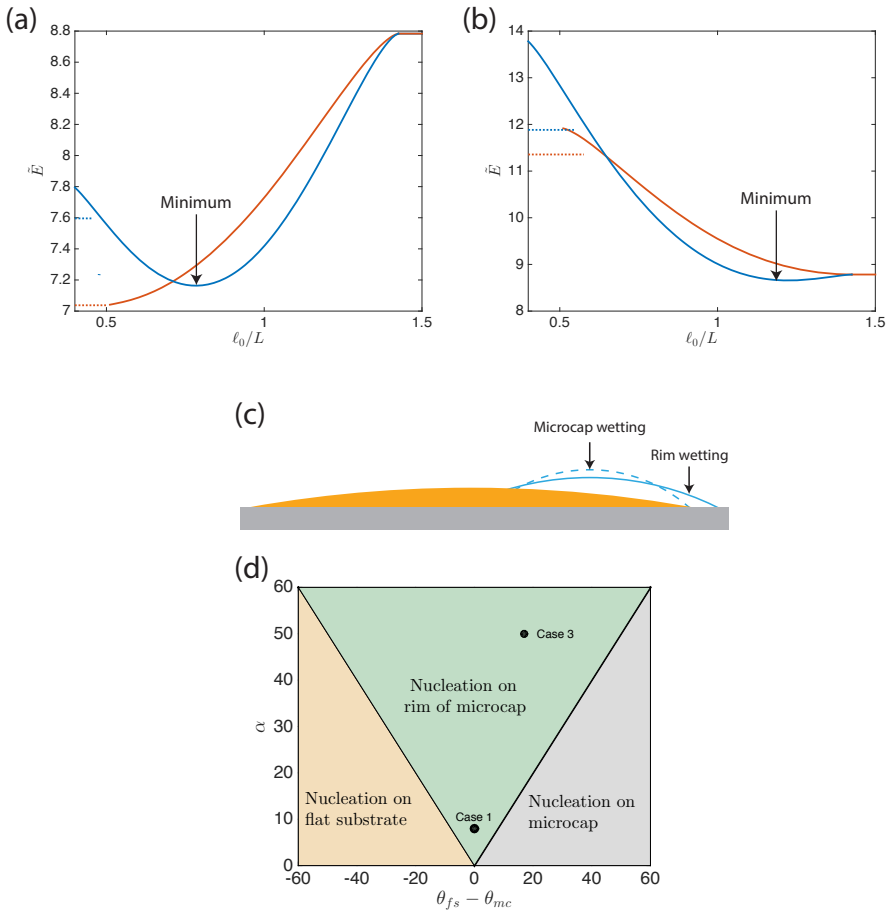

Figure 3.9: a) Interfacial energy as a function of the ratio ℓ_0/L for nanodroplets with constant volume and Young's angle ($\theta_{fs} = 26^\circ$) in point P_b and Young's angle $\theta_{mc} = 21^\circ$. The values of α are 4° (red line) and 10° (blue line). If the nanodroplet is either completely wetting the flat substrate (right hand side of plot) or the microcap (left hand side of plot, dashed line), the values of the interfacial energy are constant . In b) we change the value of θ_{mc} to 31°, while all other parameters are kept the same. With dashed lines we show the values of the interfacial energy of the nanodroplet which is completely wetting the microcap. Since for the same value of ℓ_0/L, we can construct both the spherical cap shape satisfying our before mentioned conditions (volume, θ_{fs} in point P_b) and the spherical cap shape which is completely wetting the microcap, with the contact angles on both sides being θ_{mc}, there are two distinctive energy lines. In c) we show a sketch of these two spherical cap shapes ($\theta_{fs} = 26^\circ$, $\theta_{mc} = 31^\circ$, $\alpha = 10^\circ$ and $\ell_0/L = 0.5$; blue line from b)). All the calculations were done with the value of the footprint diameter of the microcap set to $10\mu m^3$ (L). In d we show the phase diagram in the ($\theta_{fs} - \theta_{mc}$) versus α space, revealing which configuration has the global minimum of the interfacial energy. Cases 1 and 3 are in the domain in which the nanodroplets nucleate on the rim of the microcap.

show the phase space of the nanodroplet-microcap system, where the wetting configuration with the global minimum of the interfacial energy is indicated. The nanodroplet will nucleate on the rim of the microcap only if the contact angle α of the microcap is larger than the absolute difference of Young's angles θ_{mc} and θ_{fs}

$$\alpha > |\theta_{fs} - \theta_{mc}| \tag{3.9}$$

In cases for which this condition is broken, from the energy minimisation approach we find that there is no local energy minimum for the nanodroplet, which is wetting the rim of the microcap, but a global energy minimum in one of the two asymptotic cases, namely either the nanodroplet completely wetting the flat substrate or the microcap. In the phase diagram, we see that for cases 1 and 3, where nanodroplets nucleated on the rim, the contact angle condition is satisfied (Eq. (3.9)), while for cases 2 and 4, where there was no nucleation on the rim, we could not measure either the contact angle θ_{fs} (case 4, no nucleation on flat substrate) or the contact angle θ_{mc} (case 2, scarce data of nanodroplets nucleating on the microcap).

3.5 Conclusions

The findings in this study provide insight into the nanodroplet nucleation mechanism and their morphology on microstructured surface, and give guidelines for the design and engineering of microstructures for controlled droplet position. We have experimentally and theoretically investigated the shapes and locations of nanodroplets sitting on the rim of microcaps. Their locations are determined by the interfacial tensions and the resulting contact angles, as well as the volume of the nanodroplet. The positions of the nanodroplet observed in the experiments roughly follow the trend of the theoretical predictions, which are based on an equilibrium assumption. However, we also find major scattering of the experimental data around the theoretical equilibrium curve. The origin of this scattering is presumably pinning, leading to non-equlibrium effects and hysteresis. For equilibrium cases, we also provide the phase diagram, which shows us under which conditions the nucleation of the nanodroplets will be positioned on the rim of the microcap.

3.6 Appendix: Calculation of the interfacial areas and the nanodroplet volume

Referring to the top view of the system represented in Figure 3.2 d, we subtract the intersection area of the microcap and the nanodroplet footprint area, from the footprint area of the nanodroplet and obtain

$$A_1 = (r\sin\theta_{fs})^2\pi - \frac{(R\sin\alpha)^2}{2}(\rho_{mc} - \sin\rho_{mc}) - \frac{(r\sin\theta_{fs})^2}{2}(\rho_d - \sin\rho_d). \quad (3.10)$$

In order to calculate A_3, let us define the spherical coordinate system ($r = \sqrt{x^2+y^2+z^2}$, $\theta = \arccos\frac{z}{\sqrt{x^2+y^2+z^2}}$, $\phi = \arctan\frac{y}{x}$) with the origin of the coordinate system located in S_{mc}. In Figure 3.2 c we represent the geometry of our system on a flat substrate. If we performed a horizontal cross-section of the nanodroplet-microcap system above the flat substrate, we would obtain the same geometrical scheme with L, l, ρ_{mc} and ρ_d being the functions of θ. If we denote polar angle (θ) of point P_a with θ_A, we can write A_3 as a result of the surface integration in the spherical coordinate system,

$$A_3 = R^2\int_{\theta_A}^{\alpha}\rho_{\mathrm{mc}}(\theta)\sin\theta\,\mathrm{d}\theta. \quad (3.11)$$

To calculate $\rho_{mc}(\theta)$, we denote the coordinates of the centres of curvature with $S_{mc}(x_{mc}, y_{mc}, z_{mc})$ and $S_d(x_d, y_d, z_d)$ and then calculate the x_{int} and y_{int} coordinates of the intersection, by calculating the intersection of the nanodroplet with the microcap, where we obtain x_{int} as function of z (Eq.(3.12)), where z goes from zero to point P_a. Then we calculate y_{int} by solving the sphere equation of either the microcap or the nanodrop (here origin of the coordinate system is in S_{mc}),

$$x_{int}(z) = \frac{x_d}{2} + \frac{R^2 - r^2 - (z_d - z_{mc})(2z - z_{mc} - z_d)}{2x_d}. \quad (3.12)$$

We then obtain

$$\rho_{mc}(\theta) = 2\arctan\frac{y_{int}(z)}{x_{int}(z)}. \quad (3.13)$$

However, if the nanodroplet covers the apex of the spherical microcap, then the integration eq. (3.11) will not result in the total contact surface, because part of the spherical microcap above the point P_a will not be included in this integration. Hence, we must "manually" add the value of the surface area of the spherical cap above the point P_a on the spherical microcap. In the same way we can calculate A_2: we first calculate the surface area of the nanodroplet captured beneath the surface of the spherical microcap, and subtract it from

the full spherical cap surface area of the nanodroplet. We can do that by reverting the x and y axes orientation and placing the origin of the spherical coordinate system to S_d. Also, we switch the places of the microcap and the nanodrop terms in the Eq. (3.12) to calculate $\rho_d(\theta)$. The final result is

$$A_2 = 2r^2\pi(1-\cos\theta_{fs}) - r^2\int_{\theta_A}^{\theta_{fs}} \rho_{\mathrm{d}}(\theta)\sin\theta\,\mathrm{d}\theta \tag{3.14}$$

To numerically calculate the volume of the nanodroplet, we first calculate the volume of a part of the full spherical cap of the nanodroplet, that is beneath the surface of the microcap (V'). To do so, we denote the intersection surface of the drop and the microcap on the flat substrate (Figure 3.2 d, top view intersection area) as A_{int}. The microcap and the nanodroplet surfaces are denoted as $z_{mc}(x,y)$ and $z_d(x,y)$. Then, we numerically evaluate

$$V' = \int_{A_{int}} \min[\mathrm{z_{mc}(x,y)}, \mathrm{z_d(x,y)}]\,\mathrm{d}A'. \tag{3.15}$$

Finally, we substract V' from the value of the full spherical cap volume to obtain the reduced volume of the nanodrop wetting the rim of the microcap.

firstinits=true]unsrt

References

[1] A. Mendez-Vilas, A. B. Jodar-Reyes, and M. L. Gonzalez-Martin. Ultrasmall Liquid Droplets on Solid Surfaces: Production, Imaging, and Relevance for Current Wetting Research. *Small*, 5:1366–1390, 2009.

[2] A. Moosavi, M. Rauscher, and S. Dietrich. Dynamics of nanodroplets on topographically structured substrates. *Journal of Physics: Condensed Matter*, 21(46):464120, 2009.

[3] H. Xu and X. Zhang. Formation, characterization and stability of oil nanodroplets on immersed substrates. *Adv. Colloid Interface Sci.*, 224:17–32, 2015.

[4] D. Lohse and X. Zhang. Surface nanobubbles and nanodroplets. *Rev. Mod. Phys.*, 87:981–1035, 2015.

[5] R. D. Narhe and D. A. Beysens. Nucleation and growth on a superhydrophobic grooved surface. *Phys. Rev. Lett.*, 93:076103, Aug 2004.

[6] S. C. Thickett, C. Neto, and A. T. Harris. Biomimetic surface coatings for atmospheric water capture prepared by dewetting of polymer films. *Advanced Materials*, 23(32):3718–3722, 2011.

[7] K. Rykaczewski. Microdroplet growth mechanism during water condensation on superhydrophobic surfaces. *Langmuir*, 28(20):7720–7729, 2012.

[8] Q. Zhang, M. He, J. Chen, J. Wang, Y. Song, and L. Jiang. Anti-icing surfaces based on enhanced self-propelled jumping of condensed water microdroplets. *Chem. Commun.*, 49:4516–4518, 2013.

[9] M. J. Kreder, J. Alvarenga, P. Kim, and J. Aizenberg. Design of anti-icing surfaces: smooth, textured or slippery? *Nature Reviews Materials*, 1:15003 EP –, 2016.

[10] M. Wen, L. Wang, M. Zhang, L. Jiang, and Y. Zheng. Antifogging and icing-delay properties of composite micro- and nanostructured surfaces. *ACS Applied Materials & Interfaces*, 6(6):3963–3968, 2014.

[11] H. R. Holmes and K. F. Böhringer. Transporting droplets through surface anisotropy. *Microsystems & Nanoengineering*, 1:15022 EP –, 09 2015.

[12] L. Bian, Y. Weng, and X. Li. Observation of micro-droplets on metal surface in early atmospheric corrosion. *Electrochemistry Commun.*, 7(10):1033 – 1038, 2005.

[13] J. Chen, J. Wang, E. Han, and W. Ke. In situ observation of formation and spreading of micro-droplets on magnesium and its alloy under cyclic wet–dry conditions. *Corrosion Science*, 49(3):1625 – 1634, 2007.

[14] J. Chen, J. Wang, E. Han, and W. Ke. {ESEM} observation of the process of hydrogen generation around the micro-droplets forming on {AZ91} magnesium alloy. *Electrochemistry Commun.*, 10(4):577 – 581, 2008.

[15] H. Li, Q. Yang, G. Li, M. Li, S. Wang, and Y. Song. Splitting a droplet for femtoliter liquid patterns and single cell isolation. *ACS Appl. Mater. Interfaces*, 7(17):9060–9065, 2015.

[16] C. H. Choi, S. M. Kang, S. H. Jin, H. Yi, and C. S. Lee. Controlled fabrication of multicompartmental polymeric microparticles by sequential micromolding via surface-tension-induced droplet formation. *Langmuir*, 31(4):1328–1335, 2015.

[17] K. O. Zamuruyev, H. K. Bardaweel, C. J. Carron, N. J. Kenyon, O. Brand, J. P. Delplanque, and C. E. Davis. Continuous droplet removal upon dropwise condensation of humid air on a hydrophobic micropatterned surface. *Langmuir*, 30(33):10133–10142, 2014.

[18] A. R. Parker and C. R. Lawrence. Water capture by a desert beetle. *Nature*, 414(6859):33–34, 2001.

[19] J. Ju, H. Bai, Y. Zheng, T. Zhao, R. Fang, and L. Jiang. A multi-structural and multi-functional integrated fog collection system in cactus. *Nature Commun.*, 3:1247, 2012.

[20] Y. Zheng, H. Bai, Z. Huang, X. Tian, F. Q. Nie, Y. Zhao, Jin Zhai, and Lei Jiang. Directional water collection on wetted spider silk. *Nature*, 463(7281):640–643, 2010.

[21] Y. T. Cheng and D. E. Rodak. Is the lotus leaf superhydrophobic? *Applied*

Physics Letters, 86(14):144101, 2005.

[22] Y. T. Cheng, D. E. Rodak, C. A. Wong, and C.A. Hayden. Effects of micro-and nano-structures on the self-cleaning behaviour of lotus leaves. *Nanotechnology*, 17(5):1359, 2006.

[23] J. Guzowski and P. Garstecki. Droplet clusters: Exploring the phase space of soft mesoscale atoms. *Phys. Rev. Lett.*, 114:188302, 2015.

[24] A. Ma, J. Xu, X. Zhang, B. Zhang, D. Wang, and H. Xu. Interfacial nanodroplets guided construction of hierarchical au, au-pt, and au-pd particles as excellent catalysts. *Sci. Rep.*, 4, 2014.

[25] D. J. Kraft, W. S. Vlug, C. M. van Kats, A. van Blaaderen, A. Imhof, and W. K. Kegel. Self-assembly of colloids with liquid protrusions. *Journal of the American Chemical Society*, 131(3):1182–1186, 2009.

[26] D. J. Kraft, J. Hilhorst, M. A. P. Heinen, M. J. Hoogenraad, B. Luigjes, and W. K. Kegel. Patchy polymer colloids with tunable anisotropy dimensions. *The Journal of Physical Chemistry B*, 115(22):7175–7181, 2011.

[27] A. Giacomello, L. Schimmele, and S. Dietrich. Wetting hysteresis induced by nanodefects. *Proc. Natl. Acad. Sci. USA*, 113:E262–E271, 2016.

[28] L. Schimmele and S. Dietrich Line tension and the shape of nanodroplets. *Eur. Phys. J. E*, 30(4):427–430, 2009.

[29] M. Rauscher and S. Dietrich. Wetting phenomena in nanofluidics. *Annu. Rev. Mater. Res.*, 38:143–172, 2008.

[30] N. H. Fletcher. Size effect in heterogeneous nucleation. *The Journal of Chemical Physics*, 29(3):572–576, 1958.

[31] R. Seemann, M. Brinkmann, E. J. Kramer, F. F. Lange, and R. Lipowsky. Wetting morphologies at microstructured surfaces. *PNAS*, 102(6):1848–1852, 2005.

[32] S. Peng, D. Lohse, and X. Zhang. Spontaneous pattern formation of surface nanodroplets from competitive growth. *ACS Nano*, 9:11916–11923, 2015.

[33] X. Zhang and W. Ducker. Formation of interfacial nanodroplets through changes in solvent quality. *Langmuir*, 23(25):12478–12480, 2007.

[34] S. Peng, D. Lohse, and X. Zhang. Microwetting of supported graphene on hydrophobic surfaces revealed by polymerized interfacial femtodroplets. *Langmuir*, 30:10043–10049, 2014.

[35] X. Zhang, Z. Lu, H. Tan, L. Bao, Y. He, C. Sun, and D. Lohse. Formation of surface nanodroplets under controlled flow conditions. *Proc. Natl. Acad. Sci. USA*, 112:9253–9257, 2015.

[36] L. Bao, A. R. Rezk, L. Y. Yeo, and X. Zhang. Highly ordered arrays of femtoliter surface droplets. *Small*, 11:4850–4855, 2015.

[37] X. H. Zhang, J. M. Ren, H. J. Yang, Y. H. He, J. F. Tan, and G. G. Qiao. From transient nanodroplets to permanent nanolenses. *Soft Matter*, 8:4314–4317, 2012.

[38] L. Mahadevan, M. Adda-Bedia, and Y. Pomeau. Four-phase merging in sessile compound drops. *J. Fluid Mech.*, 451:411–420, 2002.

[39] L. Gao and T. J. McCarthy. How wenzel and cassie were wrong. *Langmuir*, 23:3762–3765, 2007.

[40] G. McHale. Cassie and wenzel: Were they really so wrong? *Langmuir*, 23:8200–8205, 2007.

[41] X. Zhang, J. Wang, L. Bao, E. Dietrich, R. C. A .van der Veen, S. Peng, J. Friend, H. J. W. Zandvliet, L. Yeo, and D. Lohse. Mixed mode of dissolving immersed nanodroplets at a solid–water interface. *Soft Matter*, 11(10):1889–1900, 2015.

3

4

Sessile nanodroplets on elliptical patches of enhanced lyophilicity

We theoretically investigate the shape of a nanodroplet on a lyophilic elliptic patch in a lyophobic surrounding on a flat substrate. To compute the droplet equilibrium shape we minimize its interfacial free energy, using both Surface Evolver and Monte Carlo calculations, finding good agreement between the two methods. We observe different droplet shapes, which are controlled by the droplet volume and the aspect ratio of the ellipse. In particular, we study the behaviour of the nanodroplet contact angle along the three-phase contact line, explaining the different droplet shapes. While the nanodroplet contact angle is constant and fixed by Young's law inside and outside the elliptical patch, its value varies along the rim of the elliptical patch. We find that due to pinning of the nanodroplet contact line at the rim of the elliptical patch, which has a non-constant curvature, there is a regime of aspect ratios of the elliptical patch, in which the nanodroplet starts expanding to the lyophobic part of the substrate, although there is still a finite area of the lyophilic patch free to be wetted.[1]

[1]Based on: I. Dević, G. Soligno, M. Dijkstra, R. van Roij , X. Zhang and D. Lohse, Sessile nanodroplets on elliptical patches of enhanced lyophilicity, *Langmuir* 33:2744-2749, 2017. Gradient descent calculation is part of the thesis

4.1 Introduction

Equilibrium shapes of nanodroplets, which are positioned on a patterned surface, are of great interest to both fundamental research [1–8] and many industrial applications such as printing [9], microfluidics [10] and catalysis [11]. If the nanodroplet is deposited on a homogeneous substrate, it will form a spherical cap, with a contact angle dictated by Young's law. However, if we pattern the flat substrate with chemical heterogeneities, the nanodroplet will no longer form a spherical cap, but another equilibrium shape with constant mean curvature, which is determined by the Young-Laplace equation.[12] If the length scale of the chemical heterogeneities is much smaller than the length scale of the nanodroplet and if the heterogeneities are regularly and densely distributed over the substrate, the nanodroplet has the apparent contact angle predicted by a modified Cassie-Baxter law.[13, 14] However, when the chemical heterogeneities are of the same length scale as the nanodroplet itself, a strong coupling of droplet shape and surface heterogeneities emerges. In such a case, we have to numerically minimise the interfacial free energy of the nanodroplet, as in three dimensions the minimisation problem can often not be solved analytically.[15, 16]. The numerical techniques used in calculating the nanodroplet equilibrium shapes include the gradient descent method [17, 18], metropolis stochastic calculations [19], hybrid energy-minimizations [20] and lattice Boltzman calculations [21]. Wetting experiments and calculations on isolated chemical defects, such as circular islands [22] and single stripes [23–26], have shown that the contact angles along the three-phase contact line are determined by the local properties of the substrate, which will be discussed in more detail in the "Results" section.

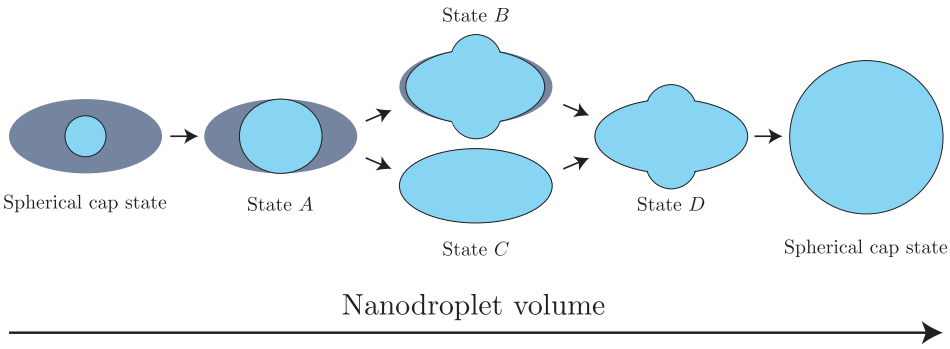

Figure 4.1: Graphical representation of all possible droplet states as seen from top view.

In this paper we analyze the morphology of a nanodroplet on a single lyophilic elliptical patch on a flat substrate. The single elliptical patch is an intermediate case between a circular island and a single stripe, but it is

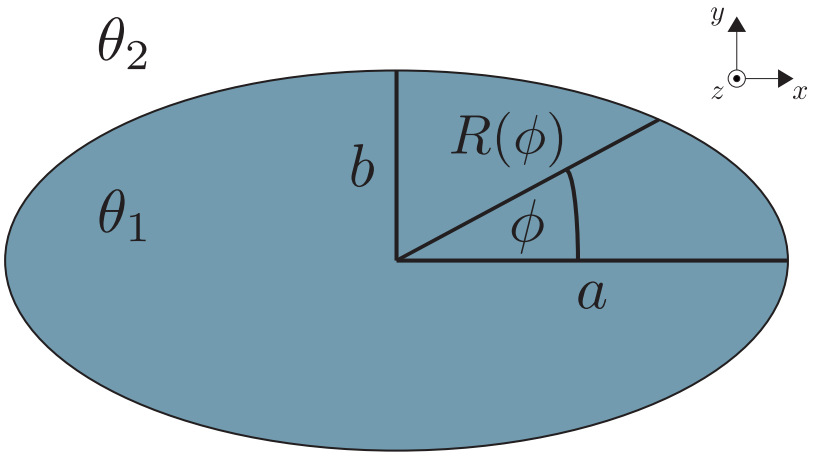

Figure 4.2: Geometry of an elliptical patch defined by semi-axises a and b, with Young's contact angle θ_1 inside the patch and θ_2 outside the patch.

qualitatively unique, since the rim of the elliptical patch has a non-constant curvature, which affects the nanodroplet equilibrium shape and shape transformations, via the Young-Laplace equation. In Figure 4.1 we show the possible nanodroplet states we expect to find in this system, which will be explained in more detail further on in the paper. These states are analogous to those of the nanodroplet positioned on a single finite lyophilic stripe [24], with the exception of the long cylindrical drops, which cannot be obtained due to the curvature of the rim of the elliptical patch. We expect two possible pathways, either through state B or through state C, as the contact line of the nanodroplet has the tendency to pin itself in the region of the sharp transition of wettability (rim of the elliptical patch), which determines the value of one out of the two principal radii of curvature.

4.2 Theoretical definition of the problem

Due to the small size of a nanodroplet, we can neglect the effect of gravity. Moreover, for simplicity we ignore line tension contributions. Therefore, the shape of the nanodroplet is controlled by the surface tension between the three phases present in the system [27] (s-solid, ℓ-liquid and v-vapor). If the droplet is in contact with a flat substrate, described by the plane $z = 0$, with patterned chemical heterogeneities, we can write the interfacial free energy E as

$$E = \gamma_{\ell v} A_{\ell v} + \int_{A_{s\ell}} (\gamma_{s\ell}(x,y) - \gamma_{sv}(x,y))\, dA \tag{4.1}$$

where γ_{ij} denotes the surface tension between phase i and j, while A_{ij} represents the area of the interface between these two phases. Normalizing the

interfacial free energy E with $\gamma_{\ell v}$, and using Young's law for the contact angle

$$\cos\theta_Y(x,y) = \frac{\gamma_{sv}(x,y) - \gamma_{s\ell}(x,y)}{\gamma_{\ell v}}, \tag{4.2}$$

we obtain the expression for a reduced interfacial free energy $\tilde{E}$

$$\tilde{E} \equiv \frac{E}{\gamma_{\ell v}} = A_{\ell v} - \int_{A_{s\ell}} \cos\theta_Y(x,y)\, dA. \tag{4.3}$$

4.3 Numerical methods and procedure

We minimize Eq.(4.3) under the volume constraint to obtain the equilibrium shape of the nanodroplet. The geometry of our system is presented in Figure 4.2, where the origin of the coordinate system (x, y, z) is in the center of the elliptical patch, with large semi-axis a and small semi-axis b. We define ϕ as a viewing angle, where the value zero corresponds to the direction of the x-axis, while $R(\phi)$ denotes the distance from the center of the elliptical patch, with which we will describe the contact line of the nanodroplet. We define the Young contact angle in our system as

$$\theta_Y = \begin{cases} \theta_1, \text{ if } (x,y) \in \frac{x^2}{a^2} + \frac{y^2}{b^2} \leqslant 1 \\ \theta_2, \text{ if } (x,y) \in \frac{x^2}{a^2} + \frac{y^2}{b^2} > 1 \end{cases} \tag{4.4}$$

where θ_1 is always smaller than θ_2, so the surface of the elliptical patch has an enhanced lyophilicity compared to the rest of the flat substrate.

We minimize Eq. (4.3) numerically with the Surface Evolver [17, 18] and with Monte Carlo [19] calculations. Surface Evolver is a free software package for minimizing the interfacial free energy, developed by Brakke, which was used with great success to calculate equilibrium wetting morphologies [13, 23, 24, 28, 29]. After setting the initial shape of the droplet, Surface Evolver triangulates the interface of the nanodroplet and moves the points of each triangle with an energy gradient descent method. The contact area $A_{s\ell}$ is omitted from the Surface Evolver calculation and we replace it with the integral of the second term of Eq. (4.3). In the Monte Carlo calculation we use a simulated annealing method to calculate the global minimum of the interfacial free energy (Eq. (4.3)), with the fluid-fluid interface represented by a grid of points. During the Monte Carlo simulation, a random shift in the morphology of the nanodroplet is introduced, and the interfacial free energy values (Eq. (4.3)) before and after the shift are compared. If the value of the interfacial free energy is smaller after the shift, we accept the new morphology. If it is larger, we assign a probability of accepting the new morphology weighted by a temperature-like

parameter T. This procedure is repeated continuously while T is gradually lowered, and the simulation ends when $T = 0$ (Metropolis algorithm) [19]. In all the presented calculations we use the large semi-axis a as our unit of length, while we consider different aspect ratios b/a by tuning the small semi-axis b, and different volumes V/a^3 of the nanodroplet. The values of the Young's contact angles in all calculations are set to $\theta_1 = 30°$ (lyophilic patch) and $\theta_2 = 60°$ (lyophobic surface). Firstly, we position the nanodroplet center of mass above the center of the elliptical patch and we set the nanodroplet initial volume to $V = 0.01\,a^3$. After calculating the nanodroplet equilibrium shape, i.e. corresponding to the minimum of the interfacial free energy, we increment the nanodroplet volume by $\Delta V = 0.01\,a^3$ and recalculate its equilibrium shape. We repeat this process until we reach $V = a^3$.

4.4 Results

When the nanodroplet is sufficiently small to have the whole three-phase contact line inside the elliptical patch, or when it is large enough to have the whole contact line outside the elliptical patch, the nanodroplet has a spherical-cap shape, with the contact angle defined by Eq. (4.4). We analytically calculate the threshold volumes V_{min} and V_{max} of the nanodroplet, for which the nanodroplet is, respectively, too large for forming the spherical-cap shape inside the patch or sufficiently large for forming the spherical-cap shape completely covering the elliptical patch, namely

$$V_{min} = \frac{b^3\pi}{3\sin^3\theta_1}(\cos^3\theta_1 - 3\cos\theta_1 + 2), \tag{4.5}$$

$$V_{max} = \frac{a^3\pi}{3\sin^3\theta_2}(\cos^3\theta_2 - 3\cos\theta_2 + 2), \tag{4.6}$$

which correspond, using $\theta_1 = 30°$ and $\theta_2 = 60°$, to $V_{min} \approx 0.431\,b^3$ and $V_{max} \approx 1.007\,a^3$. For all the values of the nanodroplet volume between threshold volumes V_{min} and V_{max}, the nanodroplet will be in one of the following four possible morphologies:

- Droplet state A: the nanodroplet has a part of the three-phase contact line pinned at the rim of the elliptical patch, while the rest of the contact line is located inside the elliptical patch. As we increase its volume, the nanodroplet can evolve to the droplet state B or C, depending on the aspect ratio of the elliptical patch.

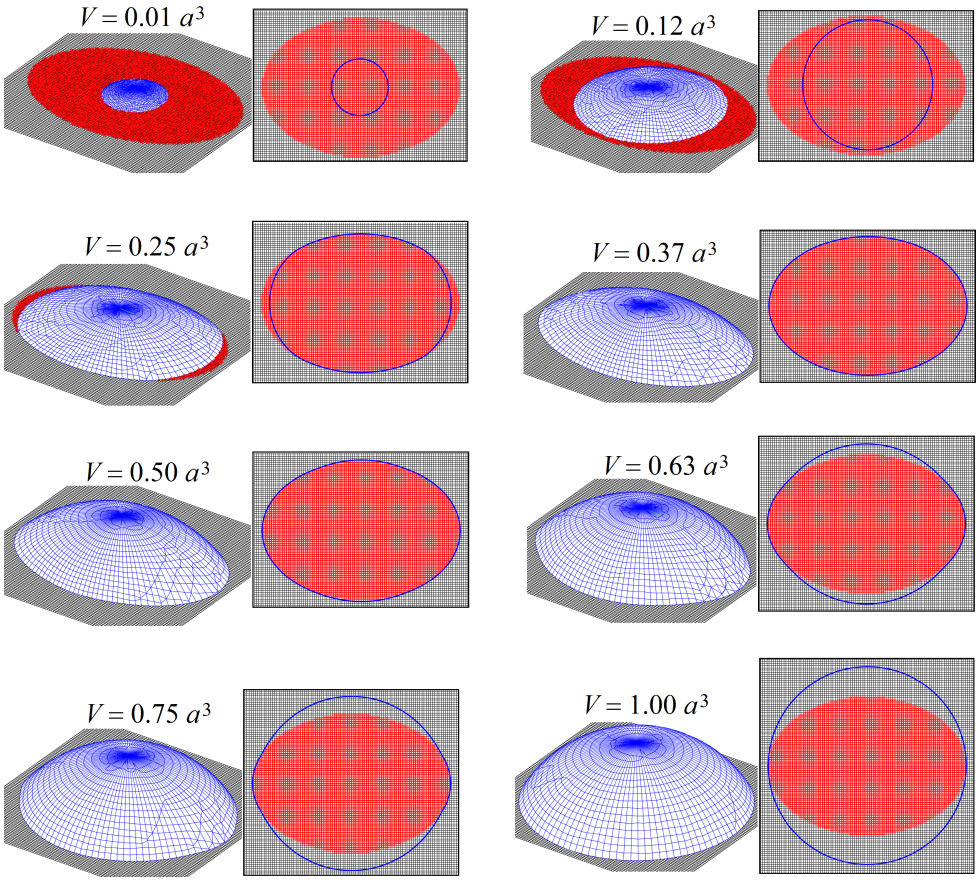

Figure 4.3: Equilibrium shapes (blue grid) of a nanodroplet with increasing volume on an elliptical patch (red area) with aspect ratio b/a = 0.7, as obtained from Monte Carlo calculations. The respective right figures show a top view of the three-phase contact line (blue line).

- Droplet state B: the nanodroplet partially spreads outside the elliptical patch, although the elliptical patch (which is more lyophilic) is not fully wetted.
- Droplet state C: the whole three-phase contact line of the nanodroplet is pinned at the rim of the elliptical path.
- Droplet state D: part of the nanodroplet contact line is still pinned to the rim of the elliptical patch, while the rest of the contact line is outside of the elliptical patch. Both state B and state C undergo a morphological transformation to state D, once the volume has become sufficiently large.

In Figure 4.3, we present results for the equilibrium shapes of a nanodroplet on an elliptical patch of aspect ratio $b/a = 0.7$ as obtained from Monte Carlo simulations for varying droplet volumes V as labeled. The results as obtained from the Surface Evolver are very similar (Figure 4.4). We find that the shape transformation proceeds via droplet state C to state D as anticipated in Figure

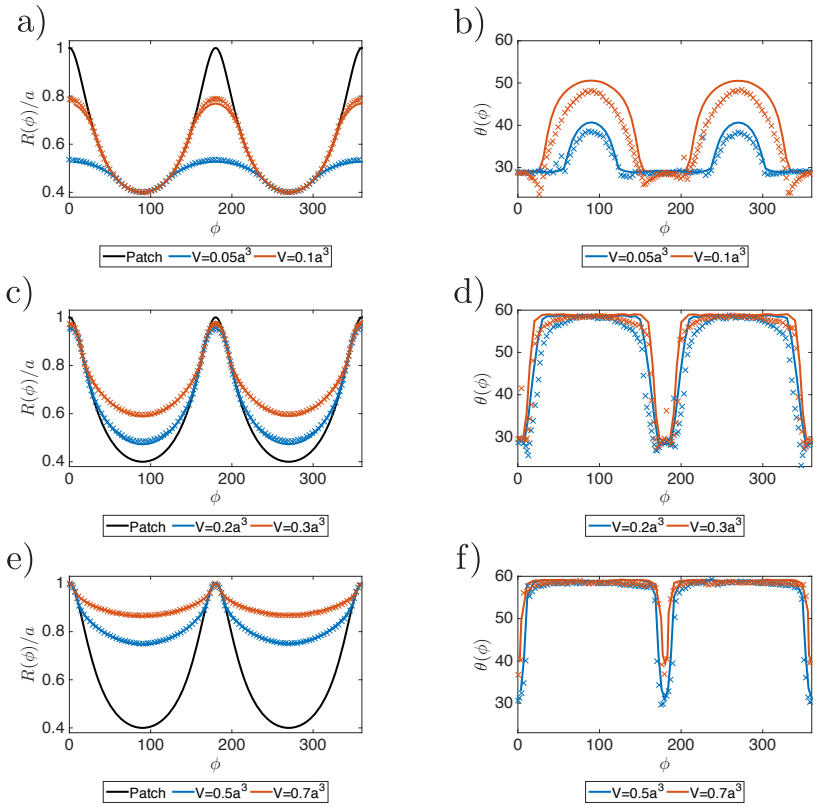

Figure 4.4: Position of the contact line $R(\phi)$ and the local contact angle $\theta(\phi)$ of the nanodroplet wetting an elliptical patch of aspect ratio $b/a = 0.4$, as a function of the viewing angle ϕ and for varying droplet volumes as labeled. We show $R(\phi)$ and $\theta(\phi)$ for the nanodroplet in state A in a) and b), for the nanodroplet in state B in c) and d), for the nanodroplet in state D in e) and f). Solid lines show results from the Surface Evolver calculation, while the markers present results from the Monte Carlo calculations.

4.1 upon increasing the droplet volume V. We now focus on the properties of the three-phase contact line and the local contact angle of the nanodroplet. In Figure 4.4 we show the position of the contact line $R(\phi)$ and the local contact angle $\theta(\phi)$ as a function of the viewing angle ϕ for different volumes of the nanodroplet, corresponding to different droplet states. For the chosen aspect ratio of the elliptical patch $b/a = 0.4$, the nanodroplet will undergo the transformation from droplet state A to state B, therefore avoiding state C. We notice from these results, that along the contact line of the nanodroplet, the local contact angle is exactly the Young's angle predicted from Eq. (4.4), if the contact line is locally either inside (θ_1) or outside (θ_2) the elliptical patch. However, when the contact line is exactly at the rim of the elliptical patch, Young's law cannot be obeyed [12, 24] and the local contact angle has a value between θ_1 and θ_2. Although Young's law cannot be obeyed, the net force exhibited on the nanodroplet is zero, due to the inversion symmetry of the system with respect to the x and y axes. When the nanodroplet volume reaches

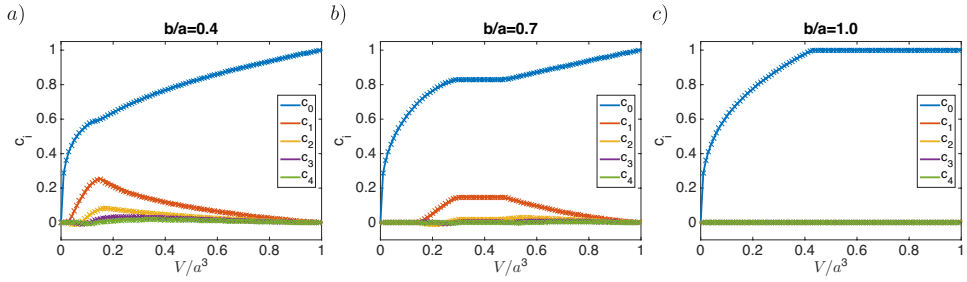

Figure 4.5: Expansion of $R(\phi)$ into a harmonic series as described in Eq.(4.7), for different values of the volume of the nanodroplet (V/a^3) and different aspect ratios of the elliptical patch: (a) b/a=0.4, (b) b/a=0.7, and (c) b/a=1. Results are presented in the same way as in Figure 4.4: solid lines correspond to Surface Evolver calculations, while the markers correspond to the Monte Carlo calculations.

the value of V_{min}, the contact line starts touching the rim of the elliptical patch, and at this point, the local contact angle starts increasing and the nanodroplet transforms from state A to state B. As we further increase the volume of the nanodroplet, once the value of the local contact angle reaches θ_2, the contact line of the nanodroplet will locally leave the rim of the elliptical patch and will move outside the patch. Since the rim of the elliptical patch has a non-constant curvature, the nanodroplet cannot have an equilibrium morphology where the local contact angle has a value of θ_2 and is constant along the contact line in regions where it is pinned to the rim. This fact determines whether the growing nanodroplet will go through state B or state C. For a given volume, when $R(90°) = R(270°) = b$ and $\theta(90°) = \theta(270°) = \theta_2$, if $R(0°) = R(180°) < a$, the nanodroplet will undergo the morphological transition from state A to state B. Instead, if $R(0°) = R(180°) = a$, the nanodroplet will be in state C. Both state B and state C eventually go through the transition to state D. Once the nanodroplet volume reaches the value of V_{max}, the nanodroplet equilibrium shape is a spherical cap with Young's contact angle θ_2.

We can study the transitions in a clearer way if we expand the function $R(\phi)$ into a (truncated) harmonic series as

$$\frac{R(\phi)}{a} = c_0 + \sum_{i=1}^{i=4} c_i \cos(2i\phi) \tag{4.7}$$

In Figure 4.5, we present coefficients from Eq. (4.7) as a function of the volume of the nanodroplet, for three different aspect ratios, which represent three different scenarios of droplet states. As already mentioned, for the value of the aspect ratio of the elliptical patch $b/a = 0.4$ (Figure 4.5a), the nanodroplet cannot wet the elliptical patch in state C, while for the value of $b/a = 0.7$ (Figure 4.5b), the nanodroplet cannot be in state B, which is visible from constant

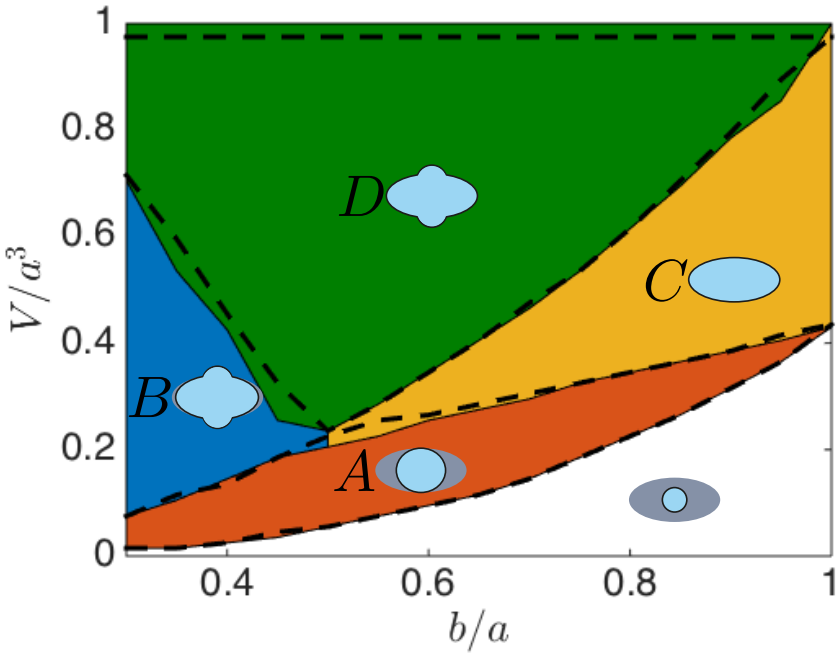

Figure 4.6: State diagram of the droplet morphologies as a function of the aspect ratio b/a of the elliptical patch (with in-side patch contact angle $\theta_1 = 30$ and out-side patch contact angle $\theta_2 = 60$) and the reduced volume V/a^3 of the nanodroplet. Solid lines present volume thresholds calculated in the Surface Evolver calculation, while dashed lines (in good agreement with the solid lines) present Monte Carlo results.

coefficient values for different values of the volume of the nanodroplet (contact line has the same position for different values of the volume of nanodroplet). Once the value of the coefficient c_1 reaches its global maximum, the nanodroplet goes through a morphological transition from state A, to either state B or C, depending on the value of $R(0°)$ and $R(90°)$ when $\theta(90°)$ and $\theta(270°)$ reach the value θ_2. As the volume becomes larger, all the higher harmonics go to zero, as the nanodroplet becomes a spherical cap again.[22] We notice that for a circular patch, where $b/a = 1$ (Figure 4.5c), all the higher harmonics remain zero, for any volume of the nanodroplet, since the nanodroplet has a spherical cap shape for any volume. Small deviations of the harmonics close to the nanodroplet volume $V = a^3$ are a numerical artefact from Surface Evolver, due to a complicated definition of the interfacial energy on the flat substrate for this particular system. We summarise all of our results in the state diagram presented in Figure 4.6, where we show the nanodroplet morphological states with respect to the nanodroplet volume V and the elliptical patch aspect ratio b/a. Note that the presented state diagram holds for inside-patch and outside-patch Young's contact angles given by $\theta_1 = 30°$ and $\theta_2 = 60°$, respectively, so it can be quantitatively different for other combinations of these two values.

4.5 Conclusion

We have calculated the equilibrium shapes of nanodroplets, on elliptical patches of enhanced lyophilicity with two different numerical methods and obtained good agreement between the two methods. With this work, we have connected the equilibrium shapes of a nanodroplet on isolated circular islands and the single stripe with all the intermediate cases with varying aspect ratio b/a of the elliptical patch. We calculated all the threshold volumes at which a morphological transition occurs for the given Young angles ($\theta_1 = 30°$ and $\theta_2 = 60°$), which are summarized in Figure 4.6. The droplet states we observe are similar to those reported on single lyophilic stripes [23–25]. However, due to the curvature of the rim of the elliptical patch, we do not observe long cylindrical drops on the elliptical patch. For practical applications of the elliptical patch, such as in catalysis, the separation of the aspect ratio of the elliptical patch into two regimes, where either the state B or state C occurs, is an important result. If we think of chemical patterning as an investment in the substrate to be more efficient (isolation of certain liquid on the patch), then the expansion of the contact line of the nanodroplet outside of the elliptical patch when there is still area available inside the elliptical patch is an inefficient way of patterning.

References

[1] A Marmur. Contact angle hysteresis on heterogeneous smooth surfaces. *J. Colloid Interface Sci.*, 168:40–46, 1994.

[2] P. G. de Gennes, F. Brochard-Wyart, and D. Quere. *Capillarity and wetting phenomena: drops, bubbles, pearls, waves.* Springer, New York, 2004.

[3] David Quere. Wetting and roughness. *Annu. Rev. Mater. Res.*, 38:71–99, 2008.

[4] P. G. de Gennes. Wetting: statics and dynamics. *Rev. Mod. Phys.*, 57:827, 1985.

[5] S. Herminghaus, M. Brinkmann, and R. Seemann. Wetting and dewetting of complex surface geometries. *Annu. Rev. Mater. Res.*, 38:101–121, 2008.

[6] M Rauscher and S Dietrich. Wetting phenomena in nanofluidics. *Annu. Rev. Mater. Res.*, 38:143–172, 2008.

[7] D. Lohse and X. Zhang. Surface nanobubbles and nanodroplets. *Rev. Mod. Phys.*, 87:981–1035, 2015.

[8] Antonio Mendez-Vilas, Ana Belen Jodar-Reyes, and Maria Luisa Gonzalez-Martin. Ultrasmall Liquid Droplets on Solid Surfaces: Pro-

duction, Imaging, and Relevance for Current Wetting Research. *Small*, 5:1366–1390, 2009.

[9] D. Soltman, B. Smith, H. Kang, S. J. S. Morris, and V. Subramanian. Methodology for inkjet printing of partially wetting films. *Langmuir*, 26:15686–15693, 2010.

[10] T. Lee, E. Charrault, and C. Neto. Interfacial slip on rough, patterned and soft surfaces: A review of experiments and simulations. *Adv. Colloid Interface Sci.*, 210:21–38, 2014.

[11] B. S. Clausen, J. Schiøtz, L. Gråbæk, C. V. Ovesen, K. W. Jacobsen, J. K. Nørskov, and H. Topsøe. Wetting/ non-wetting phenomena during catalysis: Evidence from in situ on-line exafs studies of cu-based catalysts. *Top. Catal.*, 1:367–376, 1994.

[12] P. Lenz and R. Lipowsky. Morphological transitions of wetting layers on structured surfaces. *Phys. Rev. Lett.*, 90:1920–1923, 1998.

[13] S. Brandon, N. Haimovich, E. Yeger, and A. Marmur. Partial wetting of chemically patterned surfaces: The effect of drop size. *J. Colloid Interface Sci.*, 263:237–243, 2003.

[14] A. Marmur and E. Bittoun. When wenzel and cassie are right: Reconciling local and global considerations. *Langmuir*, 25:1277–1281, 2009.

[15] Lichao Gao and Thomas J. McCarthy. How wenzel and cassie were wrong. *Langmuir*, 23:3762–3765, 2007.

[16] G McHale. Cassie and wenzel: Were they really so wrong? *Langmuir*, 23:8200–8205, 2007.

[17] K. A. Brakke. The surface evolver. *Exp. Math.*, 1:141–165, 1992.

[18] K. A. Brakke. Surface evolver manual, version 2.70, 2013.

[19] G. Soligno, M. Dijkstra, and R. van Roij. The equilibrium shape of fluid-fluid interfaces: Derivation and a new numerical method for young's and young-laplace equations. *J. Chem. Phys.*, 141:244702, 2014.

[20] H. Matsui, Y. Noda, and T. Hasegawa. Hybrid energy-minimization simulation of equilibrium droplet shapes on hydrophilic/hydrophobic patterned surfaces. *Langmuir*, 28:15450–15453, 2012.

[21] A. Dupuis, J. Léopoldès, D. G. Bucknall, and J. M. Yeomans. Control of drop positioning using chemical patterning. *Appl. Phys. Lett.*, 87:024103, 2005.

[22] C. W. Extrand. Contact angles and hysteresis on surfaces with chemically heterogeneous islands. *Langmuir*, 19:3793–3796, 2003.

[23] A. A. Darhuber, S. M. Troian, and S. Wagner. Morphology of liquid microstructures on chemically patterned surfaces. *J. Appl. Phys.*, 87:7768–7775, 2000.

[24] M. Brinkmann and R. Lipowsky. Wetting morphologies on substrates

with striped surface domains. *J. Appl. Phys.*, 92:4296–4306, 2002.

[25] D. Ferraro, C. Semprebon, T. Tóth, E. Locatelli, M. Pierno, G. Mistura, and M. Brinkmann. Morphological transitions of droplets wetting rectangular domains. *Langmuir*, 28:13919–13923, 2012.

[26] H. P. Jansen, O. Bliznyuk, E. S. Kooij, B. Poelsema, and H. J. W. Zandvliet. Simulating anisotropic droplet shapes on chemically striped patterned surfaces. *Langmuir*, 28:499–505, 2012.

[27] J. T. Woodward, H. Gwin, and D.K. Schwartz. Contact angles on surfaces with mesoscopic chemical heterogeneity. *Langmuir*, 16:2957–2961, 2000.

[28] R. Seemann, M. Brinkmann, E. J. Kramer, F. F. Lange, and R. Lipowsky. Wetting morphologies at microstructured surfaces. *Proc. Natl. Acad. Sci. U. S. A.*, 102(6):1848–1852, 2005.

[29] Y. Chen, B. He, J. Lee, and N. A. Patankar. Anisotropy in the wetting of rough surfaces. *J. Colloid Interface Sci.*, 281:458–464, 2005.

5

Stable shapes of sliding drop across a chemical step

Energy minimisation of a droplet under the influence of a body force is performed. Employing Surface evolver, we simulate the system of a sliding droplet, since it represents the most trivial example for an auxiliary body force and introduces a chemical step into the system, with the body force pushing the droplet from the lyophilic part to the lyophobic part of the substrate. We present phase diagrams, in which we show for which droplet sizes there are dynamically inaccessible equilibrium shapes. We also identify what physical laws determine the threshold volume. While this given system was studied previously in the literature using contact angle hysteresis laws, we present the full static thermodynamical solution of the interfacial energy including the contact energy, while omitting the hysteresis effects from the contact line. [1]

[1] Based on I. Dević, J. M. Encarnación Escobar and D. Lohse, submitted

5.1 Introduction

Droplet wetting on *chemically patterned* surfaces has a wide range of applications and correspondingly raises both scientific [1–4] and industrial interest [5–7]. In the case of small scale systems such as catalysis [7] and microfluidics [5], the wetting properties dictate the efficiency of the system, while in the case of large systems, small wetting effects on the substrates can cause changes in the macroscopic flow in setups such as in wall-bounded flows [8]. Although most of these processes are dynamical, there are also still a lot of unanswered questions when it comes to stable (equilibrium) droplet shapes.

To obtain the equilibrium shape, by definition one has to minimise the interfacial energy of the droplet, which on a flat homogenuous substrate results in two important qualitative results: the droplet interface has a constant mean curvature which is a function of the droplet volume (Young-Laplace equation) and the contact angle is uniquely defined via three separate surface tensions on the three-phase contact line (Young's law). While the equilibrium shapes of the droplet on the chemical patterned substrate are visually very distinctive from the spherical cap, the previous two qualitative results are still present in those shapes [9–13].

The biggest problem in finding droplet equilibrium shapes on chemically patterned substrate is due to the geometrical complications which start to arise, because the droplet contact energy with the substrate becomes a function of the location of the contact area. The only exception to this is in the case of a regularly patterned (dense and periodic in space) substrate, where the Cassie-Baxter law application for chemically patterned substrates[14–16] is still valid, resulting in a nearly spherical-cap shape with the apparent contact angle predicted as an average contact angle of all chemical species present in the substrate, weighted by the respective species percentage of area it covers on the substrate. If one decreases the size of the droplet on that type of substrate, one will reach a critical volume at which the Cassie-Baxter law will not produce valid results, since the length scale of the contact area becomes similar to the length scale of the pattern; therefore, from the perspective of the droplet, the substrate can then be considered as strongly heterogeneous [14–16]. To obtain the droplet equilibrium shape in that regime, many numerical tools have been employed such as gradient descent methods [9–11, 17], Monte-Carlo calculations [18] and molecular dynamics [19].

In this paper we want to explore under what conditions a stable equilibrium shape exist for the geometry of a chemical step on a substrate and in addition a body force acting on the droplet. The most common example of this kind of problem is a sliding drop on a tilted chemically patterned substrate. This system has recently been explored quite a bit [20–24], however,

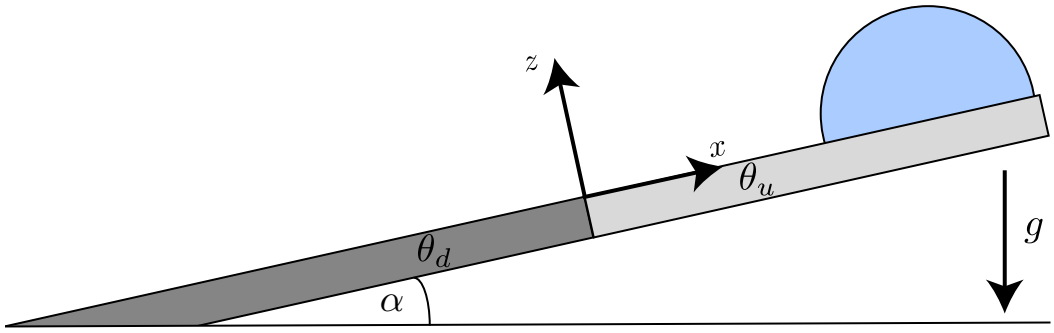

Figure 5.1: Properties of the system in which we are searching for stable shapes. The tilted substrate consists of two parts, in which the Young's angles are θ_d and θ_u, respectively.

in many cases it was done by removing the contact area contribution to the interfacial energy of the droplet and instead of it, local contact line hysteresis laws were introduced. The common name for such dynamical models is "contact line friction method", which will from now on be abbreviated as CLFM [22, 25]. CLFM can produce stable shapes and they were experimentally confirmed by Semprebon et al.[23] for values of Bond number smaller than 1.6, while for the larger Bond numbers CLFM results started to deviate from the experimental data. In various surfaces the contact angle hysteresis is small, so one approaches the limit where the contributions of the contact area to the interfacial energy has to be included and values of the advancing and the receding contact angle reduce to the value of Young's angle. Another common approximation in the analysis of sliding drops is to neglect the normal gravity component to the droplet, which basically means that those results are applicable to nano/micro-droplets, but once the length scale of the droplet becomes larger than the capillary length scale, the normal gravity component starts to deform the droplets significantly. In this paper we will perform both the analysis with and without the normal gravity component, to quantify its effect.

Using Surface Evolver [26, 27], the free gradient descent software, we will calculate the stable droplet shape on the tilted substrate with the chemical step, as shown in Figure 5.1. The tilted substrate consists of two parts, where the part below and above the chemical step respectively have the lyophobic Young's angle θ_d and the lyophilic Young's angle θ_u. Here the indices d and u stand for *down* and *up*, respectively. In the case of $\theta_d < \theta_u$, the droplet would prefer to travel down the chemical step even without the gravity, therefore we will explore the phase space where $\theta_d > \theta_u$. The substrate slope α denotes both the angle which the tilted substrate makes with the horizontal plane

and the connection between the gravity force and its components in the $x-z$ coordinate system.

5.2 Energy functionals

5.2.1 Omission of the normal gravity component

We will first consider the case where only the tangential gravity component plays a role, $g_x = g\sin\alpha$. To write down the total droplet energy, we must combine both interfacial and gravitational contributions, which results in

$$E = \gamma_{v\ell}A_{v\ell} + (\gamma_{s\ell}(x) - \gamma_{sv}(x))A_{s\ell} + \rho g_x \int_V x dV \tag{5.1}$$

where γ and A respectively denote surface tension and interfacial area, while their indices indicate between which two phases the surface tension and the interfacial area are defined, where s stands for solid (substrate), ℓ for the liquid of the droplet and v is used for the outer (e.g. vapor) phase. The last term on the right side of the equation is the potential energy of the droplet under the influence of the body force, where ρ is the droplet density and V the droplet volume. To nondimensionalise Eq. 5.1, we divide the whole equation by the surface tension $\gamma_{v\ell}$ and the square value of volume length scale $\ell_V \equiv V^{\frac{1}{3}}$ and obtain

$$\tilde{E} \equiv \frac{E}{\gamma_{v\ell}\ell_V^2} = \tilde{A}_{v\ell} - \cos\theta_Y(\tilde{x})\tilde{A}_{s\ell} + Bo_x \int_{\tilde{V}} \tilde{x} d\tilde{V} \tag{5.2}$$

where we have used Young's law for the equilibrium contact angle,

$$\cos\theta_Y(\tilde{x}) = \frac{\gamma_{sv}(\tilde{x}) - \gamma_{s\ell}(\tilde{x})}{\gamma_{v\ell}} = \begin{cases} \theta_d, \text{ if } \tilde{x} \leqslant 0 \\ \theta_u, \text{ if } \tilde{x} > 0 \end{cases} \tag{5.3}$$

and we have introduced the Bond number $Bo_x = \rho g_x \ell_V^2/\gamma_{v\ell}$, where index x indicates that it is defined with the respect to the tangential body force acceleration. Dimensionless quantities are labeled by tildes. By choosing the volume length scale as a characteristic length scale, we perform the minimisation of the Eq. 5.2 on the unit volume. Because of this, instead of looking at the Bond number as the ratio between capillary and gravitational forces, it is more convinient to think of Bond number as a squared ratio between the capillary and the volume lengthscale, since it can be expressed as $Bo_x = \ell_V^2/\ell_{cx}^2$, where ℓ_{cx} is the capillary length scale $\ell_{cx} = \sqrt{\gamma_{v\ell}/\rho g_x}$ determined by the influence of the tangential gravity component g_x. The second term, the contact energy term, in the dimensionless energy is the qualitative difference from CLFM, since this

term is used instead of the local contact angle hysteresis laws. In CLFM calculations, minimisation of the dimensionless energy without the contact energy term is performed, while the contact line is fixed and afterwards one would fix the interface position and update the contact line position by hysteresis law. This process is repeated until the stable shape is obtained. In our calculation, we minimise the dimensionless energy in a single take. The local contact angle in CLFM has an allowed range between the receding and the advancing contact angle and there is a hysteresis force locally acting on the contact line. When the droplet reaches its stable state, the net local hysteresis force along the contact line is a force with the opposite direction and the same value as the body force applied to the droplet.[22] The contact angle in our calculation is locally in a mechanical equilibrium, which means that the local contact angle always equals $\theta_Y(\tilde{x})$. The mechanical equilibrium of the outer interface is the same in both CLFM and our calculation, since the curvature has to satisfy the Young-Laplace equation, which is

$$2\gamma\kappa = \Delta p - \rho x g_x \tag{5.4}$$

where Δp is the pressure jump across the interface at $x = 0$ and κ is the mean interface curvature. In non-dimensional form Eq. 5.4 reads

$$2\tilde{\kappa} = \tilde{p} - Bo_x\tilde{x} \tag{5.5}$$

where $\tilde{p} \equiv \Delta\tilde{p} = \ell_V \Delta p/\gamma_{v\ell}$ denotes the dimensionless pressure jump at $\tilde{x} = 0$. Although in Eq. 5.5 we are expressing the mechanical equilibrium, the important geometrical result is that $\partial\kappa/\partial\tilde{x} = -Bo_x/2$, which will start playing a dominant effect in the cases of small value of θ_u, since the droplet will try to spread itself on the substrate, increasing the range of values of $\tilde{x}$ for the contact line. In general, the value of $\tilde{p}$ cannot be obtained analytically.

5.2.2 Inclusion of the normal gravity component

As already stated in the introduction of the paper, many studies so far have neglected the normal gravity component $g_z = g\cos\alpha$, due to the small size of the droplet and neglectable deformations caused by g_z. To include this interaction in the energy functional, we must add one term to the right hand side of Eq.5.1, which results in

$$E = \gamma_{v\ell}A_{v\ell} + (\gamma_{s\ell}(x) - \gamma_{sv}(x))A_{s\ell} + \rho g_x \int_V x dV + \rho g_z \int_V z dV \tag{5.6}$$

Eq. 5.6 is non-dimensionalized with the volume length scale ℓ_V as the characteristic length scale and outer surface tension $\gamma_{v\ell}$ as the characteristic surface tension. The resulting dimensionless equation is

$$\tilde{E} \equiv \frac{E}{\gamma_{v\ell}\ell_V^2} = \tilde{A}_{v\ell} - \cos\theta_Y(\tilde{x})\tilde{A}_{s\ell} + Bo_x \int_{\tilde{V}} \tilde{x} d\tilde{V} + Bo_z \int_{\tilde{V}} \tilde{z} d\tilde{V} \tag{5.7}$$

Similarly to the Young-Laplace equation (Eq. 5.4), the curvature κ has to follow

$$2\gamma\kappa = \Delta p - \rho x g_x - \rho z g_z \tag{5.8}$$

which in dimensionless from becomes

$$2\tilde{\kappa} = \tilde{p} - Bo_x\tilde{x} - Bo_z\tilde{z} \tag{5.9}$$

where $\tilde{p}$ is now the pressure at the $x = z = 0$. In this case, the curvature has to satisfy two geometrical relations, namely: $\partial\kappa/\partial\tilde{x} = -Bo_x/2$ and $\partial\kappa/\partial\tilde{z} = -Bo_z/2$. We can express the total Bond number Bo as

$$Bo = \frac{\rho g \ell_V^2}{\gamma_v \ell} = \sqrt{Bo_x^2 + Bo_z^2}. \tag{5.10}$$

We can thus express our parameter space either via (Bo_x, Bo_z) or via (Bo, α).

5.3 Numerical details

To minimise equations 5.2 and 5.7 under the unit volume constraint, we have used Surface evolver [26, 27], which is a free energy minimisation software, which represents interfaces through a triangular mesh and locally moves triangle vortices in the energy descent direction. We initialise the cube with the unit volume and position it such that the one side of the cube lies in the plane $\tilde{x} = 0$, while the rest of the cube is above the lyophilic part $\tilde{x} > 0$. Initially, we let Surface evolver minimise the energy functional without gravity terms for a few times to relax the initial shape, which leads to a spherical cap like shape where the contact line is positioned partially on the lyophilic part of the substrate $\tilde{x} > 0$ and partially on the chemical step. Afterwards, we include the body force to the droplet and let the system equilibrate. To detect stable shapes, we repeat series of energy minimisations, followed up with refinement of the mesh, until the difference in energy between two cycles becomes less than 0.005%. When convergence reaches the target value, we check the stability of the solution by introducing stochastic noise along the interface and

letting the process repeat itself. Using the above described algorithm, we have determined threshold values of Bond numbers Bo_t for which stable solutions are still obtainable with the bisection method. Throughout the calculation, refinement of the triangular mesh is done in the way that we introduce the dimensionless length scale ℓ_{mesh} and split edges whose length is longer than ℓ_{mesh}, while we delete all the edges smaller than $0.4\ell_{mesh}$. In all calculations, we keep the value of ℓ_{mesh} set to 0.1.

5.4 Results

We will firstly explore properties of stable droplet shapes when the normal gravity component g_z is neglected. In Figure 5.2 we show examples of such shapes for the respective values of Young' angle set to $\theta_u = 60°$ and $\theta_d = 120°$, since we can describe what is qualitatively happening with the droplet shape once we start increasing Bo_x. For $Bo_x = 0$, the droplet will form a spherical cap in the region $\tilde{x} > 0$ with the contact angle θ_u. Once we introduce the tangential body force to the system, part of the contact line moves to the chemical step and the local contact angle on the chemical step ranges from θ_u to θ_d. As visible in Figures 5.2 *a* and *b*, for small Bond numbers, the front part of the contact line is positioned on the chemical step and as we increase the Bond number, the droplet is more strongly pushed towards the lyophobic side. Eventually, part of the contact line will leave the chemical step and start to spread on the lyophobic area with the constant contact angle θ_d, while the remaining part of the contact line still remains on the chemical step, as visible in Figure 5.2.c. This behaviour of the contact line and the contact angle is completely analogues to the droplet wetting of a single chemical pattern, without the body force applied to the droplet [9–13]. This behaviour is very different from CLFM calculations, since the contact line will not cancel out the body force applied to the droplet itself [22], but rather the stable shapes are realised via self-deformation where the mechanical equilibria of the contact line and the interface are satisfied.

In Figure 5.2.d we show the stable morphology very close to the threshold Bond number Bo_t, which is the largest Bond number for which the equilibrium shape is observed. For the given value of Young's angles ($\theta_u = 60°$ and $\theta_d = 120°$) the threshold Bond number is $Bo_t = 1.735$. A numerical problem which arises around the threshold Bond number is that the part of the contact line which is positioned on the chemical step becomes so small, that the droplet morphology cannot realise the transition from the value of the local contact angle θ_u to θ_d along that part of the contact line. Therefore the stable smooth morphology, which satisfies the mechanical equilibria expressed via

Young's angle (Eq. 5.3) and the Young-Laplace equation (Eq. 5.5), cannot be obtained. For the values very close to the threshold Bond number Bo_t, Surface Evolver cannot resolve the smooth transition of the contact angle along the chemical step. However, if we apply a small transitional shift to the droplet morphology towards negative x-direction, the whole morphology retreats back to its original shape, meaning that the local energy minimum is present, but the transition is below the length scale of our mesh.

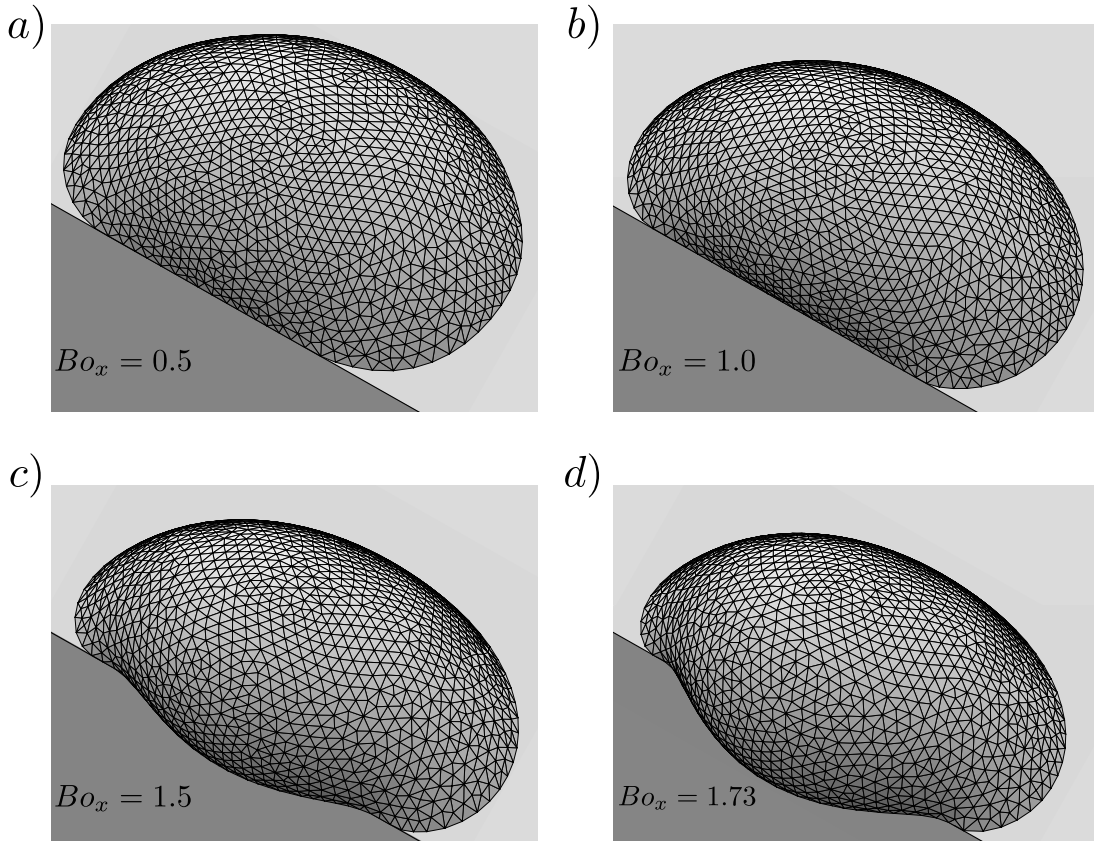

Figure 5.2: Series of shapes for Young's angles values of $\theta_d = 120°$ and $\theta_u = 60°$, for different values of Bond numbers. Threshold Bond number is $Bo_t = 1.735$ for given values of Young's angles. The camera position is same in every image, but as visible droplets can migrate a little in the direction perpendicular to $x - z$ plane, since energetically this does not change the energy value

The above described contact line behaviour towards the threshold equilibrium shape is not the same once the value of θ_u becomes relatively small compared to the value of θ_d. In Figure 5.3 we show the threshold shape for a system of values $\theta_d = 120°$ and $\theta_u = 10°$. We see that the contact line length on the chemical step is still substantial. However, once we observe the droplet shape from a side view, we see that the droplet cross section has an inflection point and that the value of the curvature on the back end of the droplet has a negative value. If we would increase Bond number a bit, part of

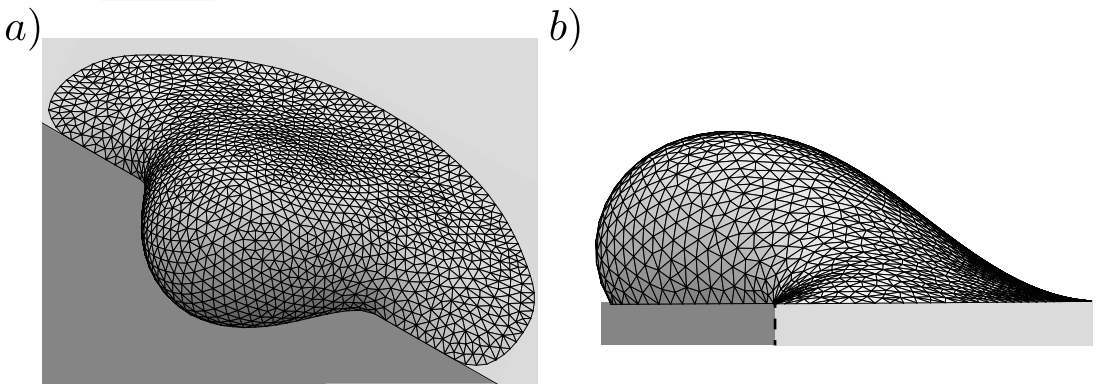

Figure 5.3: Threshold shape for Young's angles values of $\theta_d = 120^\circ$ and $\theta_u = 10^\circ$ for a value of the threshold Bond number value $Bo_t = 3.232$ from a tilted view (a) and side view in which the striped line is $x = 0$ (b)

the triangulation mesh would sink below the substrate ($z < 0$) and the whole morphology diverges to a nonphysical shape. This indicates that geometrical conditions which arise from solving Young-Laplace equations is an additional limiting factor in obtaining stable shapes. In Figure 5.4.a we show values of the threshold Bond number Bo_t (beyond which stable equilibria are no longer possible) as a function of the equilibrium contact angles θ_u and θ_d. The general rule for the threshold Bond number Bo_t is that it increases with increasing difference in wettability, but the threshold Bond number is not only a function of $\theta_d - \theta_u$, since as we show on the threshold equilibrium shape in Figure 5.3, the droplet interface curvature also plays a role. For the case of $\theta_d = \theta_u$ there is no stable equilibrium shape, since the functional represents the case of a tilted homogeneous substrate, where the energy minimum cannot be obtained due to the gravity terms present in our energy functionals, which are functions of position.

In the case of neglecting the normal gravity component in the energy functional, we can analytically calculate a relation between the size of the droplet and the maximum slope of the substrate α_{max}. Let us revisit the definition of Bo_x, which has to be smaller than Bo_t. After some rearranging, we can write

$$\sin\alpha < \frac{Bo_t \ell_c^2}{\ell_V^2} \tag{5.11}$$

where $\ell_c \equiv \sqrt{\gamma_{v\ell}/\rho g}$ is the capillary length determined by the total value of the gravity acceleration g. For the case when $\ell_V < \sqrt{Bo_t}\ell_c$, the droplet has the stable shapes for any given substrate slope α, but in the case of $\ell_V > \sqrt{Bo_t}\ell_c$, the fraction on the right hand side of the Eq. 5.11 has the value smaller than one. Therefore, there is a maximum substrate slope α_{max}, as shown in Figure 5.4.b. We can write the solution of Eq. 5.11 as

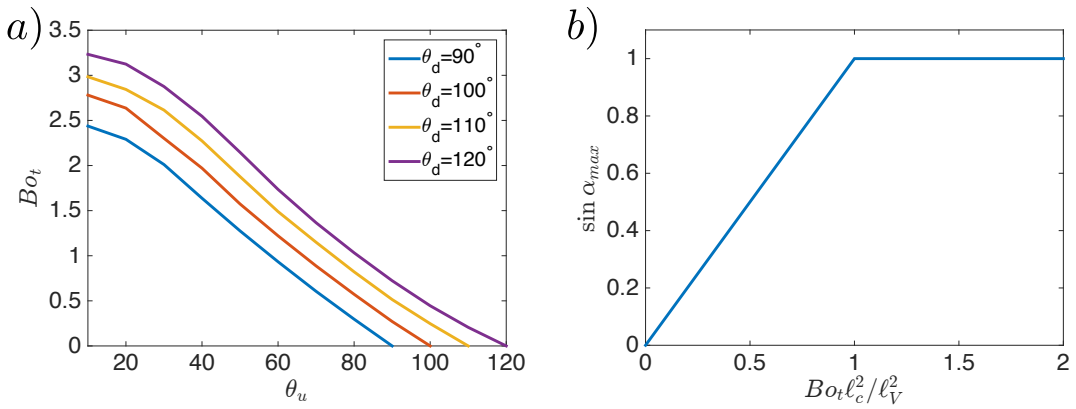

Figure 5.4: *a)* Threshold values Bo_t as a function of both Young's angles θ_u and θ_d. Once we obtain those values, we completely describe the range of the substrate slope α as a function of the size of the droplet in *b)*, where ℓ_V denotes the volume length scale.

$$\sin\alpha_{max} = \begin{cases} 1, \text{ if } \ell_V < \sqrt{Bo_t}\ell_c \\ \frac{Bo_t\ell_c^2}{\ell_V^2}, \text{ if } \ell_V > \sqrt{Bo_t}\ell_c \end{cases} \tag{5.12}$$

With the result shown in Figure 5.4, we have completely solved the problem of threshold values for the case of the energy functional expressed in Eq. 5.2, for both the droplet size and the substrate slope.

From now on, we are going to include the effect of the normal gravity component g_z. Since we are now introducing one more parameter (either Bo_z or α) to our analysis, we will limit our attention to cases with the fixed value of the lyophobic Young's angle $\theta_d = 90°$, while we will still change the value of the lyophilic Young's angle $10° \leq \theta_u \leq 90°$, where the case of $\alpha = 90°$ was already previously calculated and summarised in Figure 5.4.a. In Figure 5.5.a we show what happens with the contact line for the unit volume droplet, once we fix the value of $Bo_x = 1.5$ and change the value of Bo_z, for the lyophilic Young's angle $\theta_u = 40°$. Intuitively, one would expect for the increasing value of Bo_z that the droplet shape is going to be more spread and flat, but what we observe is that in this given system, the droplet contact line is retreating from the lyophobic part to the chemical step and the contact area with the lyophilic part increases. To observe threshold equilibrium shapes, once the full gravity effect is included, we define $Bo_t^\star$ as a threshold value of the total Bond number Bo and in the Figure 5.5.b we show the value of $Bo_t^\star$ as a function of the substrate slope α and the lyophilic Young's angle θ_u. For the substrate slope value of $\alpha = 90°$ we just use the previously calculated threshold values of Bo_t. Once the difference between Young's angles becomes substantial, we observe that values of $Bo_t^\star$ go above ten. For the case of $\alpha = 0°$, the value of the threshold total Bond number $Bo_t^\star$ diverges as they should, since the

equilibrium shape is a pancake-like morphology on the lyophilic part of the substrate. For almost perfectly wettable substrates and the small substrate slope, droplets have equilibrium wetting shapes even with the volume length scale way bigger than the capillary length scale. As stated in the introduction, the CLFM calculation was verified for values of the Bond number ranging between 1.0 and 1.6, while for larger Bond numbers the threshold values of phase transition are deviating from the experimental data.[23] In Figure 5.5.c we show the difference between the tangential component of the threshold total Bond number $Bo_t^\star$ and the threshold Bond number Bo_t obtained for the case of omission of the normal gravity component. It is immediately clear that with the increasing value of the normal gravity component, the threshold tangential gravity component also becomes larger, due to the contact line effect explained in Figure 5.5.a. Observation of this result might indicate that instead of deviation from the experimental data being a CLFM flaw, it might be an experimental measurement error. By ignoring the normal gravity component, we immediately underestimate the Bond number values, since it is immediately clear that an interaction of the normal gravity component with the droplet changes the landscape of equilibrium shapes. Larger droplets can also deform to the mechanical equilibrium, since the droplet tends to retreat to the lyophilic part of the substrate with the increasing normal gravity component. The driving mechanism for the existence of the threshold volume is the same as in the case of neglecting the normal gravity component. For small differences in values of Young's angle, it is the Young's law itself which cannot be satisfied smoothly, while for the case of large differences, we still run into the problem of a droplet having the tendency to go "beneath" the substrate, i.e., to nonphysical solutions.

5.5 Conclusions

Equilibrium shapes of the sliding droplet on the substrate patterned with chemical steps are obtained using Surface evolver. For the case of nano/micro droplets we calculate the threshold volume for which the droplet will not be able to be at the chemical step and we analytically connect this result to the maximum substrate slope for which the stable shapes can still be observed. Once we introduce the full response of the droplet to gravity, we observe that for the same value of the gravitation tangential component, the larger normal tangential component helps the droplet to retreat to the lyophilic part of the substrate. Qualitatively, we show that in the case of large difference between Young's angle, it is Young-Laplace equation which causes the existence of the threshold droplet volume for which the stable shapes can be observed, while

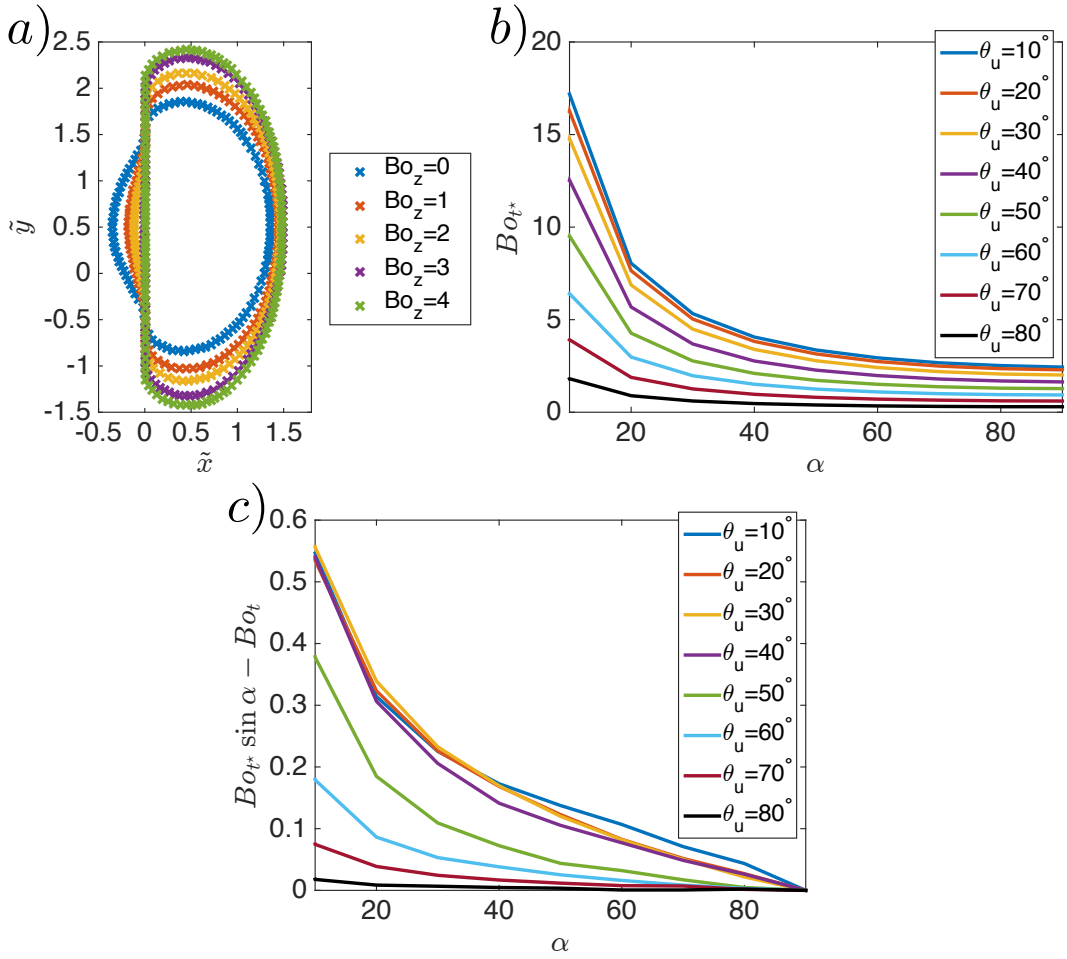

Figure 5.5: *a)* Contact line position of stable droplet shapes for a fixed value of Bo_x and for the increasing Bo_z. $\tilde{y}$ denotes the spatial coordinate along the chemical step, but the energy functionals expressed in Eqs. 5.2 and 5.7 do not depend on it. *b)* Threshold values $Bo_t^\star$ of the total Bond number Bo for which the droplet can still obtain an equilibrium shape. *c)* Increase in the threshold value of the tangential gravity component, once the normal gravity component interaction with the droplet is included.

in the case of a small difference in wetability, we identify that the mechanical equilibrium of the contact line cannot be satisfied without singularities present in the same contact line.

References

[1] R. J. Good. Contact angle, wetting and adhesion: a critical review. *J. Adhesion Sci. Technol.*, 6:1269–1302, 1992.

[2] P. G. de Gennes, F. Brochard-Wyart, and D. Quere. *Capillarity and wetting phenomena: drops and bubbles and pearls and waves.* Springer, New York, 2004.

[3] P. G. de Gennes. Wetting: statics and dynamics. *Rev. Mod. Phys.*, 57:827,

1985.

[4] S. Herminghaus, M. Brinkmann, and R. Seemann. Wetting and dewetting of complex surface geometries. *Annu. Rev. Mater. Res.*, 38:101–121, 2008.

[5] D. Soltman, B. Smith, H. Kang, S. J. S. Morris, and V. Subramanian. Methodology for inkjet printing of partially wetting films. *Langmuir*, 26:15686–15693, 2010.

[6] T. Lee, E. Charrault, and C. Neto. Interfacial slip on rough, patterned and soft surfaces: A review of experiments and simulations. *Adv. Colloid Interface Sci.*, 210:21–38, 2014.

[7] B. S. Clausen, J. Schiøtz, L. Gråbæk, C. V. Ovesen, K. W. Jacobsen, J. K. Nørskov, and H. Topsøe. Wetting/ non-wetting phenomena during catalysis: Evidence from in situ on-line exafs studies of cu-based catalysts. *Top. Catal.*, 1:367–376, 1994.

[8] H. Hu, J. Wen, L. Bao, L. Jia, D. Song, B. Song, G. Pan, M. Scaraggi, D. Dini, Q. Xue, and F. Zhou. Significant and stable drag reduction with air rings confined by alternated superhydrophobic and hydrophilic strips. *Sci. Adv.*, 3:e1603288, 2017.

[9] I. Dević, G. Soligno, M. Dijkstra, R. van Roij, X. Zhang, and D. Lohse. Sessile nanodroplet on elliptical patches of enhanced lyophilicity. *Langmuir*, 33:2744–2749, 2017.

[10] M. Brinkmann and R. Lipowsky. Wetting morphologies on substrates with striped surface domains. *J. Appl. Phys.*, 92:4296–4306, 2002.

[11] A. A. Darhuber, S. M. Troian, and S. Wagner. Morphology of liquid microstructures on chemically patterned surfaces. *J. Appl. Phys.*, 87:7768–7775, 2000.

[12] C. W. Extrand. Contact angles and hysteresis on surfaces with chemically heterogeneous islands. *Langmuir*, 19:3793–3796, 2003.

[13] P. Lenz and R. Lipowsky. Morphological transitions of wetting layers on structured surfaces. *Phys. Rev. Lett.*, 90:1920–1923, 1998.

[14] S. Brandon, N. Haimovich, E. Yeger, and A. Marmur. Partial wetting of chemically patterned surfaces: The effect of drop size. *J. Colloid Interface Sci.*, 263:237–243, 2003.

[15] Lichao Gao and Thomas J. McCarthy. How wenzel and cassie were wrong. *Langmuir*, 23:3762–3765, 2007.

[16] G McHale. Cassie and wenzel: Were they really so wrong? *Langmuir*, 23:8200–8205, 2007.

[17] H. Matsui, Y. Noda, and T. Hasegawa. Hybrid energy-minimization simulation of equilibrium droplet shapes on hydrophilic/hydrophobic patterned surfaces. *Langmuir*, 28:15450–15453, 2012.

[18] G. Soligno, M. Dijkstra, and R. van Roij. The equilibrium shape of fluid-

fluid interfaces: Derivation and a new numerical method for young?s and young-laplace equations. *J. Chem. Phys.*, 141:244702, 2014.

[19] C. T. Nguyen, M. Barisik, and B. Kim. Wetting of chemically heterogeneous striped surfaces: Molecular dynamics simulations. *AIP Advances*, 8:065003, 2018.

[20] S. Varagnolo, V. Schiocchet, D. Ferraro, M. Pierno, G. Mistura, M. Sbragaglia, A. Gupta, and G. Amati. Tuning drop motion by chemical patterning of surfaces. *Langmuir*, 30:2401–2409, 2014.

[21] S. Varagnolo, D. Ferraro, P. Fantinel, M. Pierno, G. Mistura, G. Amati, L. Biferale, and M. Sbragaglia. Stick-slip sliding of water drops on chemically heterogeneous surfaces. *Phys. Rev. Letter.*, 111:066101, 2013.

[22] C. Semprebon and M. Brinkmann. On the onset of motion of sliding drops. *Soft Matter*, 10:3325–3334, 2014.

[23] C. Semprebon, S. Varagnolo, D. Fillipi, L. Perlini, M. Pierno, M. Brinkmann, and G. Mistura. Deviation of sliding drops at a chemical step. *Soft Matter*, 12:8268–8272, 2016.

[24] M. Sbragaglia, L. Biferale, G. Amati, S. Varagnolo, D. Ferraro, G. Mistura, and M. Pierno. Sliding drops across alternating hydrophobic and hydrophilic stripes. *Phys. Rev. E*, 89:012406, 2014.

[25] M. J. Santos, S. Velasco, and J. A. White. Simulation analysis of contact angles and retention forces of liquid drops on inclined surfaces. *Langmuir*, 28:11819–11826, 2012.

[26] K. A. Brakke. The surface evolver. *Exp. Math.*, 1:141–165, 1992.

[27] Surface evolver manual, version 2.70, 2013.

6

Solid-state dewetting on grooved substrate

Once we heat a solid to the sub-melting regime, the capillary interaction between the solid interface and surrounding phase starts the atom surface diffusion along the same interface. The common name for this process is solid-state dewetting. The contact line behaviour during the solid-state dewetting has been analysed numerically for homogenous substrates, but an open fundamental question is how does the contact line behave, once we introduce patterning to our system. In the present work, we have investigated influence of the physical inhomogeneity on the contact line, mainly, how long does contact line pinning last and how does the global dynamics get affected. To answer these questions, we developed marker code for the solid-state dewetting on the grooved substrate for which the solid and the substrate length scales are of a similar order. We identify two different ways of convergence to the equilibrium shape and depending on the scenario, the contact line will either remain pinned in the inhomegeneity or it will unpin itself very quickly. We also provide estimation for the material constant of the copper, but the precision of the estimate is up to factor of three, due to imperfections in experiments such as fingering instabilities and groove boundaries.

6.1 Introduction

When a solid film is deposited on a substrate and exposed to a sub-melting temperature environment, the solid interface becomes capillary unstable and a surface diffusion process of atoms starts deforming the solid. If the substrate has a relatively high melting temperature and remains stable, the solid film will start to dewet that same substrate, with a developed three-phase contact line similar to ones observed on sessile droplets. Solid-state dewetting is the phenomenon which has many industrial applications such as catalysis and nanopatterning [1, 2]. From a scientific point of view, many fundamental questions still remain unanswered, although the phenomenon is known for longer than half of century [3]. Solid-state dewetting poses a two-way problem, since it may start an unwanted deformation in many nanosystems, but it might be used to produce desired solid nanopatterns.

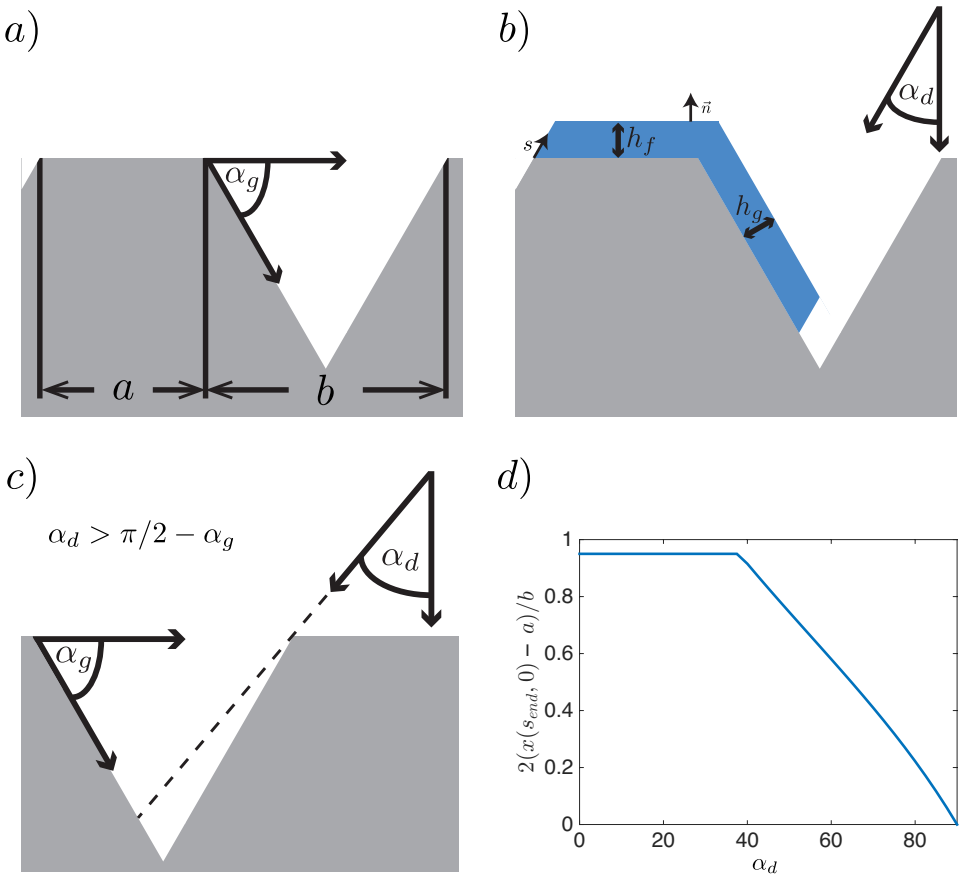

Figure 6.1: *a)* Geometrical definitions of variables describing the substrate. *b)* Initial state of the solid film deposited under the angle α_d. *c)* Visual representation of the "shadow" principle, which determines $x(s_{end},0)$. *d)* On y axis, we show the area fraction initially covered by the solid film on the left side of the groove.

Solid-state dewetting also has many similarities [4–6] to thin liquid film

dynamics [7], which can be adressed with general liquid wetting theory [8–10]. However, the driving dewetting mechanism differs a lot. In the case of wetting/dewetting liquid systems, one has to solve Navier-Stokes equation with proper boundary conditions, while the solid-state dewetting is completely governed by surface diffusion, once the temperature of the system is sufficiently high to make the solid interfacial layer sensible to the capillary interactions, but the temperature must still not be so high that the whole solid melts. Even though different mechanisms drive dewetting processes in liquid and isotropic solid systems (weak crystallography effects), an additional striking similarity is that the final equilibrium shapes belong to the same family of shapes; namely they are solutions to the Young-Laplace equation, which implies a constant curvature equilibrium shape along with the equilibrium contact angle, more commonly known as the Young's angle.

Solid-state dewetting on the patterned substrate was experimentally studied by many authors [2, 11–15], while the numerical research was concentrated on smooth curved substrates [16]. Since the Young's angle and the constant curvature shape are direct result of minimising the interfacial energy of the system, we will use the same argumentation in providing boundary condition for the inhomogeneity on the physically patterned substrate, which for liquids was studied on both chemical [17, 18] and physical [9] patterns. In previous work of some of the authors, van den Beld et al. [15] performed the experiment of the copper dewetting on a grooved silicone substrate (Figure 6.1.a), where the contact line pinning was observed at the groove edge. In the present work, we will explore given geometries with the two dimensional numerical scheme.

The grooved substrate and all of parameters are introduced in Figure 6.1.a, along with the properties of the initial state of the solid film. The grooved substrate consists of a flat part which has width a and the groove which is characterised by the width b. To completely define the system geometry, we need the value of the groove angle α_g. We use the same properties of the substrate as van den Beld et al. [15]; namely, we will fix the value of the groove angle to 54.7° and we will set the ratio between b and a to 2.5. With these restrictions, the only control parameter for the substrate geometry is the length scale a (Figure 6.1.a). In the experimental study, the copper thin film was deposited on the substrate by the e-beam evaporation under different angles, resulting in different initial profiles of the copper film over the flat substrate and the left groove wall (Figure 6.1.b). If we deposit a film of height H (the length scale with which we normalise spatial and time coordinates) under the deposition angle α_d, the deposited film has two different dimensionless heights: the film height above the flat part of the substrate $h_f = \cos\alpha_d$ and the film height above the groove $h_g = \cos(\alpha_d - \alpha_g)$. To determine how much

of the groove is covered by the solid film initially, we define two conditions. If $\alpha_d < (90^\circ - \alpha_g)$, we set that 95 percent of the groove wall is covered by the solid film, so that we do not have to deal with the presence of the right groove wall in the initial stages of the dynamics, since in experiments, the left groove wall was never fully covered initially [15]. However, if $\alpha_d > (90^\circ - \alpha_g)$, we have to determine using the "shadow principle" (Figure 6.1.c), with which we predict the position of the contact line by calculating how much area of the left groove wall was not exposed to the e-beam evaporation in experiments [15]. In Figure 6.1.d we show the area fraction of the left groove wall which is initially covered by the solid film. For the left side of the solid film, we always initially set the contact line in the left groove edge point. To summarise, with the width of the flat part of the grooved substrate a we define the substrate geometry, while with the deposition angle α_d, we define the initial shape of the solid film.

For isotropic solids (surface tension is constant on the solid interface), the chemical potential is linearly proportional to the curvature [19] and the solid-state dewetting is governed by[3]

$$\tilde{u} = B\tilde{\nabla}_s^2\tilde{K} \tag{6.1}$$

where $\tilde{u}$ is the interface velocity in the direction of the interface normal vector $\vec{n}$ (Figure 6.1), $\tilde{K}$ is the interface curvature, while the material constant B is defined as $B = \gamma D\nu\Omega^2/k_BT$, where γ is the solid surface tension with the outer phase, D is the surface diffusivity, ν is number of moving atoms per unit area in the interfacial layer, Ω is the atomic volume, k_B is the Boltzmann constant and T is the temperature of the system. To make Eq. 6.1 dimensionless, we will normalise all spatial coordinates with the solid film height H, while we will normalise time with H^4/B. The resulting dimensionless equation is

$$u = \nabla_s^2 K \tag{6.2}$$

where u is the dimensionless interface velocity and K is the dimensionless curvature. The dimensionless equation reveals an interesting property about the material constant B. While it affects how fast the solid-state dewetting happens, it does not play any role on temporary morphological states of the solid film.

Let us describe the film interface with functions $x(s,t)$ and $y(s,t)$, where s is the dimensionless arc length parameter (Figure 6.1.b) and t is the dimensionless time variable, while x and y are spatial coordinates in the dimensionless space. We set the origin of the (x,y) coordinate system in the left groove edge point $(x(0,0) = 0)$. Additionally, we define the arc length parameter to start

from the left contact line ($s = 0$), to the right contact line ($s = s_{end}$). Firstly, we need to set the contact line on the substrate, hence we impose:

$$y(0,t) = \begin{cases} 0, & \text{if } 0 < x(0,t) \leq a \\ (a - x(0,t)) \tan \alpha_g, & \text{if } a < x(0,t) < a + b \end{cases} \tag{6.3}$$

In the same fashion, we define the boundary condition for the position of the contact line on the right side of the film

$$y(s_{end},t) = \begin{cases} 0, & \text{if } 0 < x(s_{end},t) \leq a \\ (a - x(s_{end},t)) \tan \alpha_g, & \text{if } a < x(s_{end},t) < a + b \end{cases} \tag{6.4}$$

On both ends of the film, we set the zero-flux boundary condition

$$\left.\frac{\partial K}{\partial s}\right|_{s=0} = \left.\frac{\partial K}{\partial s}\right|_{s=s_{end}} = 0 \tag{6.5}$$

which is a sufficient condition to impose mass conservation on the solid film.

To mathematically close the problem, we need one more condition, which is the contact angle boundary condition. The equilibrium contact angle for the solid film during the solid-state dewetting process is Young's angle, which is uniquely defined by three separate surface tensions present at the contact line. If we denote Young's angle with θ_Y, we can define the contact angle boundary conditions for the left side of the solid film;

$$\left.\frac{\partial y(s,t)}{\partial x(s,t)}\right|_{(s=0)} = \begin{cases} \tan \theta_Y, & \text{if } 0 < x(0,t) < a \\ \tan(\theta_Y - \alpha_g), & \text{if } a < x(0,t) < a + b \end{cases} \tag{6.6}$$

while for the right side of the solid film, the contact angle boundary condition is

$$\left.\frac{\partial y(s,t)}{\partial x(s,t)}\right|_{(s=s_{end})} = \begin{cases} -\tan \theta_Y, & \text{if } 0 < x(s_{end},t) < a \\ -\tan(\theta_Y - \alpha_g), & \text{if } a < x(s_{end},t) < a + b \end{cases} \tag{6.7}$$

However, there is a specific boundary condition we have to define for the groove edge ($x = a$). Since the contact angle boundary condition is completely analogous to the liquid wetting theory, we are going to implement the scheme of that theory in handling contact line dynamics on the groove edge. We will explain this boundary condition for the left contact line, once it arrives to the groove edge point $x = a$,. Once the contact line reaches $x(0,t) = a$, it will have the Young's contact angle, but if we calculate next time step of

the dynamics (Eq. 6.2), we are facing a situation where we cannot satisfy the boundary conditions represented in Eqs. 6.3 and 6.6 at the same time. Therefore, we will fix the position of the contact line in the groove edge point, until the film morphology rotates enough, so that the combination of boundary conditions for the left contact line can be satisfied. Let us denote the slope $\partial y(0,t)/\partial x(0,t)$ with θ. We can ten write the last boundary condition as

$$x(0,t) = a, \text{if } \theta_Y > \theta > \theta_Y - \alpha_g \; and \; x(0,t) = a \tag{6.8}$$

For the case when the left contact line is positioned in $x = 0$, we define the similar boundary condition, but we would like to note that this happens very rarely in early stages of dynamics

$$x(0,t) = 0, \text{if } \theta_Y < \theta < \theta_Y + \alpha_g \; and \; x(0,t) = 0 \tag{6.9}$$

Although we are just fixing the contact line in the edge point, this is indeed the contact angle condition which will make solid-state dewetting to behave analogues to the quasi-steady growth and shrinkage of droplets and bubbles on both physically and chemically patterned substrate [9]. Even though the solid-state dewetting is qualitatively different than the liquid dewetting, energetical argumentation for using the boundary condition expressed in Eq. 6.8 is identical to the Young's angle boundary condition, which we are imposing on homogeneous parts of the substrate (Eqs. 6.6 and 6.7).

6.2 Numerical scheme

To solve the solid-state dynamics (Eq. 6.2), we used a *marker* numerical scheme, similar to the one developed by Wong et al. [20], where we describe the solid film interface by positioning points (markers) on the interface. We evaluate the normal velocity u for each marker using Eq. 6.2 and then we perform forward time integration to calculate new positions of the markers. To evaluate the dimensionless curvature, we calculate the divergence of the normal interface vector along the solid film interface. Since the curvature is a function of x and y, which are functions of the arc length parameter and of time, we can rewrite the Laplacian present in Eq. 6.2 to obtain

$$u = \frac{\partial^2 K}{\partial s^2} \tag{6.10}$$

For calculation of the curvature and its Laplacian, we use central-difference spatial derivatives for unevenly spaced points. Although some sources claim [21] that one of the biggest flaws of *marker* methods is the need to make points equidistant at every time step, which makes needed computational power even

bigger, we do not perform this process on every time step. However, if we do not make points equidistant at all during the calculation, we will face problem of having small time steps in our calculation, which also slows down the calculation, which means that we need to balance this two effects, to optimise the code. Since Eq. 6.2 is a fourth-order partial differential equation, we have to take into consideration that our maximum time step dt will be proportional to the fourth power of the smallest distance between points on the whole interface $min(ds)$. We can express this as

$$dt = \frac{min(ds)^4}{C} \tag{6.11}$$

where C is a constant which cannot be uniquely defined for any fourth-order differential equation solving method, but depends on mathematical stability of all the numerical schemes used during the calculation [22]. We report that our finite difference scheme was stable for value of $C = 10$. We make points equidistant every 5000 time steps with the spline interpolation, since the resulting interpolation function will be continuous, not only for x and y, but also for the curvature.

To validate the present numerical scheme, we will compare our results to the groove boundary dynamics in which the analytical solutions is known [3] and for the case of the semi-infinite solid film [20] for which the contact line in later stage of dynamics asymptotically approaches scaling $x(0,t) \sim t^{\frac{2}{5}}$ as Young's angle goes to zero. For both cases the analytical solution was obtained using the small slope approximation. In Figure 6.2.a we show that the groove boundary aspect ratio (ratio of the groove boundary width w and the groove boundary depth d) is constant throughout the dynamics as predicted by Mullins [3]. In Figure 6.2.b we confirm $t^{\frac{2}{5}}$ scaling law for the contact line dynamics of the semi-infinite film.

6.3 Results

In Figure 6.3, we show the time evolution of the dimensionless interface and curvature for fixed values of the groove length scale a, the deposition angle α_d and Young's angle θ_y. What is immediately noticeable on the curvature time evolution, is that the behaviour of the system is local, which results in propagation of the curvature along the interface in a wave-like fashion. The initial details of the system become important once these propagations of curvature collide. In the given system, there are two big initial sources of these kind of wave-like behaviour of curvature values: contact angle boundary condition (Eqs. 6.6 and 6.7) and singularity points present in the initial interface

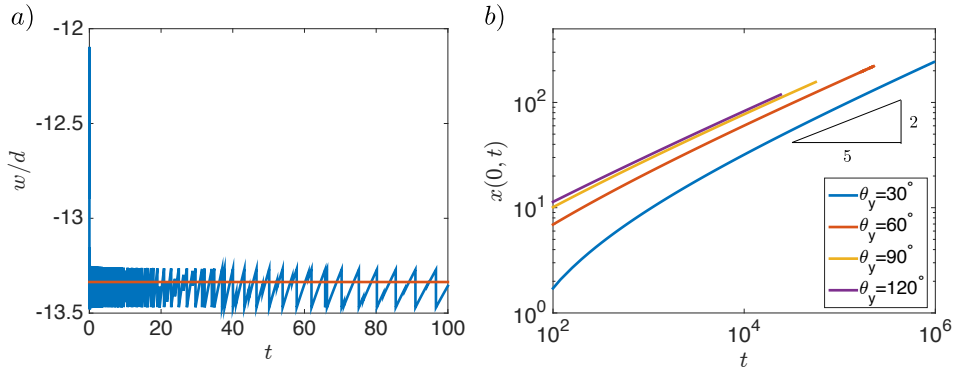

Figure 6.2: In d we show comparison of our numerical scheme to the Mullins's analytical solution for thermal grooving. Mullins predicted that the ratio of the groove width w and the groove depth d is constant throughout the grooving process. For the case of the 100° groove angle, with the red line we show Mullins's prediction [3], while with the blue line we show the value of this ratio in our numerics. The spiky nature of the blue line is due to the finite element representation of the interface and interpreting the marker with the highest value of y as the groove apex. In *b)* we validate the scaling predicted by Wong et al. [20] for the late stage solid-state dewetting of the semi-infinite film.

(points of discontinuous curvature). Dornel et al. [23] showcased that this kind of curvature interplay can cause a finite solid film on a flat homogeneous to split into isolated islands or remain compact as one body.

We are interested in exploring the phase space of variables a, θ_Y and α_d, for which the solid remains compact as one body and for which there is only one contact line. In Figure 6.4 we show qualitatively morphologies, which break up the body or create a new contact line. For the cases where the substrate length scale a and the deposition angle α_d are too small, the solid is too big to form the equilibrium shape inside the groove, so the new contact line is formed on the right groove wall, once the solid interface touches it. However, if these two parameters are way too big, then the solid interface will touch the groove edge ($x = a$) and the solid will split into two isolated solid islands. In the regime, where the solid stays as one body and doesn't form additional contact lines, we are interested how the Young's angle affects the dynamics.

The boundary condition expressed in Eq. 6.8 fixes the position of the contact line, while the interface rotates enough to satisfy contact angle boundary condition either inside or outside of the groove. Since the interface markers only move in the direction normal to the solid interface, the neighbouring marker of the one fixed in the groove edge, will move along the circular path (up to numerical error). If we denote the velocity of that marker with u_1, we can write

$$u_1 = \nabla_s^2 K(s = s_1, t) \tag{6.12}$$

where s_1 is the value of the arc length parameter of the first neighbouring

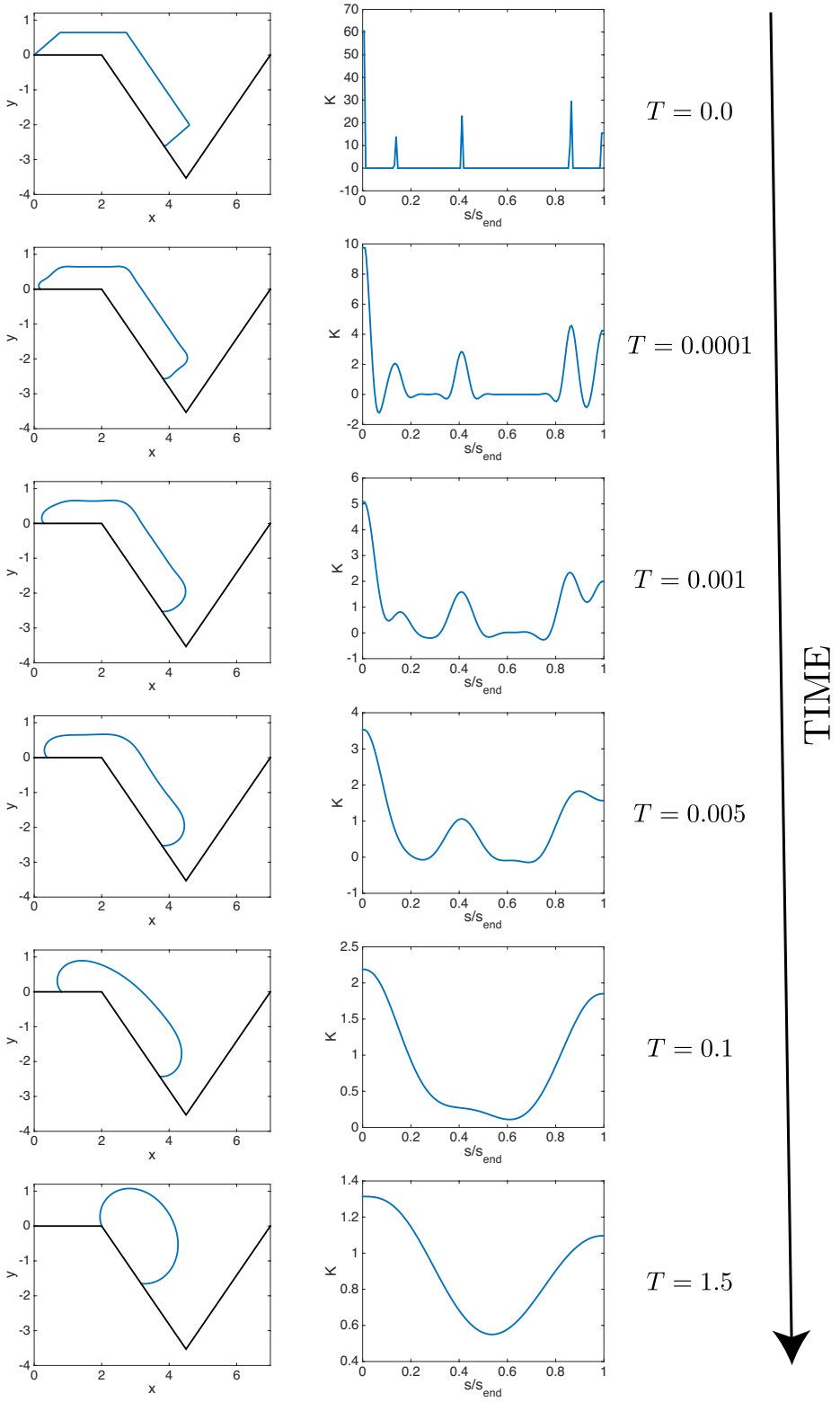

Figure 6.3: Time evolution of the interface in the dimensionless space (left column) and the evolution of the dimensionless curvature (right column). In the first row, we showcase the initial state for the values of $a = 2$, $\theta_y = 130^\circ$ and $\alpha_d = 50^\circ$. Initial singularities are quickly smoothened by the solid-state dewetting and the curvature information starts propagating along the interface.

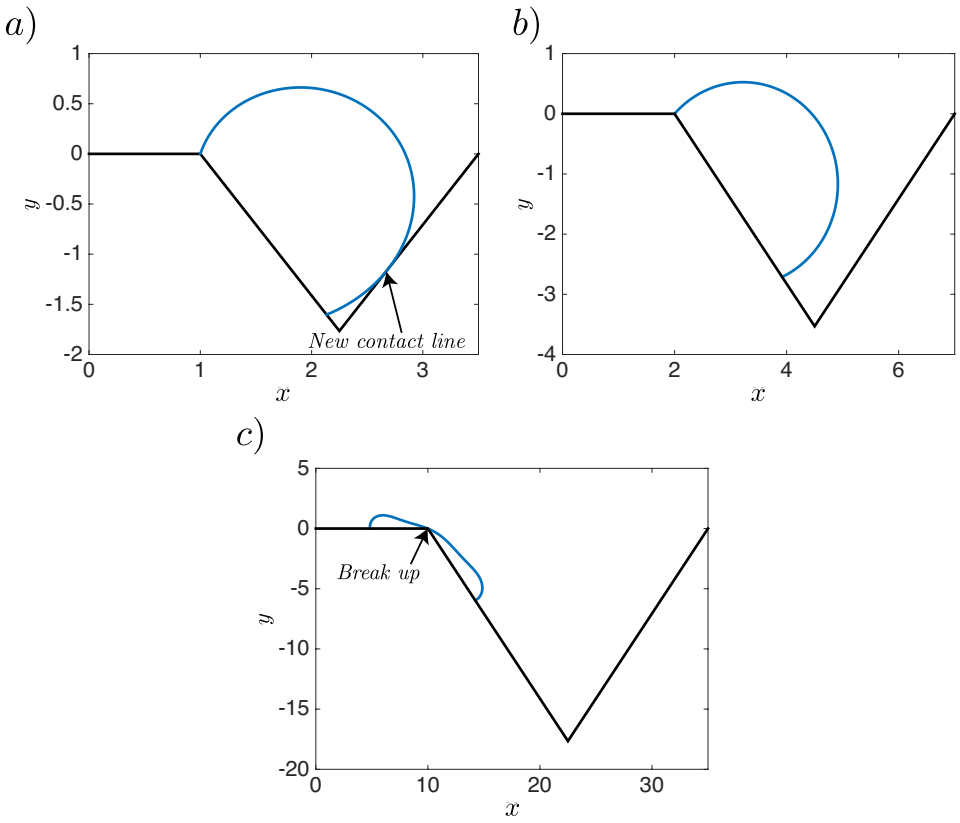

Figure 6.4: Qualitative shapes of all possible results of the solid-state dewetting. In *a)* we show the case where the new contact line is formed ($a = 1.0, \theta_Y = 100^\circ$ and $\alpha_d = 10^\circ$). The compact bodies, which are main interest of this work, form spherical caps on the left side of the groove as shown in *b)*($a = 2.0$, $\theta_y = 100^\circ$ and $\alpha_d = 10^\circ$). In the case of a large value of the substrate length scale a, such as the one shown in *c)*, the break up of the body happens at the groove edge.

marker. In terms of the contact angle, since $u_1 = s_1 \frac{\partial \theta}{\partial t}$, this equation can be expressed as

$$\frac{\partial \theta}{\partial t} = \frac{\nabla_s^2 K(s = s_1, t)}{s_1} \tag{6.13}$$

If we recall that the mass conservation boundary condition expressed in Eq. 7.5 and the local behaviour of the governing equation (Eq. 6.10), we can shed more light on the behaviour of the interface, once the left contact lines becomes pinned in the groove edge $x = a$. In discretised representation of the solid interface, second derivative of the curvature is defined via curvature values in a marker in which we are evaluating the curvature, along with curvature values in the neighbouring markers. Therefore, the velocity u_1 only depends on the curvature gradient (implicitly) between the first and second neighbouring marker of the contact line marker. However, since the curvature has the wave-like propagation along the interface, curvature gradient

informations arrives to the contact line, where due to the mass conversation boundary condition, those gradients start to diminish. With this in mind, we can state that the time evolution of the velocity u_1 depends on the curvature profile along the interface. If we look at the contact angle evolution which is explicitly expressed in Eq. 6.13, the pinning boundary condition (Eq. 6.8) starts revealing interesting properties of the solid-state dewetting dynamics, once physical inhomogeneities are present in the substrate. What this implies is that if the curvature profile is very close to obtaining constant curvature shape, there may not be enough of the curvature gradient close to the contact line to unpin from the groove edge, while if the solid still has large curvature gradients, it will unpin easily. This is observable in analysing final shapes of the dynamics, which are obtained once the difference between highest and lowest curvature value has a deviation of less than 0.5%, since the dynamics become really slow afterwards. For small values of the substrate length scale a, the equilibrium shape has the contact line pinned in the groove edge, while once we start increasing the substrate length scale, in the moment when the contact line touches the groove edge there is much more curvature gradient and the contact line unpins at the later stages of the dynamics and the contact line of the equilibrium shape will be on the left groove wall (for both left $x(s=0,t)$ and right $x(s=s_{end},t)$ contact line). If we continue increasing the substrate length scale, we will eventually finish up in the regime where the solid splits in two isolated islands (Figure 6.4.c). Although we describe this phenomenon in respect to the substrate length scale a, it is not this length scale alone which dictates pinning/unpinning scenarios. If we observe curvature profiles for the given dynamics, once the solid starts final stage of converging to the constant curvature shape, there are two scenarios how the equilibrium shape is obtained. In Figure 6.5 we show curvature profiles of two different systems, once they reach the convergence of the 1%, where we identify two different scenarios of the convergence. In the first case, which we will call two-way convergence, there is a curvature global extreme for $0 < s < s_{end}$ while the curvature value for $s = 0$ and $s = s_{end}$ are almost equal. Since the atoms migrate from higher chemical potential to lower chemical potential regions, it is visible that there are two present fluxes of atoms in the system, where both fluxes either bring atoms away from or towards to both contact lines. In second case, one-way convergence, function $K(s)$ is monotone, so the flux of atoms is directed from one contact line, either left or right, to the other contact line. This two cases affect the system as it is visible in the Figure 6.5.e, where we show t_{eq}, which is the value of dimensionless time variable t once the solid shape has converged to the constant curvature shape, as a function of substrate length scale a, where we see that there is a local maximum for any given value of the deposition

angle or the Young's angle. If we compare values of t_{eq} to the time in which contact line remains pinned t_{pin} (Figure 6.5), we notice that local maxima for both values are around the same value for the substrate length scale, meaning that the pinning itself dictates how long it will take for the solid to reach the equilibrium shape via solid-state dewetting and wether or not, the equilibrium shape will have pinned contact line. In the case of the two-way convergence, the left contact line will continue to migrate deeper down the groove, but since the solid-state dynamics slow down over time, it will take long time for the solid to become constant curvature shape, although two-way convergence is happening until the end.

Since in the experiments, the width of the system (third dimension) is much larger than the substrate length scale or the height of the initially deposited solid film, the two-dimensional approximation is appliable, but the fingering instabilities and groove boundary are observable and important in third dimension, but even if we would extend our numerical scheme to be three-dimensional, these two effects would have to be included either in the initial shape of the solid film or include them in stochastic fashion. Due to the high temperatures in which the experiment is performed, it is still not feasible to observe experimentally solid-state dynamics, but we can only analyse the initial and the final state of the solid in the experiments. Because of this limitations, we can only try to evaluate the material constant B of copper. To perform this evaluation, we will compare the position of the left contact line in the experiment, which is performed for 15 minutes, with the numerical data which has full time dynamics information stored in functions $x(0,t)$. We will measure standard deviation of the function $x(0,t)$ compared to the experimental data for the corresponding value of the substrate length scale a and we are searching for a time t_{fit} for which the standard deviation is at minimum. In Figure 6.6.f we showcase t_{fit} as a function of deposition angle values α_d used in the experiment. As we can notice, the variable t_{fit} stays in the same order of magnitude and it has tendency to decrease with the higher deposition angles α_d. For higher deposition angles, initial heights of the solid h_f and h_g are smaller compared to the substrate length scale a, so the groove boundary affects the system to a higher degree than when these heights are of similar size to the pattern substrate. In the current literature, so far there are no reports on the exact values of the material constant B, rather reported values deviate up to an order of magnitude [2, 24, 25], which is the accuracy exhibited in comparing our numerical results to the experimental data. Although the reported values are for the silicon (Si) solid-state dewetting on the silicon dioxide (SiO_2) substrate, the existing problem in precisely evaluating the material constant B is not unique for that system alone. Once we plot

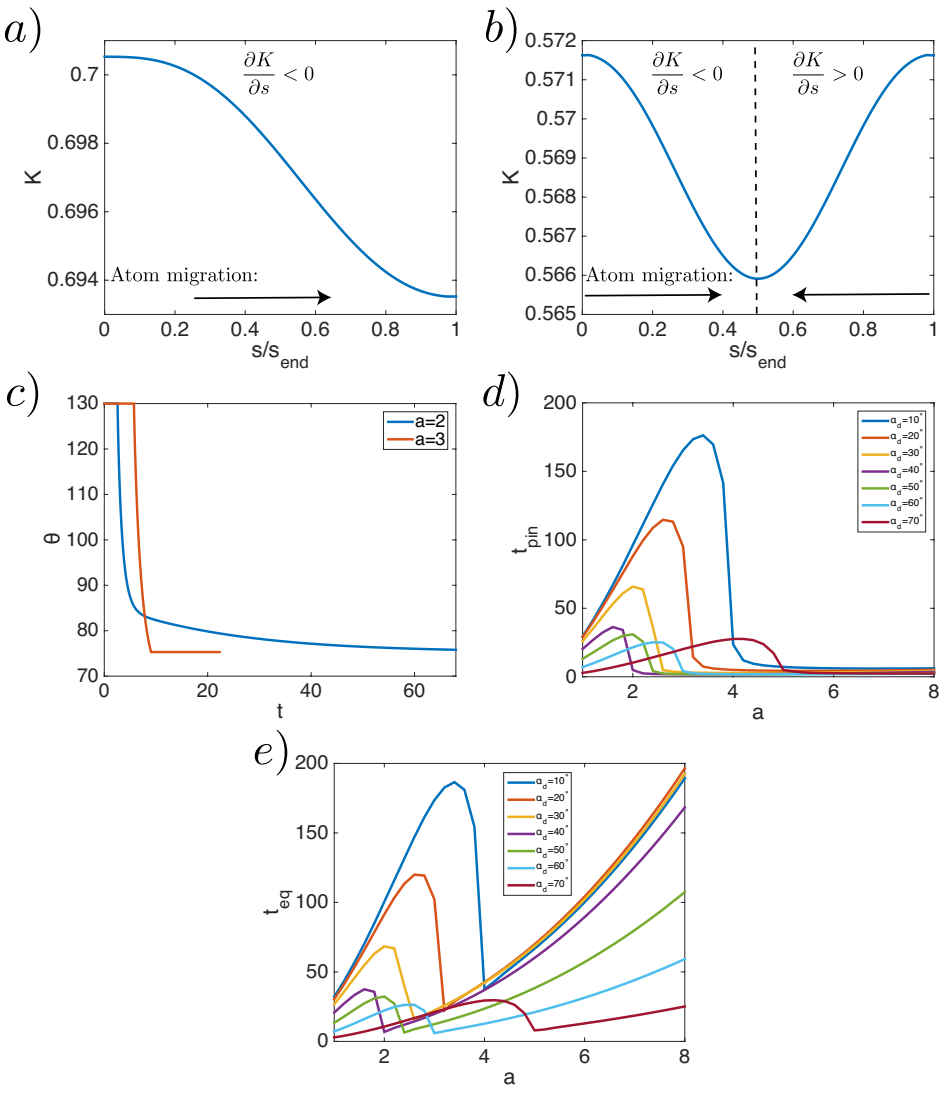

Figure 6.5: *a)* Curvature profile for the one-way convergence for the case of $a = 2$, $\theta_Y = 130°$ and $\alpha_d = 30°$, once the maximum deviatation of curvature is 1%. Atom migration of the solid in this case happens from the right to the left contact line. *b)* Curvature profile for the two-way convergence for the case of $a = 3$, $\theta_Y = 130°$ and $\alpha_d = 30°$, once the maximum deviatation of curvature is 1%. Atoms migrate away from the contact line. *c)* Time evolution for the interface slope at the contact line for cases expressed in *a* and *b* part of the figure. *d)* Pinning time of the contact line for a different values of the deposition angle α_d and the substrate length scale *a*. *e)* Time necessary for system to converge to the constant curvature shape.

$x(0, t_{fit})$ for all substrate length scales versus the experimental data, we can observe that the pinning effects are indeed stronger in the experiment than predicted by theory for smaller substrate length scales, where in numerics the unpinning scenario occurs. We do not report the comparison of the phase space in which the pinch-off happened, since the phenomenon is influenced by imperfections in the experimental setup and in the experiments, for a set val-

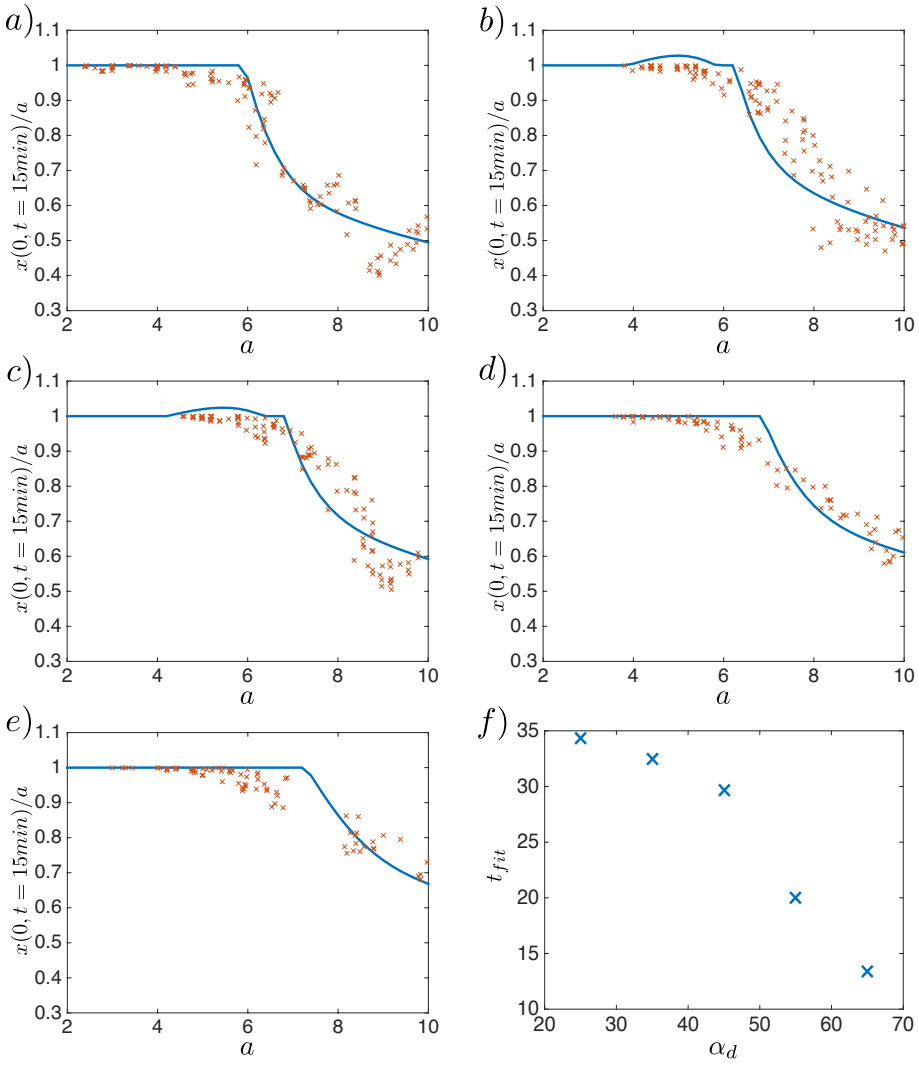

Figure 6.6: In subplots $a) - e)$ we show the comparison of the experimental data from van den Beld et al. [15] with the present numerical results. Red markers represent experimental measurements, while the solid blue line represents $x(0, t_{fit})$ for different values of the substrate length scale a. Deposition angle α_d for the subplots $a) - e)$ is respectively 25°, 35°, 45°, 55° and 65°, while the reported Young's angle is 103° [15]. We assume that dimensionless time corresponds to the dimensional time of 15 minutes and we estimate t_{fit}. In $f)$ we show estimated values of t_{fit} versus the deposition angle α_d.

ues of the deposition angle and the Young's angle, the results are not unique on the substrate with the fixed length scale a, which means there is a hysteresis effect present in the experiments. To summarise, in the regime where there is only one contact line (experiments were not performed in this regime) and the solid remains compact, we manage to obtain values of the material constant B, which deviate up to a factor of about three, while the order of the material constant is $10^{-3} \mu m^4/s$. Although there seems to be trend between the deposition angle α_d and t_{fit}, we do not intend to make any claims on the physics of it, since the source of this trend may be pure numerical.

6.4 Conclusion

In the present work, we have investigated the effect of physical inhomogeneity on the substrate and its influence on the solid-state dewetting. Since there is no migration of atoms inside the solid, but only along the interfacial layer of the same solid, qualitative difference to the liquid wetting/dewetting dynamics become even more exposed in the case of contact line pinning. We identify two different mechanisms of convergence to the constant curvature shape, which determine how fast the equilibrium shape is resolved and whether the contact line unpins itself from edges of the geometry. All of the qualitative descriptions of phase states have also been observed in the numerical results, however, the quantitive agreement is still not present, since the experiments themselves still do not give reproducible results, due to the substrate heterogeneities, fingering instabilities and groove boundary effects which might nucleate along the interface. In a regime, where the solid still remains compact with a single contact line, we show that by comparing experimental results after fifteen minutes to the numerical data, we might be able to evaluate the material constant B for a given material systems. The deviation of our estimates are of factor three, however due to the technical limitations, this improves the predictions from the literature which so far were only able to provide estimates up to the order of magnitude.

References

[1] C. V. Thompson. Solid-state dewetting of thin films. *Annu. Rev. Mater. Res.*, 42:399–434, 2012.

[2] F. Leroy, Ł . Borowik, F. Cheynis, Y. Almadori, S. Curiotto, M. Trautmann, J. C. Barbé, and P. Müller. How to control solid state dewetting: A short review. *Surf. Sci. Rep.*, 71:391–409, 2016.

[3] W. W. Mullins. Theory of thermal grooving. *J. Appl. Phys.*, 28:333–339, 1957.

[4] E. Jiran and C. V. Thompson. Capillary instabilities in thin films. *J. Electron. Mater.*, 19:1153–1160, 1990.

[5] D. J. Srolovitz and S. A. Safran. Capillary instabilities in thin films. i. energetics. *J. Appl. Phys.*, 60:247–254, 1986.

[6] D. J. Srolovitz and S. A. Safran. Capillary instabilities in thin films. ii. kinetics. *J. Appl. Phys.*, 60:255–260, 1986.

[7] R. V. Craster and O. K. Matar. Dynamics and stability of thin liquid films. *Rev. Mod. Phys.*, 81:1131–1198, 2009.

[8] P. G. de Gennes, F. Brochard-Wyart, and D. Quere. *Capillarity and*

wetting phenomena: drops and bubbles and pearls and waves. Springer, New York, 2004.

[9] David Quere. Wetting and roughness. *Annu. Rev. Mater. Res.*, 38:71–99, 2008.

[10] P. G. de Gennes. Wetting: statics and dynamics. *Rev. Mod. Phys.*, 57:827, 1985.

[11] Y. Ishikawa, Y. Imai, H. Ikeda, and M. Tabe. Pattern-induced alignment of silicon islands on buried oxide layer of silicon-on-insulator structure. *Appl. Phys. Lett.*, 83:3162–3164, 2003.

[12] Y. J. Oh, C. A. Ross, Y. S. Jung, Y. Wang, and C. V. Thompson. Cobalt nanoparticle arrays made by templated solid-state dewetting. *Small*, 5:860–865, 2009.

[13] A. L. Giermann and C. V. Thompson. Solid-state dewetting for ordered arrays of crystallographically oriented metal particles. *Appl. Phys. Lett.*, 86, 2005.

[14] J. Petersen and S. G. Mayr. Dewetting of ni and niag solid thin films and formation of nanowires on ripple patterned substrates. *J. Appl. Phys.*, 103, 2008.

[15] W. T. E. van den Beld, A. van den Berg, and J. C. T. Eijkel. Spatial control of direct chemical vapor deposition of graphene on silicon dioxide by directional copper dewetting. *RSC Adv.*, 6:89380–89386, 2016.

[16] L. Klinger and E. Rabkin. Capillary-driven motion of nanoparticls attached to curved rigid substrates. *Acta Mater.*, 60, 2012.

[17] M. Brinkmann and R. Lipowsky. Wetting morphologies on substrates with striped surface domains. *J. Appl. Phys.*, 8:4296–4306, 2002.

[18] I. Dević, G. Soligno, M. Dijkstra, R. van Roij, X. Zhang, and D. Lohse. Sessile nanodroplet on elliptical patches of enhanced lyophilicity. *Langmuir*, 33:2744–2749, 2017.

[19] C. A. Johnson. Generalization of the gibbs-thomson equation. *Surf. Sci.*, 3:429–444, 1965.

[20] H. Wong, P. W. Voorhees, M. J. Miksis, and S. H. Davis. Periodic mass shedding of a retracting solid film step. *Acta Mater.*, 48:1719–1728, 2000.

[21] W. Jiang, W. Bao, C. V. Thompson, and D. J. Srolovitz. Phase field approach for simulating solid-state dewetting problems. *Acta Mater.*, 60:5578–5592, 2012.

[22] A. K. Kassam and L. N. Trefethen. Fourth-order time-stepping for stiff pdes. *SIAM J. Sci. Comput.*, 26:1214–1233, 2005.

[23] E. Dornel, J. C. Barbé, F. de Crécy, and G. Lacolle. Surface diffusion dewetting of thin solid films: Numerical method and application to si/sio$_2$. *Phys. Rev. B*, 73, 2006.

[24] K. Sudoh, H. Iwasaki, H. Kuribayashi, R. Hiruta, and R. Shimizu. Numerical study on shape transformation of silicon trenches by high-temperature hydrogen annealing. *Jpn. J. Appl. Phys.*, 43:5937–5941, 2004.

[25] E. Dornel. *Évolution morphogique par diffusion de surface et application à l'étude du démouillage de films minces solides.* PhD thesis, Université Joseph-Fourier, Grenoble, 2007.

7

Solid-state dewetting on chemically patterned surfaces

While solid-state dewetting has recently been investigated numerically and experimentally, the direct effect of the substrate on the dewetting dynamics is still not completely clear. To shine light on this effect, we investigate solid-state dewetting on chemically patterned substrate, namely on patterns with lines. Such a substrate introduces new contact line dynamics and complicates the phase space of equilibrium shapes, not only due to the existence of multiple energy minima under the volume constraint, but also because of limitations in phase space where the same equilibrium shapes can be formed on aforementioned substrate. We directly compare the static solutions of the Young-Laplace equation to the dynamics equilibrium solutions of the solid-state dewetting, which reveals that the solid-state dewetting selection between energetically possible equilbrium shapes, is not driven by the value of the interfacial energy, but rather purely by contact line dynamics.

7.1 Introduction

If a thin solid film is deposited on a substrate and the system is heated to a sufficient temperature, the solid film can become unstable. Due to capillary interactions, the solid will minimise its interfacial energy by diffusing atoms via surface diffusion. The described process is called the solid-state dewetting and up to date, many fundamental aspects of it remain unanswered, although there are many industrial applications in which the precise control of the process would enhance many systems.[1, 2] The capillary interaction along the interface also results in the existence of a three-phase contact line and, just as in the case of liquids [3–5], the equilibrium contact angle is formed according to the surface tensions of all three phases. Although there is no detailed experimental study of the contact line dynamics in the literature, since it is hard to perform accurate measurements in the high temperature environment, phenomenological experimental observations indicate that the global dynamics is in many way driven by the local contact line behaviour. Some of the indicators are the pinning effects which arise in solid-state dewetting [6], along with the observations of hole formation and dewetting fronts inside those holes [7–9], which are qualitatively similar to the outer contact line in solid films. In our recent work [10], we showed that contact line pinning at a geometric singularity causes the solid to locally rotate around the pinning singularity, which eventually leads to the existence of two types of convergences to the final equilibrium shapes: the atoms travel from one side of the solid film to the other or they migrate from both contact lines to the solid film centre. The obvious follow-up question is: What is the influence, on the of the other liquid-like contact line behaviours on the macroscopic dynamical properties.

To analyse a related scenario of solid-state dewetting, in this paper we focus on a chemically patterned surface. To our knowledge, there is not yet a single experimental study of such a system. In their recent review, Leroy et al. [2] summarised all combinations of film/substrate which were used and they indicate that there are only three systems which can be considered a model one, out of which silicon-on-insulator (SOI) systems are known due to the lack of grain boundary effects in those systems[11], while setups of Ni/MgO[12, 13] and Ni/Al_2O_3[14] have been recognised as such in the recent years. The presence of only three combinations of material which can be studied experimentally as model system may explain why there are no studies yet with chemical patterns. Not only will one have places where the contact line would have interactions with all four phases present in the system, but the merging point between two chemical species must not reflect the groove boundary effect. Despite of all technical difficulties present in realising such a system, the motivation for exploring the phase space of such a system also is to

improve the fundamental understanding of the complex behaviour of the solid film contact line, such as slip effects or macroscopic effects of wetting different chemical species locally along the contact line. The same type of boundary conditions can be realised through the physical patterning of the substrate, such as grooves or pillars, but geometrical problems starts to arise such as break-ups of compact solid films or the creation of the new contact line, along with the dependance of boundary conditions on way too many geometrical parameters.

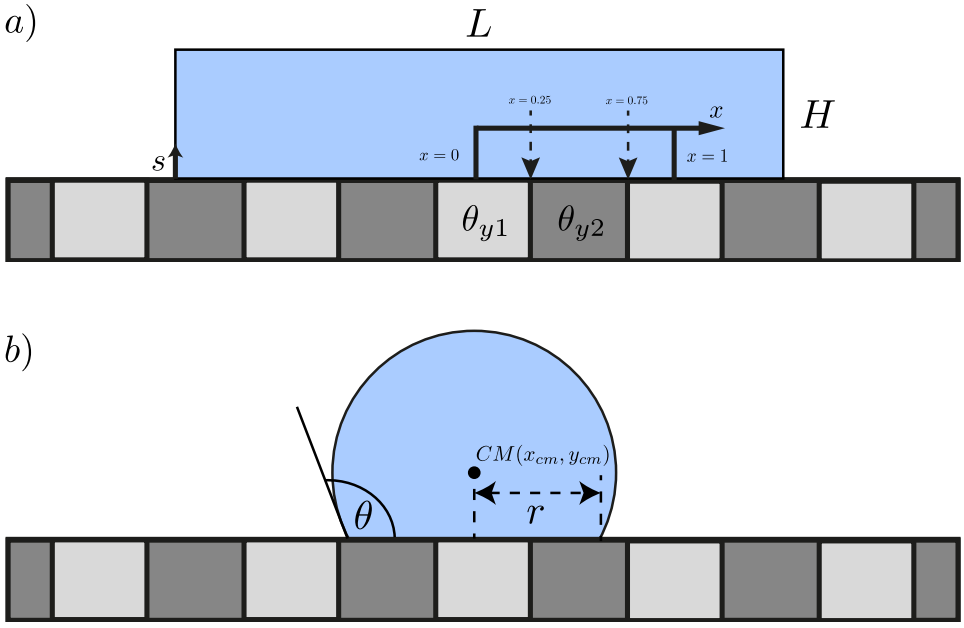

Figure 7.1: In a) we define geometrical properties of the substrate and the initial solid film morphology. θ_{y1} and θ_{y2} respectively denote the Young's angle of periodic stripes. The solid film is initially a rectangle of height H and length L. With s we define arc length parameter which has a zero value on the left solid side. In b) we characterise equilibrium shapes of solid-state dewetting with the contact radius r and the contact angle θ. The point $CM(x_{cm}, y_{cm})$ is positioned in the solid centre of mass.

In Figure 7.1.a we show the schematics of the system with all spatial coordinates made dimensionless by the spatial period of the chemical pattern ℓ_{ch}. Substrate is patterned with periodic stripes of two different material, where each individual stripe has a width of $\ell_{ch}/2$. Throughout the calculation, we set the Young's angles to $\theta_{y1} = 120°$ and $\theta_{y2} = 100°$, respectively. To properly define Young's angle, we write

$$\theta_y = \begin{cases} \theta_{y1}, & \text{if } x^\star < 0.25 \quad \text{or} \quad x^\star > 0.75 \\ \theta_{y2}, & \text{if } x^\star > 0.25 \text{ and } x^\star < 0.75 \end{cases} \tag{7.1}$$

where with the $x^\star = \mid x \mid - \lfloor \mid x \mid / \ell_{ch} \rfloor$ we denote the remainder of a division between the absolute value of the spatial dimensionless coordinate x and the

period of the chemical pattern ℓ_{ch}. The solid film interface is described with functions $x(s,t)$ and $y(s,t)$, where s is the arc length parameter and t is the dimensionless time. We assume that the solid film does not change along the third dimension, which makes current problem two-dimensional. The contact line on the left side of solid film has value $s=0$, while on the contact line on the right side has value $s=s_{end}$, where s_{end} is the interface length (Figure 7.1.a). In the case when the contact line crosses the symmetry point $x=0$, such as $x(0,t)>0$ and $x(s_{end},t)<0$. To account for this problem in the analysis ahead, we define for either left or right contact line

$$x^\star = \mid 1 - x^\star \mid \text{ if } x(0,t)>0 \text{ or } x(s_{end},t)<0 \tag{7.2}$$

7.2 Theoretical and numerical details

There are three important aspects of the given problem which will be analysed separately: solid-state dewetting, set of the specific boundary conditions we need for describing transitions of contact line from one chemical species to the other and the Young-Laplace equation. Solid-state dewetting is governed by surface diffusion of atoms along the interfacial layer of the solid, in the direction of the negative chemical potential gradient [15, 16]. For isotropic solids, such as in the model systems which were mentioned in the *Introduction*, the chemical potential linearly depends on the curvature and the governing equation reads [16]

$$\tilde{u} = B\tilde{\nabla}_s^2\tilde{K} \tag{7.3}$$

where $\tilde{u}$ is the interface velocity in the interface normal vector direction, $\tilde{K}$ the curvature, $\tilde{\nabla}_s^2$ the surface Laplacian operator along the solid interface and $B=\gamma D\nu\Omega^2/k_BT$ is the material constant which affects the time scale of the whole system, while it does not alter the morphological landscape through which the solid will go throughout the dewetting process. Material properties which determine the value of the material constant B are the surface tension of the solid with the outer phase γ, the surface diffusivity D, cross-section density of migrating atoms ν, the molecular volume Ω and the thermal energy of the system k_BT. To make the Eq. 7.3 dimensionless, all of the spatial coordinates are normalised by the period of the chemical pattern ℓ_{ch}, while the time is made dimensionless by normalising it with ℓ_{ch}^4/B. The resulting dimensionless equation is

$$u = \nabla_s^2 K \tag{7.4}$$

where u is the dimensionless interface velocity in the interface normal vector direction, K is the dimensionless curvature, while ∇_s^2 represents the dimensionless surface Laplacian operator. Firstly, we will introduce only boundary conditions which are already common for the solid-state dewetting. To ensure the mass conversation of the solid, we have to set the curvature gradient on the contact line to zero,

$$\left.\frac{\partial K}{\partial s}\right|_{s=0} = \left.\frac{\partial K}{\partial s}\right|_{s=s_{end}} = 0 \tag{7.5}$$

The contact angle boundary condition sets the contact angle to the value of the local Young's angle θ_y (Eq. 7.1), for the case of the contact line position not being positioned on the transitions from one chemical species to another

$$\left.\frac{\partial y(s,t)}{\partial x(s,t)}\right|_{(s=0)} = -\left.\frac{\partial y(s,t)}{\partial x(s,t)}\right|_{(s=end)} = \tan\theta_y \tag{7.6}$$

where the opposite sign for contact line on the right and left side of the solid film accounts for the opposite relative position between the contact line and the solid contact area with the substrate. For the case of the contact line positioned on the transition between chemical species there are four possible scenarios: receding contact line motion from the smaller to larger equilibrium contact angle, receding contact line motion in the opposite direction and the advancing contact line motion for both cases.[17, 18] Values of the Young's angles in the current work define the region with the equilibrium contact angle θ_{y1} as an region with the higher equilibrium contact angle. Although there are four possible scenarios of the contact line motion from one chemical species to another, one of two contact line events will occur: slip or pinning. Pinning occurs when the contact line recedes from the θ_{y1} region to the θ_{y2} region, or when the contact line advances in the other direction. Pinning fixes the position of the contact line in the transition point, until the local morphology of the solid rotates enough for satisfying boundary condition expressed in Eq. 7.1. This boundary condition is completely analogues to the case of the solid state dewetting over the physical singularity and the liquid wetting of chemically patterned substrate. In the case of the receding contact line motion from the θ_{y2} region to the θ_{y1} or the advancing contact motion in the other direction, in the moment when the contact line touches the transition point, we abruptly change the value of the contact angle, since the equilibrium contact angle cannot be formed in that transition point. Here lies the big difference between the behaviour of liquid drops and solids on chemically patterned substrates. In the case of liquid drops, the nonzero slip length causes larger changes in the morphology, since throughout the bulk there is an hydrodynamical flow, but

in the case of solids, the slip is truly local and only affects the position of the contact line. In many reports of either growing or shrinking droplet[19, 20], stick-slip contact line motion is observed, while the experimental evidence of the exact behaviour of the contact line slip for solids is nonexistent at the moment. Let us denote the current contact angle absolute value on the left side of solid θ_ℓ and with θ_r on the right side. To mathematically summarise all boundary conditions expressed in this paragraph, we will first express pinning boundary conditions, where for the left contact line the boundary condition reads

$$x(0,t) = x(0,t-\Delta t), \text{ if } x^\star = 0.75 \text{ and } \theta_2 < \theta_\ell < \theta_1 \tag{7.7}$$

and for the right side the boundary condition is identical

$$x(s_{end},t) = x(s_{end},t-\Delta t), \text{ if } x^\star = 0.75 \text{ and } \theta_2 < \theta_r < \theta_1 \tag{7.8}$$

where $t-\Delta t$ represents previous time step in the calculation. The slip boundary condition is more easily expressed in the terms of θ_ℓ and θ_r. For the left and the right contact line ($\theta_{\ell,r}$) we define

$$\theta_{\ell,r} = \begin{cases} \theta_{y1}, & \text{if } x^\star = 0.25 \text{ and } \theta_{\ell,r} = \theta_{y2} \\ \theta_{y2}, & \text{if } x^\star = 0.25 \text{ and } \theta_{\ell,r} = \theta_{y1} \end{cases} \tag{7.9}$$

With the set of boundary conditions expressed in Eqs. 7.5-7.9, we have mathematically closed the problem for the case of a chemical substrate with the local wettability expressed in Eq. 7.1. We would like to remind the reader that inside the definition of $x^\star$, which is expressed in Eq. 7.2, we take into account the case when contact line crosses the point of symmetry $x = 0$.

So far we were discussing dynamical properties of the system, but looking at possible equilibrium shapes of the solid-state dewetting process reveals additional nuances present in the system. As visible from Eq. 7.4, all of the dynamics diminish once the curvature becomes constant along the solid interface. Additionally, due to contact angle boundary conditions (Eqs. 7.5-7.9), the local equilibrium contact angle is always the current contact angle, therefore, the final equilibrium shape is identical to the solutions of Young-Laplace equation, which implies constant curvature shape along with the equilibrium contact angle. To obtain all of those shapes, we must minimise the interfacial energy which in dimensionless space is

$$E = s_{end} - \int_{x(0,t)}^{x(s_{end},t)} \cos\theta_y dx \tag{7.10}$$

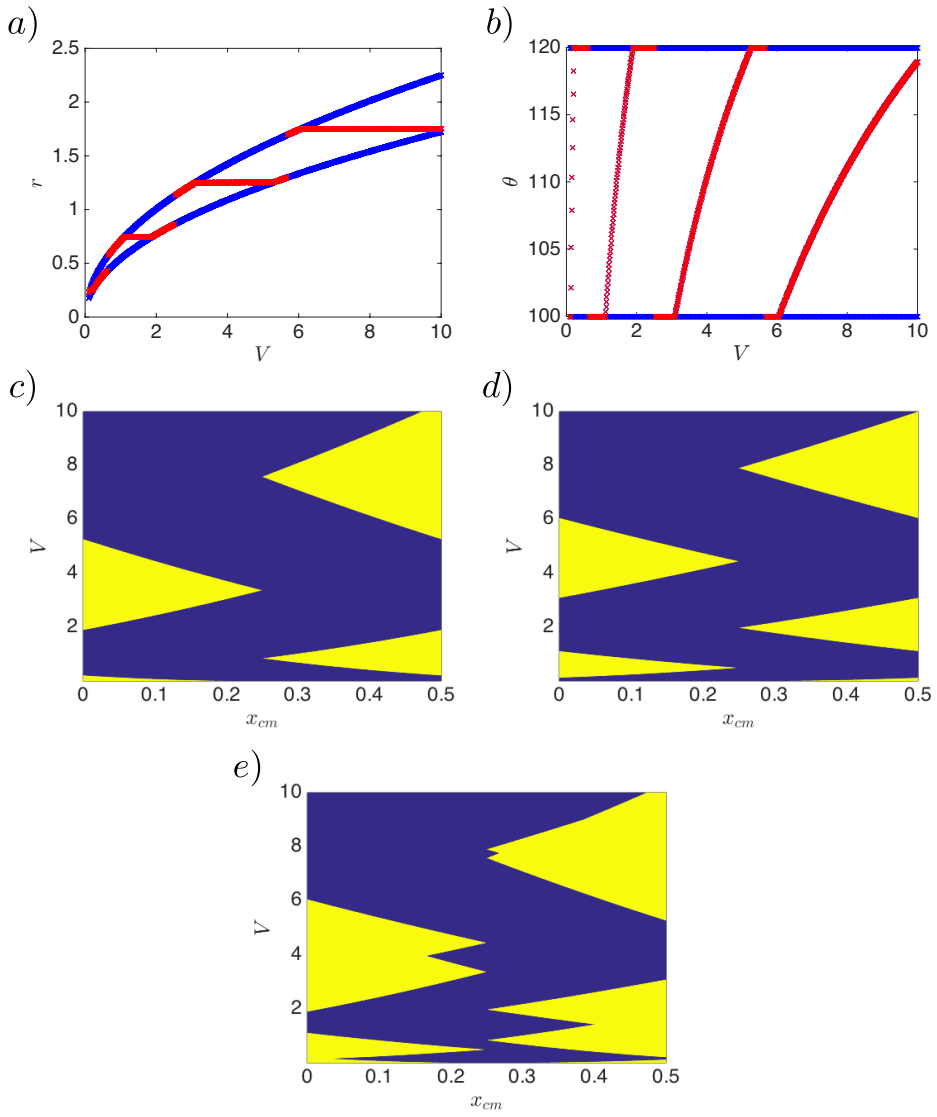

Figure 7.2: Collection of all solutions of Young-Laplace equation expressed in $V-r$ space in a and in $V-\theta_y$ in b subplot. With the blue colour we indicate local minima, while the global one is denoted with the red colour. In the next three subplots we showcase where these stable solutions can occur as a function of x_{cm}, where the yellow colour represents available phase space. In c we show this phase space for the case of spherical caps with the θ_{y1} Young's angle, while in d the same thing is shown for the spherical caps with the θ_{y2} Young's angle. In e we show the total restriction effect of the present substrate on the droplet position.

We will explore all of the solutions by controlling the position of the centre of mass x_{cm}. The main reasoning behind using the centre of mass as a control variable is validated due to the properties of the interfacial energy, namely, the energy remains constant if we shift the whole morphology towards any orientation in x direction, as long as the contact line stays inside same stripes on the both sides of the solid. To exclude additional unnecessary calculations, we will minimise Eq. 7.10 for two cases: $x_{cm}=0$ and $x_{cm}=0.5$. These val-

ues where chosen so that the centre of the mass is positioned right above the centroids of individual stripes and with this method we are able to detect all the possible local stable shapes. The minimisation was performed in a fashion that we construct a family of spherical caps under the volume constraint and let the contact angle be a free variable. We report all minima present in the calculation for both values of x_{cm} in Figure 7.2, where we summarise all properties of the family of equilibrium shapes. Additionally, in Figure 7.1.b, we define all geometrical parameters with which we characterise this family of equilibrium shapes. For a dimensionless solid volume V, either the dimensionless contact radius r or the equilibrium contact angle θ are sufficient to describe the shape, due to the constant curvature implication of the Young-Laplace equation. As visible from Figure 7.2.a and 7.2.b, for a single value of the dimensionless volume V, there is always more than one possible equilibrium shape, where for the very small volume ranges we only have two possible states, while the number of minima increases with the increasing volume value. We limit our phase space to $2 \leq V \leq 10$, so that we can focus on the part of phase space where only three minima are available. Horizontal lines in Figure 7.2.a represent the equilibrium shape with the contact line being positioned at the transition points which allow pinning scenario and the contact angle value between two Young's angles which characterise the system. This shape is the global minimum for the solid, if it is available in the given phase space. In Figures 7.2.c-e the additional interplay between the Young-Laplace equation and the chemical substrate is revealed. For an equilibrium shape from Figures 7.2.a-b there is an restriction on the position of centre of mass for which contact angle boundary conditions can be satisfied. The phase diagram for values of x_{cm} larger than 0.5 is not shown, since there is a plane symmetry around $x_{cm} = 0.5$ inside the single spatial period of the chemical substrate ℓ_{ch}, which in dimensionless space is the unit length. For a case of the equilibrium shape with the contact line positioned on transition points which allow pinning scenario, centre of mass always has a value of either $x_{cm} = 0$ or $x_{cm} = 0.5$. For example, the solid of a volume $V = 10$ and the fixed position of the centre of mass at $x_{cm} = 0$, cannot form an spherical cap with the contact angle either θ_{y1} or θ_{y2}, therefore unless the dynamics push away solid from that region, we can only observe a formation of the global minimum.

To solve the governing equation Eq. 7.4, coupled with boundary conditions expressed in Eqs. 7.5-7.9, we use the *marker* numerical scheme[21], in which we discretise the solid interface via markers and solve the governing equation locally in every marker. The governing equation is a forth order partial differential equation, so the largest value of integrating time step is defined as $dt = ds^4/C$, where for our code converging results occur only for a value of C

up to ten. To optimise the numerical integration, we make markers equidistant every 5000 time steps using the *spline* interpolation of functions $x(s,t)$ and $y(s,t)$, since from given interpolations, curvature as a function is smooth.

7.3 Results

To explore the phase space of equilibrium shapes we fix the initial solid height $H = 1$ and we introduce an initial centre of mass parameter $x_i = x_{cm}|_{t=0}$. Dependance of the equilibrium shape on the initial state was not investigated for heterogeneous substrates, but for anisotropic solids it is known that depending on the initial state[22, 23], they will finish up in one of many solutions of the so-called Winterbottom construction [24]. As already stated, we keep the solid volume value between $2 \leq V \leq 10$, which directly translates to $2 \leq L \leq 10$, while values of x_i range inside the single spatial half-period, since the soild-state dewetting has same symmetries as energy phase diagrams shown in Figure 7.2.c-e.

In Figure 7.3.a-b we show the contact line dynamics ($V = 3$) for both left and right contact line in the inital stage of solid-state dewetting. The pinning scenario is visible via regimes of dynamics where the position of contact line is constant for values $x^\star = 0.75$ ($x = -0.75$ and $x = 1.75$), while the slip motion of contact line is visible as a singularity point at $x^\star = 0.25$ ($x = -1.25$ and $x = 1.25$). After the slip occurs, the contact line accelerates its receding motion since the curvature is locally created, but after a while, it relaxes to the normal dewetting motion. Solutions of the Young-Laplace equation indicate that the solid has to migrate to the zone in which the equilibrium shape can be formed. In Figure 7.3.c we follow these dynamics and it is observable that for cases of $x_i = 0$ and $x_i = 0.5$ the centre of mass does not move throughout the dynamics. The contact line behaviour is symmetrical with respect to plane $x = x_i$ and the time it takes for these shapes to converge is of an order of magnitude smaller than for other values of x_i. Since contact line dynamics are symmetrical, the same must hold for values of θ_ℓ and θ_r because of the contact angle boundary conditions which are symmetrical. If we start the solid-state dewetting for any value of x_i which is not positioned above centroids of stripes in the substrate, the symmetry is broken and different values of θ_ℓ and θ_r can be observed. If we define this difference as $\Delta\theta \equiv \theta_\ell - \theta_r$, we can see on Figure 7.3.d that the sign and the value of this variables is directly affecting the migration of centre of mass, where for the case of $\Delta\theta = 0$, the centre of mass for solid is fixed in space. Huge difference in convergence times also indicate that symmetrical shapes converge to the equilibrium by migration of atoms from contact line to the centre, while for the other cases convergence is slow due to migration of atoms

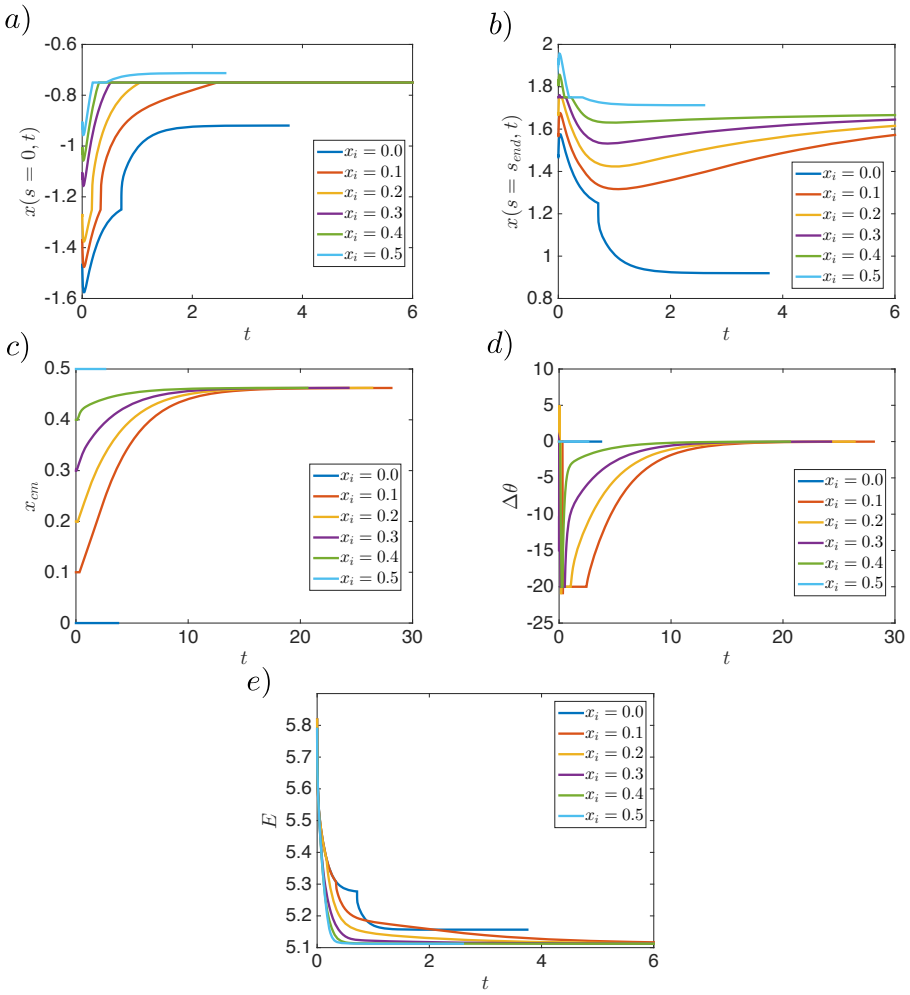

Figure 7.3: Contact line dynamics are shown in a) for the left contact line and in b) for the right contact line, where pinning and slip motion is qualitatively very clear. Migration of the centre of mass (c)) is directly connected to the sign of the difference in contact angles (d)) observed on both sides of the solid, allowing the solid to migrate to zones in energy phase diagram where the formation of equilibrium shape is feasible. In e), we show the evolution of the interfacial energy (Eq. 7.10), where the presence of other minima in the system is visible due to the existence of singularity points in the same evolution (only observable for $x_i = 0$ and $x_i = 0.1$).

from one side of the solid film to the other, which shows that chemical patterns affect the solid-state dewetting in a same fashion as physical singularities do. The evolution of the interfacial energy (Figure. 7.3.e) reveals that the solid searches for available equilibrium shape locally (contact-line driven). Out of six cases in Figure 7.3, five of them finish up as a spherical cap with the contact angle θ_{y2}, which in this case is the global minimum, while only for the case of $x_i = 0$ we observe formation of the spherical cap with the contact angle θ_{y1}. However, for cases $x_i \leq 0.2$, there is a singularity point in the interfacial energy evolution, which occurs in the same time as the slip occurs for the left contact line. Since the slip for the case of $x_i = 0.0$ happens later in time, it also implies

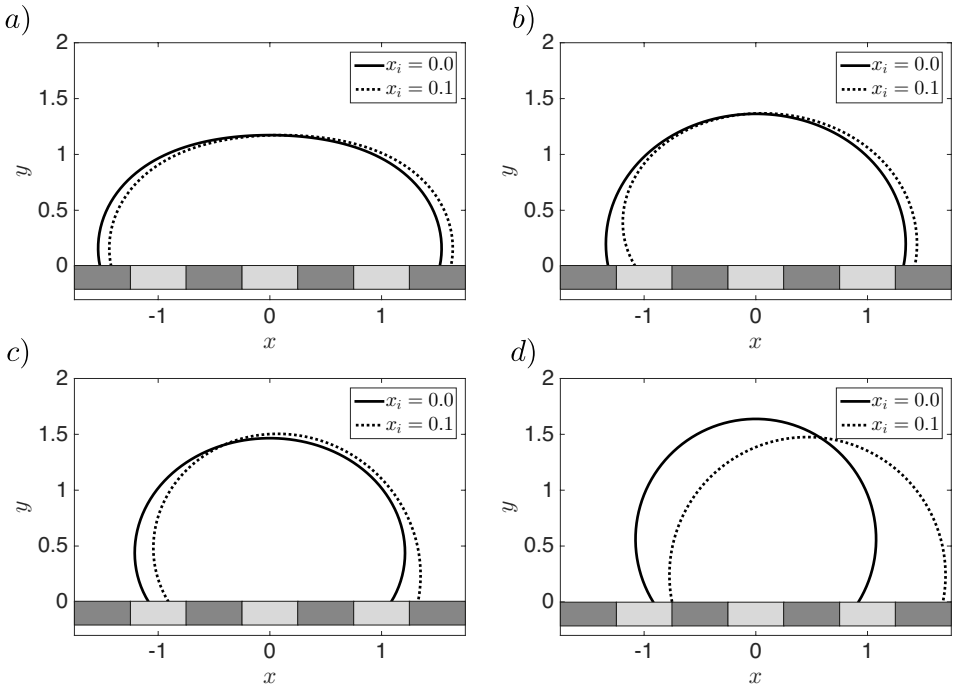

Figure 7.4: Morphology evolution for solid films with different values of x_i is shown. In a) both solids have an identical interface since in both cases the contact line remained on the same stripe during the dynamics ($T = 0.1$). Solids become morphologically different in b) since the contact line for solid with $x_i = 0.1$ slipped across the transition point ($T = 0.4$). In c) both solids start converging towards attainable equilibrium shape ($T = 0.8$), which is shown in d)

that the slip happens once the solid morphology is closer to the equilibrium shape and the solid-state dewetting quickly goes in the local minimum, due to the two-way convergence, but if slip happens in earlier stages of dynamics, contact line approaches the pinning point extremely fast, which by itself is comparable to the stick-slip motion of evaporating droplets. While in the case $x_i = 0$ slip enables the solid to approach to the global energy minimum, we can observe a complete opposite scenario on the behaviour of the right contact line. The one case in which the right contact line experiences slip ($x_i = 0$), the solid morphology converges to the stable local minimum, while other cases experienced migration of solid towards positive x direction, due to the sign of $\Delta\theta$ in that stage of dynamics, which also resulted in the advancing motion of the right contact line. Although in all non-symmetrical cases the left contact line is positioned at the pinning point, the value of $\Delta\theta$ at the end of the dynamics, along with interfacial energy value, reveal that this shape is energetically identical to the symmetrical shape found in the case of $x_i = 0.5$. In Figure 7.4 we show series of shapes for $x_i = 0$ and $x_i = 0.1$. Since the qualitative behaviour indicates that the final equilibrium shape only depends on the contact line dynamics, we would like to quantify this dependence by

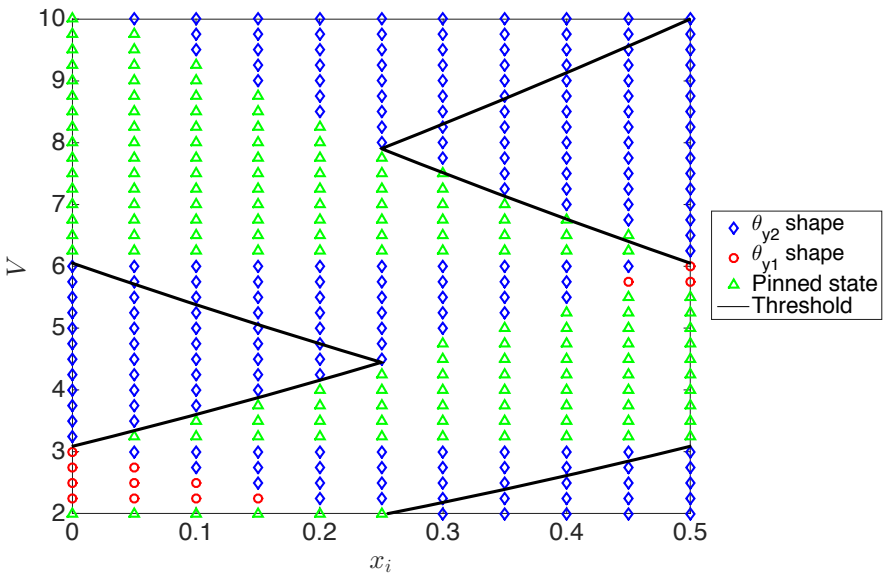

Figure 7.5: Phase diagram of equilibrium shapes obtained by solid-state dewetting. Individual markers represent the type of equilibrium shape, while the solid lines indicate threshold areas from the energy phase diagram shown in Figure 7.2.d.

comparing energy phase diagrams (Figure 7.2.c-e) with the phase diagram of equilibrium shapes obtained by the solid-state dewetting, with different initial positions of centre of mass and different lengths, where the solid length and the solid volume are identical, since we keep the solid height fixed.

In Figure 7.5 we show the phase diagram, which is very similar to energy phase diagrams from Figure 7.2, with the only difference that x_{cm} is replaced from the x-axis and instead of it we write the centre of mass in the initial moment of dynamics x_i. From the quantitive difference between the two phase diagrams we can immediately see the influence of the contact line on the migration of the whole solid. There are two striking properties revealed by observing equilibrium shapes: for a fixed volume, the solid will only be able to access two minima for each value of the solid volume V, even if by the energy phase diagrams there are three minima available; and the equilibrium shape with the contact angle θ_{y2} is present for some values of x_i for every volume V. With the solid lines in Figure 7.5 we indicate threshold values from the energy phase diagram (Figure 7.2.d) for equilibrium shapes with the contact angle θ_{y2}. When the value of x_i corresponds to values of x_{cm} for which this equilibrium shape can be obtained, the solid does not migrate. When x_i is out of the range of available values of x_{cm} the solid will either migrate to the part of the substrate where the equilibrium shape with the contact angle θ_{y2} or it will form different equilibrium shape. The tendency is that solid goes to the global minimum (pinned state), unless the pinned state is not obtainable (small ranges of volume around values $V = 3$ and $V = 6$). This qualitative

behaviour additionally indicates the importance of the contact line dynamics in the solid-state dewetting. For a fixed volume V, the spherical cap with the smaller contact angle θ will have larger contact radius r, but this implies that on the substrate which we use in the current work, that for the solid to reach the pinned equilibrium shape, the solid contact line has to have sufficient speed over areas with the equilibrium contact angle θ_{y2} so the morphology does not converge there. In the same fashion, for the solid to reach the equilibrium shape with the contact angle θ_{y1} has to unpin from transitional points which allow pinning scenarios. This behaviour explains the large disparity present in area fractions of individual equilibrium shapes.

7.4 Conclusion

Solid state-dewetting on the chemical patterns has been numerically investigated to clarify the effect of surface patterns on the contact line dynamics and the macroscopical effect on the solid equilibrium morphology, which is affected due to existence of multiple solutions of Young-Laplace equation. Taking inspiration from liquid capillary interactions, we introduce the stick-slip motion of the contact line, but the effects of such a motion have more local effect in the case of solids than in the case of liquids. As a result, the occurrence of equilibrium shapes in the phase diagram are not affected by the energy value of the same equilibrium (whether it is the global or the local minimum), but by the geometrical availability either via restrictions of solutions of the Young-Laplace equation or via converging to the first available energy minimum. In the current framework it becomes clear that the migration of the solid bulk only occurs when different values of the contact angle are observed on the opposite solid sides, while in the case of the same contact angles, the centre of mass remains stationary independent of the current solid morphology.

References

[1] C. V. Thompson. Solid-state dewetting of thin films. *Annu. Rev. Mater. Res.*, 42:399–434, 2012.

[2] F. Leroy, Ł . Borowik, F. Cheynis, Y. Almadori, S. Curiotto, M. Trautmann, J. C. Barbé, and P. Müller. How to control solid state dewetting: A short review. *Surf. Sci. Rep.*, 71:391–409, 2016.

[3] P. G. de Gennes, F. Brochard-Wyart, and D. Quere. *Capillarity and wetting phenomena: drops and bubbles and pearls and waves.* Springer, New York, 2004.

[4] P. G. de Gennes. Wetting: statics and dynamics. *Rev. Mod. Phys.*, 57:827, 1985.

[5] David Quere. Wetting and roughness. *Annu. Rev. Mater. Res.*, 38:71–99, 2008.

[6] W. T. E. van den Beld, A. van den Berg, and J. C. T. Eijkel. Spatial control of direct chemical vapor deposition of graphene on silicon dioxide by directional copper dewetting. *RSC Adv.*, 6:89380–89386, 2016.

[7] A. L. Giermann and C. V. Thompson. Solid-state dewetting for ordered arrays of crystallographically oriented metal particles. *Appl. Phys. Lett.*, 86, 2005.

[8] J. Ye and C. V. Thompson. Templated solid?state dewetting to controllably produce complex patterns. *Adv. Mater.*, 23:1567–1571, 2011.

[9] Y. Ishikawa, Y. Imai, H. Ikeda, and M. Tabe. Pattern-induced alignment of silicon islands on buried oxide layer of silicon-on-insulator structure. *Appl. Phys. Lett.*, 83:3162–3164, 2003.

[10] I. Dević, W. T. E. van den Beld, A. van den Berg, J. C. T. Eijkel, and D. Lohse. Solid-state dewetting on grooved substrate. *To be submitted.*

[11] E. Dornel, J. C. Barbé, F. de Crécy, and G. Lacolle. Surface diffusion dewetting of thin solid films: Numerical method and application to si/sio$_2$. *Phys. Rev. B*, 73, 2006.

[12] J. Ye and C. V. Thompson. Regular pattern formation through the retraction and pinch-off of edges during solid-state dewetting of patterned single crystal films. *Phys. Rev. B*, 82:193408, 2010.

[13] G. H. Kim, R. V. Zucker, J. Ye, W. C. Carter, and C. V. Thompson. Quantitative analysis of anisotropic edge retraction by solid-state dewetting of thin single crystal films. *J. Appl. Phys.*, 113:043512, 2013.

[14] E. Rabkin, D. Amram, and E. Alster. Solid state dewetting and stress relaxation in a thin single crystalline ni film on sapphire. *Acta Mater.*, 74:30–38, 2014.

[15] C. A. Johnson. Generalization of the gibbs-thomson equation. *Surf. Sci.*, 3:429–444, 1965.

[16] W. W. Mullins. Theory of thermal grooving. *J. Appl. Phys.*, 28:333–339, 1957.

[17] A. Dupuis and J. M. Yeomans. Lattice boltzmann modelling of droplets on chemically heterogeneous surfaces. *Future Gener. Comput. Syst.*, 20:993–1001, 2004.

[18] M. Iwamatsu. Contact angle hysteresis of cylindrical drops on chemically heterogeneous striped surfaces. *J. Colloid Interface Sci.*, 297:772–777, 2006.

[19] E. Dietrich, E. S. Kooij, X. Zhang, H. J. W. Zandvliet, and D. Lohse.

Stick-jump mode in surface droplet dissolution. *Langmuir*, 31:4696–4703, 2015.

[20] D. Orejon, K. Sefiane, and M. E. R. Shanahan. Stick-slip of evaporating droplets: Substrate hydrophobicity and nanoparticle concentration. *Langmuir*, 27:12834–12843, 2011.

[21] H. Wong, P. W. Voorhees, M. J. Miksis, and S. H. Davis. Periodic mass shedding of a retracting solid film step. *Acta Mater.*, 48:1719–1728, 2000.

[22] W. Bao, W. Jiang, D. J. Srolovitz, and Y. Wang. Stable equilibria of anisotropic particles on substrates: a generalized winterbottom construction. *SIAM J. Appl. Math.*, 77:2093–2118, 2017.

[23] W. Bao, W. Jiang, Y. Wang, and Q. Zhao. A parametric finite element method for solid-state dewetting problems with anisotropic surface energies. *J. Comput. Phys.*, 330:380–400, 2017.

[24] W. Winterbottom. Equilibrium shape of a small particle in contact with foreign substrate. *Acta Mater.*, 15:303–310, 1967.

8 Conclusions and outlook

8.1 Main results

In this thesis, we have investigated wetting interactions with many types of patterned substrates and with various interactions such as a body force and the disjoining pressure. Although the two core results of the wetting theory (Young's law and Young-Laplace equation) are always observed, many "side-effects" are noticed as a patern complexity increases.

In *Chapter 2* we have analysed interplay between wetting effects, the disjoining pressure and the gas compressibility. The given theoretical framework has a diverging interaction at the substrate, therefore the current problem cannot truly resolve the contact line properties. The distortion caused by disjoining pressure is only observable very close to the contact line, where the bubble obtains a shoulder-like shape, while the shape far away from the contact line is a spherical cap. Main result is the existence of a threshold aspect ratio for which boundary conditions are satisfied. The threshold aspect ratio approaches the aspect ratio dictated by the Young's law and the Young-Laplace equation (without the disjoining pressure), as we increase the bubble height.

Chapters 3 and 4 deal with wetting problems on patterned substrates. In *Chapter 3* we analysed the system of a flat substrate decorated with micro-caps. The given geometry is convinient, since the droplet will have a truncated spherical cap shape due to a symmetry of the sphere-sphere intersection. Analysis of equilibrium shapes reveals that the droplet position, whether it is on

the microcap, the flat substrate or at the microcap rim, is only dictated by values of surface tensions present in the system and are completely independent of the droplet size. Although we obtain numerically a linear expression for a threshold wetting scenario, this expression seems to be non-obtainable analytically. In *Chapter 4* we show that the curvature plays as important role as does the equilibrium contact angle. Depending on the aspect ratio of the lyophilic elliptical patch, the droplet in a quasi-steady grow will either completely wet the patch or it will start spreading on the lyophobic part of the substrate, although there is a finite amount of the lyophilic patch available to the droplet. Additionally, in this work we also show that the Metropolis stochastic algorithm is capable of minimising the interfacial energy as precise as the energy gradient method (Surface Evolver). In *Chapter 5* we introduce an external body force to the droplet. Although many experimental and numerical studies were performed on sliding drops, hereby we present a full thermodynamical calculation of equilibrium shapes. Qualitative difference between the present work and the literature is that we have included the contact energy in our calculation, while so far a more common approach was to model the contact angle hysteresis, instead of calculating the contact energy. We identify two types of threshold shapes, where in one case the droplet cannot satisfy Young-Laplace equation smoothly, while in the other case the droplet would have tendency to go inside the substrate, due to the curvature becoming negative at some parts of a droplet interface.

In *Chapter 6* we have developed the *marker* numerical code for simulating the process of the solid-state dewetting. We investigated the effect of substrate physical singularities on the solid dynamics. The contact line behaviour at the geometrical singularity shines light on a lot of novel qualitative properties of solid-state dewetting, namely, the contact line will not unpin itself from the singularity if the complete morphology is close to the equilibrium shape and the convergence to the equilibrium shape has two modes, where the time needed to reach the equilibrium shape can be an order of magnitude smaller in a faster mode. Natural enquiry which arose is how does this effect affect the solid-state dewetting once there are many possible solutions to the Young-Laplace equation. This question was tackled in *Chapter 7*, where we introduce the chemical patterning to the solid-state dewetting research. While this induces many complex contact line behaviours, the main result of this chapter is that the solid-state dewetting is completely a contact line driven problem. While this result might not come as a surprise to some of you, solid-state dewetting on a striped pattern shows that it does not prefer to go to the global energy minimum, but rather it converges to the first available equilibrium shape, independent of the energy value of that same equilibrium.

8.2 Outlook

While there are still many unanswered questions in wetting, the future direction of the field should be of a multi-disciplinary approach. When it comes to droplets and bubbles, the logical evolution of the field is to dwell in to the interaction of many droplets or bubbles via diffusion. Since the time scale of a diffusion is very long, a common approximation is to treat the droplet/bubble evolution as a quasi-steady one, which implies that every temporary morphology is the solution of the Young-Laplace equation. Another big unanswered question which remains is the contact angle hysteresis. While the theoretical framework used in this thesis immediately removes the hysteresis from calculations, there are some problems where the implementation of hysteresis is the only way of solving problems, however, these results eventually have to converge with the "pure" thermodynamics used in this thesis. Implementing the knowledge from fluids on the solid-state dewetting provided us with novel results, which accidentally open up a lot more questions. While there is still a fundamental problem with simulating anisotropic solids (crystals), the goal should be to understand the interplay between crystallography and contact line effects on patterned substrates, since most of solids are anisotropic. Considering that the anisotropic solid has multiple equilibrium states even on a flat homogenous substrate, the complexity of this system increases with patterns on the substrate.

Summary

Wetting and dewetting effects of all phases are crucial for many scientific and industrial applications such as catalysis, microfluidics and nanopatterning. Although some of effects are known for a half of century, many details about stable equilibrium shapes are still unknown to this day. The main goal of this thesis is to explore stable equilibrium shapes of bubbles, droplets and solids. We are interested in equilibrium shapes of aforementioned bodies once they cover patterned substrates (physically or chemically) and once they are under the influence of interactions such as the disjoining pressure or a body force. To predict the equilibrium shape in the wetting system, one needs to minimise the interfacial energy of a given body (bubble, drop or solid) under the volume constraint. Additional interactions can be incorporated by adding the potential energy of said interaction to the energy minimisation.

Additional complication arises with bubbles due to the gas compressibility, which also has to be taken into account in the total energy, once a bubble is exposed to an additional interaction. In Chapter 2 we investigated the interplay between a single bubble and the disjoining pressure. Due to the gas compressibility, nanobubbles and nanodrops with the same amount of molecules will significantly differ in size. Additionally, a nanodrop will form a nearly spherical cap shape under the influence of the disjoining pressure, while a nanobubble will significantly deform close to the contact line. We reveal that the disjoining pressure implies the existence of maximum nanobubble aspect ratio. As the bubble height increases, this maximum aspect ratio asymptotically approaches the classical bubble shape (solution of Young's law and Young-Laplace equation for wetting a homogeneous substrate).

Droplets are incompressible, therefore the equilibrium droplet shape will be identical to the classical bubble equilibrium shape of the same volume (only surface tension dependent). In Chapters 3 and 4 we minimised the droplet interfacial energy for a substrate decorated with microcaps and for a single lyophilic elliptical patch respectively. Microcaps are solid spherical caps which can have a different Young's angle from the flat substrate. We showed that the difference in Young's angles (one for the microcap and one for the flat substrate) and the microcap contact angle with the flat substrate

determine the droplet nucleation location. In Chapter 4 we investigated the droplet morphology on the single lyophilic elliptical patch. Since the patch edge has a nonconstant curvature, there are two scenarios of a quasi-steady droplet growth. Depending on the Young's angles present in the system and the patch aspect ratio, the droplet will either cover the whole patch at one moment during the growth or the droplet will start to wet the lyophobic part of the substrate even when there is an available lyophilic area to wet. In industrial applications, this qualitative difference between the two mentioned scenarios will determine whether the application is efficient or not.

We applied the body force to the sessile droplet in Chapter 5. The force direction is chosen in a fashion that it pushes the droplet to a chemical step which separates the substrate in two semi-infinite areas: a lyophilic and a lyophobic half. Since we are pushing droplet from the lyophilic to the lyophobic area, there are going to be droplet equilibrium shapes at the chemical step. If we would increase the value of body force, which is controlled via the Bond number Bo, we would encounter the maximum threshold Bond number for which there are geometrically available energy minima. The value of threshold Bond number increases with the increasing difference in Young's angle values, but once this difference becomes too large, the curvature also starts affecting the value of threshold Bond number.

When solids are heated to the sub-melting temperature, they will start to deform via a surface diffusion of atoms along the solid interfacial layer. This process is called solid-state dewetting and we investigated it on patterned substrates. Solid and liquid dewetting have qualitatively different dynamic mechanisms, but the final equilibrium shape is identical. In Chapter 6 we have investigated the effect of geometrical singularities present in a grooved substrate on the solid-state dewetting. The contact line pinning which occurs at the aforementioned singularity affects the solid macroscopically and it is observable in a value of time required to reach the equilibrium. Due to the macroscopic effect of the contact line on the solid, in Chapter 7 we introduce the solid-state dewetting on a chemically patterned substrate, namely a striped substrate. There are multiple available equilibria for a solid for the given volume on the striped substrate and we revealed that the solid will go to the global energy minimum if the contact line dynamics allow it. To track this effect, we were changing only position of the initial solid centre of a mass and we provided the phase diagram for given dynamics. We revealed that the solid will go to the global energy minimum only if the contact line dynamics move the solid to the part of the substrate where that particular equilibrium shape can be formed.

Samenvatting

Bevochtiging- en ontvochtigingseffecten van alle fases zijn cruciaal voor veel wetenschappelijke en industriële toepassingen zoals katalyse, microfluidica en nanopatroonvorming. Hoewel sommige effecten al een halve eeuw bekend zijn, zijn veel details over stabiele evenwichtsvormen tot op heden onbekend. Het hoofddoel van dit proefschrift is om stabiele evenwichtsvormen van bellen, druppels en vaste stoffen te verkennen. We zijn geïnteresseerd in genoemde evenwichtsvormen wanneer deze substraten met patronen (fysische of chemische) bedekken en wanneer ze onder invloed van interacties zo als ontkoppelingsdruk of een lichaamskracht zijn. Om de evenwichtsvorm in een bevochtigingssysteem te voorspellen, moet men de grensvlakenergie van een gegeven lichaam (bubbel, druppel of vaste stof) minimaliseren onder een voorwaarde van behoud van volume. Aanvullende interacties kunnen worden meegenomen door de potentiele energie ervan op te nemen in de energieminimalisatie.

Aanvullende complicaties ontstaan met bubbels door de compressibiliteit van het gas, dat ook meegenomen dient te worden in de totale energie, wanneer de toegevoegde interactie aanwezig is. In hoofdstuk 2 onderzoeken we wisselwerking tussen een enkele bubbel en de ontkoppelingsdruk. Door de compressibiliteit van het gas verschillen nanodruppels en nanobubbels met dezelfde hoeveelheid moleculen significant van grootte. Daarbij zullen nanodruppels bijna een bolvormige dop vormen onder de invloed van de ontkoppelingsdruk waar nanobubbels significant vervormen dicht bij de contactlijn. We onthullen dat de ontkoppelingsdruk het bestaan van een maximum nanobubbel aspectratio impliceert waarvoor deze nog steeds stabiel is. Wanneer de hoogte van de bubbel toeneemt, benaderd de maximum aspectratio asymptotisch de klassieke bubbelvorm (oplossing van Youngs wet en Young-Laplace vergelijking van het bevochtigen van een homogeen substraat).

Druppels zijn niet-samendrukbaar, daarom zal een druppelvorm in evenwicht identiek zijn aan de klassieke bubbel evenwichtsvorm bij hetzelfde volume (alleen oppervlaktespanning afhankelijk). In hoofdstuk 3 en 4 minimaliseren we de druppel oppervlakte energie voor een substraat gedecoreerd met microkappen en een lyofiel ellipsvormige vlak, respectievelijk. Microkappen zijn vaste bolkappen die een andere Youngs hoek kan hebben dan het vlakke

oppervlak. We hebben laten zien dat het verschil in Youngs hoeken (en voor de microkap en een voor het vlakke oppervlak) en de contacthoek van de microkap met het substraat bepalend is voor de locatie van druppel nucleatie. In hoofdstuk 4 onderzochten we druppel morfologie op een enkel lyofiel ellipsvormig vlak. Omdat het vlak een niet constante kromming heeft zijn er twee scenario?s voor quasi-statische druppelgroei. Afhankelijk van Youngs hoeken in het systeem en de aspectratio van het vlak, zal de druppel het hele vlak bedekken gedurende het groeien, of beginnen met het lyofobische gedeelte van het substraat te bevochtigen terwijl er nog een lyofiel gebied beschikbaar is. In industriële toepassingen bepaalt het kwalitatieve verschil tussen de twee genoemde scenario?s of de applicatie efficiënt is of niet.

We passen een lichaamskracht toe op de sessiele druppel in hoofdstuk 5. De richting van de kracht is gekozen op een manier die de druppel naar een chemische stap duwt die het substraat scheidt in twee halfoneindige oppervlakken: een lyofiele en lyofobe helft. Omdat we de druppel van het lyofiele naar de lyofobe oppervlak duwen, zullen er evenwichtsvormen van de druppel bestaan bij de chemische stap. Als we de lichaamskracht vergroten, die bestuurd wordt via het Bondgetal Bo, zouden we een maximum drempelwaarde voor het Bondgetal tegenkomen waarvoor er geometrisch beschikbare energieminima beschikbaar zijn. De drempelwaarde van dit getal neemt toe met een toenemend verschil in Youngs hoeken, maar wanneer dit verschil te groot wordt zal de kromming ook de drempelwaarde beïnvloeden.

Wanner vaste stoffen verhit worden tot een sub-smeltende temperatuur, zullen ze deformeren via oppervlaktediffusie van atomen bij het grensvlak. Dit proces wordt vastestof-ontvochtiging en we onderzochten dit op substraten met patronen. Vastestof- en vloeistof-ontvochtiging hebben kwalitatieve verschillen dynamische mechanieken, maar de uiteindelijke evenwichtsvormen zijn identiek. In hoofdstuk 6 hebben we het effect van geometrische singulariteiten aanwezig in vastestof-ontvochtiging op een gegroefd substraat onderzocht. Het pinnen van de contactlijn dat voorkomt bij voorgenoemde singulariteit beïnvloed de vaste stof macroscopisch. Het is meetbaar in de tijd die nodig is om het evenwicht te bereiken. Door de macroscopische effecten van de contactlijn van de vaste stof introduceren we in hoofdstuk 7 de vastestof-ontvochtiging op een substraat met een chemisch patroon, namelijk een gestreept substraat. Er zijn meerdere beschikbare evenwichten voor een vaste stof voor een gegeven volume op een gestreept substraat en we onthulden dat de vaste stof alleen naar het globale minimum gaat als de contactlijndynamica dat toe staat. Om dit effect te volgen veranderden we de positie van het centrum van massa van de initiële vaste stof en voorzagen we in een fasediagram voor de gegeven dynamica. We onthulden dat de vaste stof alleen naar het globale minimum gaat

als de contactlijndynamica de vaste stof verplaatst naar het gedeelte van het substraat waar die specifieke evenwichtsvorm gevormd kan worden.

Acknowledgements

After finishing my master studies in 2014, I literally had no idea what to do with my life. There were some job offers available, but they just didn't seem to fit the "big picture". Problem with the "big picture" was that I wanted to be an astrophysicist, until my last year of studies, when the change of mood kicked in. In my quest for finding an answer, I wrote down scientific fields I would be interested. Afterwards, I investigated what is the set of problems which characterises the field and in the end, there was only one result: fluid physics. Me being me, I just naively googled "phd positions in Europe in fluid physics" and one of the first links was link to the *Physics of Fluids* group in the Netherlands. Again, me being me, I just sent an enquiry e-mail to the chair of the group explaining that I have no background in the field and that I am just curious in general.

The above description is neither a perfect resume or a perfect motivation background for a future academic, but it resulted in a Skype conversation with Detlef Lohse, who would turn out to be my PhD supervisor. Dear Detlef, the only thing I can say is thank you for the leap of faith you took when you offered me position in your group. I would like to think that this thesis is proof I validated your trust, but I still cannot believe I got a shot. After the job interview, two of us talked a bit and you said a sentence which still perfectly describes our relation: *"Ivan, there are two types of people in science: a model and a problem scientist. While I declare my self as the problem scientist, you seem to be on the opposite side. This is going to be interesting."* Ironically, we never found common ground in this philosophical discussion, so I would just conclude that both of us are set in our ways, but we managed to produce solid science despite our disagreements. Words cannot describe the amount of knowledge and experience I obtained here. What words also fail to describe is how much my life has changed during these four years. Thank you for tolerating my article skills in English. Thank you for being supportive of my "last-second" way of working as long as results keep flowing. Thank you for showing me what it takes to be a successful scientist. However, me being me, to truly depict dynamic between two of us, I have to provide you with few comments which would make you even a better supervisor for future students:

- People are very angry after their national football team gets kicked out of European/World championships. It is not a very smart idea as a supervisor to provoke your students literally seconds after it happens. I waited full day before I sent you e-mail about South Korea.
- Brown is a wonderful colour

Once again, thank you for everything.

When I started my PhD, someone had to take care of my initial baby steps. Luckily for me and sadly for him, this task was assigned to Vitaly. Dear Vitaly, Chapter 2 of this thesis literally wouldn't exist without you, while all of other chapters have your signature all over them. I fondly remember our daily discussions in your office, since this was a "flash-course" for me to catch up, due to my knowledge gap. STEM education in Croatia is hugely influenced by Russian school of mathematics and physics, so discussing things with you just felt like being home: hardcore analytics, no pretty analogies of flying butterflies and most importantly the Slav motivation school. To this day, you are still the only person in academia who knew how to motivate me. Before an average reader thinks there were nice words involved in motivating me, I would invite you to reread the phrase Slav motivation school ("I bet you can't do it"). While I am extremely thankful for your scientific help, I am even more thankful for help in less scientific areas. First time I attended FoM days, during the lunch break you invited me to join you and you just told me: "this is how you should behave on conferences". What you taught me that day is how to approach any person in the scientific environment, how to spark their interest and how to at the same time be skeptical about them. This is a type of education most students don't experience during their lifetimes and I truly consider it an unfair advantage I had you as a mentor that day. But for you, that was just a start and soon I started receiving personal advices about both my life and future planning of my career, for which I am grateful. However, the suggestion I will always remember (besides how to drink vodka) is the one about girls. I would like to use this opportunity to spread this wisdom: *"Every guy is too stupid at 25 years old to know what they want in girls."* I am so sorry I didn't listen back then, you were right.

Next step is to reflect on the location which brings me some of the happiest memories from my life in the Netherlands, my office. The Magic quartet was formed in early 2015 and up to the current day, chemistry level keeps on getting higher. I am actually happy I am the first one leaving, since office without any of you, is just another four-wall room. Dear Huanshu, my only officemate with mutual scientific work. If only Detlef knew how many sleepless nights two

of us had because of NBA, he would fire us both. Every day of NBA season, my working day would start with two of us fanboying over the highlights from the previous night. Both of us are huge Kobe Bryant fans and I am so happy your PhD defence was exactly on 24/8, two Kobe numbers (and my sister's birthday). Those two magical numbers also describe two of us: I like to think I am 8, while you are 24. You know what I mean by this. We also played basketball a lot together and for me, this is a sacred bond, my friend. Dear Mathijs, two of us brought the geek culture to our office, probably in an over the top fashion, but still it was so satisfying just to throw references around the office and have someone recognise them. Thank you for translating my Summary chapter and thank you for building my PC setup. Aside from being geeks, two of us were also the musical half. Singing Britney Spears and Frozen soundtrack will never be the same after you. I am so sorry we still didn't play a game of *Starcraft*, but at least you got to crush me in chess. But you know how they say: "It don't mean a thing, if it ain't got that swing". Dear Anupam, I feel so lucky two of us started and finished our Dutch adventure around the same time. Since you were my theoretical brother in arms, we shared so many struggles throughout my PhD, so much that I considered you the living proof I am not crazy, but that my problems are pretty normal ones. We were moving each other across Enschede, we were commenting each others work, we were investigating ethanol flows together...simply put two bodies one soul (sorry Kanishka). You have some of the most wonderful Facebook profile picture I ever saw and sometimes just looking at them can make my day. I always considered you one of the most talented guys around and I always enjoyed our discussions about science. But to be fair, I enjoyed our non-scientific discussions even more. I will forever remember when two of us lost three days of our lives developing a dynamical theory, which was inspired by a Youtube video of some stupid guy brutally injuring himself with a very long whip. This is what science is all about.

If you step outside of the office for the second, you will notice a lot of "PoF-ers" swarming around. If you look careful, you will notice a lot of intereseting characters. Dear Yaxing, you are the best thing ever made in China. Two of us are true *Dota* fans, so much that we spent four years of our life arguing are Chinese or European teams better. Absolutely priceless. Our weekend in Frankfurt was epic, during which you taught me the only Mandarin word I know how to pronounce (niceuuuhhhh, I hope you spell it like this). I sincerely hope you will live long enough to see a good Chinese football or basketball team. Thank you for the Christmas card in 2014, I will never forget that one. Dear Vamsi, I still hate you for being a second faster on the karting circuit

in Enschede. At least, I still hold better lap time than you in Oldenzaal, so it is an even result. We need to choose a third track to finally settle this. I suggest Nurburgring in tuned cars, do you accept? Also, next time we see each other there will be no thesis pressure on our heads, so we might see a Champions league game together again after so long. Dear Biljana, literally thank you for existing, because without you, I would forget how to speak Croatian. Our information exchanges about availability of ajvar in Enschede are both hilarious and sad. And please, quit smoking, it is bad for your health. You should know better by now. Dear Crossfit Dennis, may the force be with you. You are now approaching the same deadline I am currently facing. Remember, fear leads to the dark side. You need to teach yourself how to let go. Let it go, Dennis, let it go. Dear Other Dennis, thank you for organising board game nights and I sincerely hope in near future experimentalists are going to listen to you. Dear Elise, if you ever need a ride in the morning, I am your guy. As long as you complain the whole drive, I will take you anywhere you want to go. Dear Maxime, boys have swag, guys have style, but real men have class. I remember. Dear Sander, I really like your photos, but somehow I always finish up ugly on them. Somehow. Dear Erwin, thank you for showing me chill dudes can be successful. Dear Michiel, drop it like its hot. Dear Álvaro, my limping brother, two of us have so much memories, yet I cannot tell a single one here. Makes you wonder why, right? Dear Sr. Escobar, you're simply the best. You're better than all the rest. Dear Myrthe, at first I was afraid, I was petrified, kept thinking I could never teach without you by my side. Dear Ricardo, you are the only colleague TA I don't have a song with, so we should definitely work on that. We still have to go for chess and pool. Dear Diana, trust me when I say that you will enjoy last two years of your PhD. Dear Anaïs, I am so sorry we didn't get to collaborate earlier and thank you for the experience of following World cup together. We knew from day one we will meet in finals. Dear Carola, it is very rude to pursue career in physics, yet you own a hairstyle which breaks all of thermodynamics laws. Dear Jessica, you are next in the line. You will find out in few days what this actually means. Dear Class-Willem, thank you for being a "big bro" so many times. Dear Stefan, while your scientific input may seem minimal, it was still crucial for this thesis. Dear Minori, I just sincerely miss you. As you can see, there are so many people I had to remember and sadly I probably forgot few names here. To compensate for that, if you didn't find yourself in the text so far, you are getting a title of "Unsung hero", which I hope will make you happy sufficiently. Now there are few names which were skipped intentionally so far, because some of them are more than "PoF-ers".

Dear PoF united, my forth favourite football team (the list goes Hajduk

Split, Croatia, Barcelona, PoF United), I still remember when I started playing for you. It was the worst football I ever experienced in my lifetime. I still remember being sad for days just because of this. But like a phoenix, we rose from ashes. It was not until "The Flying Dutchman" Ruben took over the ship and said I have an idea. I am faster than all of you, so lets play counter attacks focused on me. I can only score about 10% of shots, so produce a lot of them. Before you start laughing, it was not until this moment when we finally started to score some wins. As wins started to amass, we attracted a lot of football talent. "The Sultan of Swing" Ali is still causing vertigo feelings to defences all across the University, although he is not here for more than a year. "The Caveman" Pieter just looks frightening, but nothing compared to the "Oligarch from the East" Mikhail. Unlike them, Jelle is injured way too often for a cool nickname. If we need to become really serious during the game, we just throw a "Hurricane" Nakul at the opposing team, while Alex "Kahn" is guarding our back. All in all, very fun times which made my life here so wonderful. If we were not playing football, basketball was the sport of choice. And when it comes to basketball, there is only one Peter who looks like a direct copy/paste of Tim Duncan. This is the biggest compliment anyone has received so far in this chapter and you know it.

There is a famous trio of guys which simply deserve a separate paragraph just for three of them. Los hermanos. Dear Rodrigo, our academic lives are synced up, our love lives are synced up (sadly for both of us) and of course, our epic guitar skills are sooooo synced up. By the way, do you remember that epic Detlef Christmas e-mail? Yep, we've been through it all. Also, nouuuou. Dear Enrique, you love Slavs and I love Latin people. Two of us getting along was never in question. As in, we barely even tried and it worked. Europe misses you man, come back here. Thank you for all of meals you prepared. I still consider you "The Chef". Dear Rodolfo, you deserved a separate paragraph, but your ego is already overblown. Thank you for trusting in me in the start of my PhD. Whenever I needed an opinion, you were there, whenever I was confused with academia, you were there, whenever I didn't even need you, you were there (we could work on this one). Something tells me our paths will collide once more and I sincerely hope that it will happen.

Dear Joanita, you are everything to everyone. Simple as that. Dear Bas, Gert-Wim and Martin, I didn't bother you as much as other students did, but I always loved when I had excuse to come chat with you. There are only finite amount of people in PoF who understand what motorcycles, cars and rock n' roll really mean.

Dear MCEC members, we should definitely collaborate.

It is time to move for a while back to Croatia, because there are so many people who are part of this thesis. My family had to listen for hours about my problems here and rarely did they complain about it. For that I thank you all. Special mention will always go to my generation of Dević family (siblings and in-laws) because they made me the person I am today. However, I must admit I started liking "next-gen" Dević family much more, since they are helping me to become a person I want to be in future and they are less boring compared to us. Mala, you might not have official Dević name in your documents, but for pure act of tolerating my dear father, I hope you know you are included by definition in this paragraph.

My dear friends from Split, you are one of the biggest reasons I want to come back. Dear *Panchos*, you are more than friends. You are the way of life.

The academic title I will obtain here would be a distant dream if I didn't had guidance all the way throughout my life. Of course, this is the part where I reflect on professors who effectively changed who I am. Dear Andrea Norac, you are the zero-patient of this story. You were my first physics teacher ever and that small detail lead my life to this point. Dear Antonio Vrbatović, while you are not so good in mathematics though, the skepticism you installed in my head came very useful in my later years. It is your own fault that I became so skeptical that even you cannot tolerate it anymore. Dear Ante Bilušić, you were not only an academic father figure to me, but to all of us who had pleasure to had you as our professor. All the fundamental physics knowledge I posses is your influence. Simply put, thank you. Dear Leandra Vranješ Markić, you were the first one to give me academic job (teaching assistant) and the first one to push me out of my comfort zone. Thank you for trusting in me. Dear Petar Stipanović, thank you for showing me how to be efficient with my numerical codes. Last but not least, dear Dejan Vinković, thank you for supervising me before Detlef took over. You gave the "final touch" which made me ready for the next step. And I would just like to remind you, if you could graduate in Zagreb, so could I. I hope you remember the incident I am referring with my last sentence.

Dear opponents, I am ready.
Dear all, until next time,
Ivan